Université catholique de Louvain

Earth and Life Institute

Fractional diffusion models for epidemiological and immunological applications

Doctoral dissertation presented by

Afshin Farhadi

in partial fulfilment of the requirements for the degree of

Doctor of Philosophy in Bioscience Engineering

Thesis committee:

Prof. Emmanuel Hanert (Supervisor)	UCLouvain, Belgium
Prof. Patrick Bogaert	UCLouvain, Belgium
Prof. Pierre-Antoine Absil	UCLouvain, Belgium
Prof. Gholamhossien Erjaee	University of California, Irvine, USA
Dr. Dana Copot	Ghent University, Belgium
Prof. Jacques Mahillon (President)	UCLouvain, Belgium

Louvain-la-Neuve, July 2022

Abstract

Lévy flights are a specific model of random walks that appear to be ubiquitous across a wide range of fields where the diffusion process is faster than predicted by classical Brownian motion. Lévy flights consist of a succession of random displacements whose step lengths have a heavy-tailed probability distribution. Unlike Brownian motion, whose step-length probability distribution decays exponentially, the distribution of Lévy flights decays algebraically. This leads to heavier tails and hence a larger probability of very long displacements that would be almost impossible with a Brownian motion. This thesis consists in deriving a space-fractional-order diffusion model that explicitly represents the effect of Lévy flights, deriving a numerical algorithm for solving the model equations, and then applying it to study the dispersion of living organisms in the field of life-science problems. In immunology, it has been observed that $CD8^+$ T cells adopt a Lévy flight foraging pattern in response to Toxoplasma gondii infection in the brain. Here, we show that the Lévy search pattern enables T cells to spread over the whole brain tissue and hence they can rapidly destroy infected cells distributed throughout the brain tissue. However, with the Brownian motion assumption, T cells travel through the brain slowly, leading to a slower decline of the infected cells far away from the source of T cells. In nature, the existence of landscape and physiological limitations prevents the occurrence of arbitrary large displacements by the individuals following a Lévy flight. Instead, truncated Lévy flights are introduced, which lead to truncated space-fractional-

order diffusion models with a truncation parameter. As an application of such equations, we propose a simple epidemic model with the assumption that infected individuals follow a truncated Lévy flight, and then we investigate the effect of different values of the truncation parameter on the epidemic speed. Finally, we explore the obtained results for a more realistic model, i.e., the West Nile virus epidemic, which happens among wild birds and mosquitoes. We suggest that truncated space-fractional-order diffusion models can provide appropriate estimations of the epidemic speed that is underestimated and overestimated by the models based on pure Brownian and Lévy movements, respectively. Our proposed model leads to accelerating epidemic waves that finally reach a constant speed representing the maximum speed of the epidemic.

Acknowledgement

First of all, I would like to express my sincere gratitude to my supervisor Professor Emmanuel Hanert for the continuous support of my Ph.D. study and related research, for his patience, motivation, and immense knowledge. His guidance helped me in all the time of research and writing of this thesis. I would also like to thank my committee members, Professor Gholamhossien Erjaee, Professor Patrick Bogaert, Professor Pierre-Antoine Absil, and Dr. Dana Copot for their insightful comments and encouragement, and finally I am particularly appreciative to Professor Jacques Mahillon for having agreed to be the president of my committee.

Contents

List of acronyms

CTRW	Continuous-Time Random Walk
CLT	Central Limit Theorem
PDF	Probability Density Function
LF	Lévy Flight
ML	Mittag-Leffler
MSD	Mean-Squared Displacement
TLF	Truncated (Tempered) Lévy Flights
FDM	Fractional Diffusion Model
DC	Dendritic Cell
RW	Random Walk
BBB	Blood-Brain Barrier
PV	Parasitophorous Vacuole
FE	Finite Element
WNV	West Nile Virus
BM	Brownian Motion
PLF	Pure Lévy Flight
APC	Antigen Presenting Cell

CHAPTER 1

Introduction

One can ask what would be a differential having as its exponent a fraction. Although this seems removed from geometry... it appears that one day these paradoxes will yield useful consequences.
Gottfried Leibniz (1695)[1]

Movement among living organisms is a ubiquitous process that happens for numerous reasons. In their search for food, shelter, and mate, animals need to move. Birds make different types of movements, including local movements within their home range or territory for daily activities, and migration away from the breeding sites to live a season in a new area. Humans travel between home and work. The immune system cells must move throughout the body in order to find the sites of infected cells, and pathogens like viruses also search for healthy cells in the tissues of the body to infect them.

[1] This is a part of Leibniz's reply to a question that L'Hôpital asked in a letter: What is the meaning of the expression $d^n y/dx^n$ if $n = 1/2$? This was the beginning of what we now call fractional calculus. (source: Kalmykov et al. (2006))

A general crucial question relevant to the movements is what strategy the organisms adopt in their search for targets. This has prompted biologists and ecologists to statistically specify the characteristics of the movement trajectories. As a way of categorizing the movements, their displacements can be either regular and directed or random and highly irregular. For instance, during an infection in the body, there are molecules called chemokines that direct the movement of activated T cells from lymph nodes towards the infected tissues. However, T cells then move randomly within infected tissues to find pathogens. When compared to directional movement, random movements allow biological organisms to execute more efficient searches for the targets whose sites are unknown a priori. The distribution of targets is a crucial factor that limits the cognitive and detective skills of organisms and hence they randomly move to optimize their search. The random (stochastic) motion is the main focus of this thesis.

In a variety of disciplines, including ecology, biology, chemistry, physics, and technology, the term "diffusion" is applied to the random motions of living and non-living objects, such as molecules, atoms, cells, bacteria, and animals in an environment. In physics, the motion of molecules from a region of high concentration to places of low concentration is referred to as diffusion. In ecology, diffusion can be designated to the spread or dispersal of animals. As examples of diffusion processes, see Figure 1.1. All of the scientists in these fields have similar interests to study the diffusion processes in space and time. To this end, the diffusion equations, as the best-known models ranging from simple to complex have been obtained. Indeed, diffusion models are partial differential equations whose solutions represent the space and time evolution of the density (concentration) of particles following random movements in an environment.

Given the ubiquity of diffusion processes in a variety of engineering and natural science applications, the most important question arises as follows:

How can diffusion equations be derived by considering different types of diffusion processes?

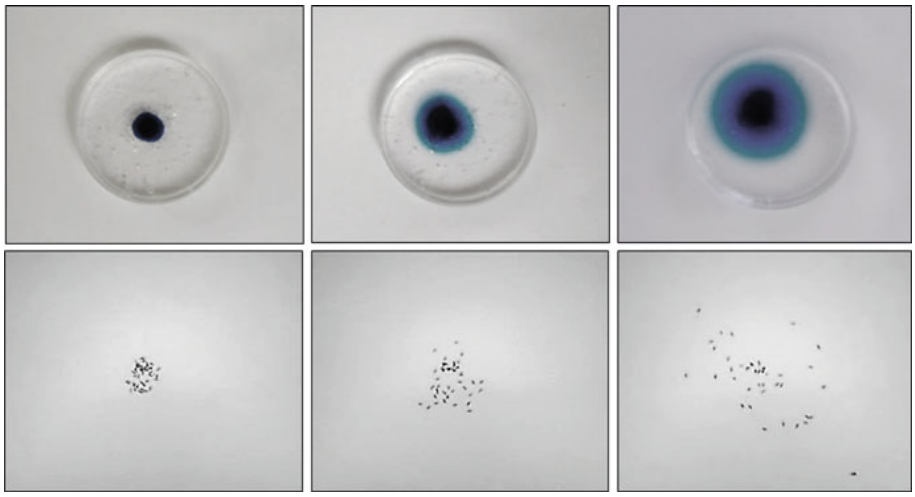

Fig. 1.1: Upper panels: diffusion of an ink drop in liquid media (glycerine). Lower panels: diffusion of ants (Aphaenogaster senilis) from a center where they have been grouped previously. (source: Méndez et al. (2016))

The answer to this question is relevant to topics, such as random walk theory, and stochastic processes. More precisely, the most well-known method of *Continuous-Time Random Walk* (CTRW) has built bridges between diffusion processes and space-time diffusion equations. Before moving to the discussion of a CTRW process, let us first present some essential concepts of probability theory that are used throughout this chapter.

1.1 Some topics from probability theory

In this section, we provide a summary of some basic elements in mathematical probability. More details can be found in the book

by Freund et al. (2004).

Probability theory is defined as the mathematical study of an empirical phenomenon whose outcome is not certain before it happens. In that case, we can consider a set of all possible outcomes called the *sample space*, which is usually denoted by Ω. A sample space according to the number of points or elements that it contains can be classified - that is finite or infinite. Here, we only consider sample spaces that are infinite, i.e., Ω is a continuous interval of outcomes. Any subset A of Ω is called an event. The probability of an event satisfies the property $0 \leq P(A) \leq 1$, where P denotes a probability measure.

A mapping X from the sample space Ω to a subset of $\mathbb{R}$ is called a **random variable** if $P(\{\omega : a \leq X(\omega) \leq b\})$ can be calculated based on the given probability P for every $a, b \in \mathbb{R}$. Indeed, A random variable X is defined as a real-valued function defined over the elements of Ω. Note that $X(\omega)$ is called a realization of X. A random variable X is said to be continuous if the set of realizations of X is an interval I of the real line and there exists a non-negative function $f(x)$ such that

$$P(\{\omega : a \leq X(\omega) \leq b\}) = P\{a \leq X \leq b\} = \int_a^b f(x)dx,$$

for any $[a, b] \subset I$. The function $f(x)$ defined on I is called the **probability density function (pdf)** of X. It should be noted that a function f can serve as a pdf of a continuous random variable X if it satisfies the conditions: $f(x) \geq 0$ for every $x \in \mathbb{R}$, and $\int_{-\infty}^{\infty} f(x) = 1$.

Given a pdf $f(x)$ of a continuous random variable X, the nth **moment** about the origin of X, which is denoted by $E[X^n]$, is defined by

$$E[X^n] = \int_{-\infty}^{\infty} x^n f(x)dx,$$

for $n = 1, 2, \ldots$. Some of the moments have special names. The first-order moment $E[X]$ is called the **mean** value of X, and it is denoted simply by μ. the nth moment about the mean of X, which is denoted by $E[(X-\mu)^n]$, is defined by

$$E[(X-\mu)^n] = \int_{-\infty}^{\infty} (x-\mu)^n f(x)dx,$$

The second moment about the mean is called the **variance**, which is usually denoted by σ^2. It can be easily shown that $\sigma^2 = E[X^2] - \{E[X]\}^2$.

A **joint probability density function** of the continuous random variables X and Y is defined as a bivariate function with values $f(x, y)$ over the xy-plane such that for any region A in the xy-plane:

$$P\{(X, Y) \in A\} = \iint_A f(x, y)dxdy.$$

In that case, $f(x, y)$ satisfies the conditions: $f(x, y) \geq 0$ for every $x, y \in \mathbb{R}$, and $\int_{-\infty}^{\infty} \int_{-\infty}^{\infty} f(x, y)dxdy = 1$. If X and Y are continuous random variables and $f(x, y)$ is the value of their joint probability density at (x, y), the function given by

$$g(x) = \int_{-\infty}^{\infty} f(x, y)dy,$$

is called the **marginal density** of X. Correspondingly, the function given by

$$h(y) = \int_{-\infty}^{\infty} f(x, y)dx,$$

is called the **marginal density** of Y. If the values of the joint pdf $f(x, y)$ are given by the products of the corresponding values of the two marginal densities $g(x)$ and $h(y)$, i.e., $f(x, y) = g(x)h(y)$, then the two random variables X and Y are said to be **independent**.

In probability theory, **stochastic (or random) processes** deal with the evolution of a collection of random variables. More precisely, we can define a stochastic process as a family of random variables $\{X(t,\omega) : t \in T, \omega \in \Omega\}$, where T is a set of the time parameter. If T is a continuous interval of real numbers, then the process is called a continuous-time stochastic process. It should be noted that for each fixed ω, the stochastic process can be considered as a function that depends on t, and for each fixed t, we have a random variable $X(\omega)$.

1.2 Continuous-Time Random Walk

A Continuous-Time Random Walk (CTRW) is a stochastic process, which originally described by Montroll and Weiss (1965). To illustrate this process in one dimension, we assume that a walker moves randomly to the left and right sides. First, the walker starts at the the origin at time $t_0 = 0$. The walker makes a jump of size $x_i \in \mathbb{R}$ at time t_i. After waiting until time t_{i+1}, he or she makes another jump of size x_{i+1} at time t_{i+1}. The time between these two subsequent steps is given by $\tau_i = t_{i+1} - t_i$, for $i = 1, 2, ...$, which is defined as the pausing times (or waiting times). Here, it is assumed that the jump sizes x_i and the waiting times τ_i are independent and identically distributed random variables. By defining $N(t)$ as the number of jumps up to time t, which is given by $N(t) = \max\{n : t_n \leq t\}$, the position of the walker at time t can be obtained as follows:

$$x(t) = \sum_{i=1}^{N(t)} x_i.$$

Let T and X be the waiting time and jump size random variables, respectively. If $f_{\mathrm{XT}}(x,t)$ is the joint pdf of the random variables T and X, then the marginal densities of X and T, respectively satisfy

$$f_{\mathrm{X}}(x) = \int_0^\infty f_{\mathrm{XT}}(x,t)dt, \quad \text{and} \quad f_{\mathrm{T}}(t) = \int_{-\infty}^\infty f_{\mathrm{XT}}(x,t)dx.$$

Now, given $f_{\mathrm{X}}(x)$ and $f_{\mathrm{T}}(t)$, the mean value of the waiting time μ_{T} and the second moment of the jump size σ_{X}^2 about its mean with zero value ($\mu_{\mathrm{X}} = 0$) can be obtained as follows:

$$\mu_{\mathrm{T}} = \int_0^\infty t f_{\mathrm{T}}(t) dt, \quad \text{and} \quad \sigma_{\mathrm{X}}^2 = \int_{-\infty}^\infty x^2 f_{\mathrm{X}}(x) dx. \tag{1.1}$$

We can classify different CTRW processes based on the finite or diverging values of μ_{T} and σ_{X}^2 defined by Eq. 1.1.
Let $P(x,t)$ represent the probability that the walker reaches the position x at time t. Of great significance is the relationship between $P(x,t)$ and $f_{\mathrm{XT}}(x,t)$, which can be described by the following equation called the Montroll-Weiss equation (or Master equation):

$$P(x,t) = \delta(x)R(t) + \int_0^t \int_{-\infty}^\infty P(u,v) f_{\mathrm{XT}}(x-u, t-v) du dv, \tag{1.2}$$

where $\delta(x)$ is the Dirac delta function and $R(t) = P\{T > t\} = 1 - \int_0^t f_{\mathrm{T}}(v) dv$. In the case of an uncoupled (independent) CTRW, i.e., $f_{\mathrm{XT}}(x,t) = f_{\mathrm{X}}(x) f_{\mathrm{T}}(t)$, the Master equation 1.2 can be expressed in the following Fourier-Laplace form:

$$\widetilde{\widehat{P}}(k,s) = \frac{1 - \widetilde{f_{\mathrm{T}}}(s)}{s} \frac{\widehat{P}(k,0)}{1 - \widetilde{\widehat{f_{\mathrm{XT}}}}(k,s)} = \frac{1 - \widetilde{f_{\mathrm{T}}}(s)}{s} \frac{\widehat{P}(k,0)}{1 - \widehat{f_{\mathrm{X}}}(k)\widetilde{f_{\mathrm{T}}}(s)}, \tag{1.3}$$

where $\widehat{P}(k,0)$ is the Fourier transform of the initial condition $P(x,0)$, $\widetilde{f_{\mathrm{T}}}(s)$, and $\widehat{f_{\mathrm{X}}}(k)$ are the Laplace and Fourier transforms of the pdf's f_{T} and f_{X}, respectively defined as follows:

$$\mathcal{L}\{f_{\mathrm{T}}(t)\} = \widetilde{f_{\mathrm{T}}}(s) = \int_0^{+\infty} f_{\mathrm{T}}(t) e^{-st} dt,$$

and

$$\mathcal{F}\{f_{\mathrm{X}}(x)\} = \widehat{f_{\mathrm{X}}}(k) = \int_{-\infty}^{+\infty} f_{\mathrm{X}}(x) e^{ikx} dx.$$

For more details on the derivation of the Master equation, refer to (Ibe, 2013; Méndez et al., 2016). In order to simulate CTRW

processes, we need to define pdf's for the jumps length and waiting times. To do this, in the next two sections, we shall introduce a family of pdf's for the jump length, known as Lévy distributions, and Mittag-Leffler functions for the pdf of the waiting times.

1.3 Lévy distribution

We define X as a Lévy stable random variable if its pdf S with parameters $0 < \alpha \leq 2$, $-1 \leq \beta \leq 1$, $\gamma > 0$, and $\delta \in \mathbb{R}$ can be expressed with the following inverse Fourier transform:
If $\alpha \neq 1$

$$S(\alpha, \beta, \gamma, \delta; x) = \mathcal{F}^{-1}\left\{\exp\left(i\delta k - \gamma^{\alpha}|k|^{\alpha}(1 - i\beta\,\mathrm{sgn}(k)\tan\frac{\alpha\pi}{2})\right)\right\}, \tag{1.4}$$

and if $\alpha = 1$

$$S(\alpha, \beta, \gamma, \delta; x) = \mathcal{F}^{-1}\left\{\exp\left(i\delta k - \gamma|k|(1 + i\beta\,\mathrm{sgn}(k)\frac{2}{\pi}\ln|k|)\right)\right\}, \tag{1.5}$$

where

$$\mathrm{sgn}(x) := \begin{cases} -1 & \text{if } x < 0 \\ 0 & \text{if } x = 0 \\ 1 & \text{if } x > 0 \end{cases}$$

and $\mathcal{F}^{-1}$ denotes the inverse Fourier transform defined as follows:

$$\mathcal{F}^{-1}(\widehat{f}(k)) = f(x) = \frac{1}{2\pi}\int_{-\infty}^{+\infty}\widehat{f}(k)e^{-ikx}dk.$$

The parameters α, β, γ, and δ characterize the Lévy distributions, which have the following definitions:

1. The parameter α is called the *tail exponent* or the *stability index*, which shows the decay rate of the distribution tails.

2. The parameter β is called the *skewness parameter*, which shows the distribution direction to the left and right sides,

i.e., the positive and negative values of β skew the distribution to the right and left sides, respectively. When $\beta = 0$, a symmetric distribution is obtained.

3. The parameter γ is the *scale parameter*, which measures the distribution width.

4. the parameter δ is the *shift or location parameter*, which determines the rate at which the distribution peak has shifted.

Although we cannot generally express the Lévy distributions explicitly, we shall here introduce two special cases that have closed-form expressions.

- When $\alpha = 2$, we have the *Gaussian (Normal) distribution* defined as follows:

$$S(2, \beta, \gamma, \delta; x) = \frac{1}{\sqrt{8\pi\gamma}} \exp\left\{-\frac{(x-\delta)^2}{8\gamma}\right\} \quad -\infty < x < \infty.$$

  In this case, the variance and the mean of the distribution are given by $\sigma^2 = 2\gamma$, and $\mu = \delta$. The Gaussian distribution can thus be expressed in terms of its variance and mean as follows:

$$S(2, \beta, \sigma, \mu; x) = \frac{1}{\sqrt{4\pi\sigma^2}} \exp\left\{-\frac{(x-\mu)^2}{4\sigma^2}\right\} \quad -\infty < x < \infty. \tag{1.6}$$

- When $\alpha = 1$, we have the *Cauchy distribution* defined as follows:

$$S(1, \beta, \gamma, \delta; x) = \frac{\gamma}{\pi\left\{\gamma^2 + (x-\delta)^2\right\}} \quad -\infty < x < \infty.$$

It should be noted that in these two cases, the parameter β has no impact on the skewness of the distributions.

For $\alpha < 2$ and arbitrary skewness parameter β, the Lévy distributions asymptotically behave as a power-law of the following form:

$$\lim_{|x|\to\infty} S(\alpha, \beta, \gamma, \delta; x) \sim \alpha(1+\beta)C(\alpha)|x|^{-(\alpha+1)}, \tag{1.7}$$

where $C(\alpha) = \frac{1}{\pi}\Gamma(\alpha)\sin\left(\frac{\pi\alpha}{2}\right)$, and $\Gamma(.)$ denotes Euler's gamma function. In this case, the variance σ^2 about its mean with zero value is given by

$$\sigma^2 \approx \int_{-\infty}^{\infty} x^2 x^{-(\alpha+1)} dx = \frac{1}{2-\alpha} x^{2-\alpha}\Big|_{-\infty}^{\infty} = \infty,$$

That is the variance of a Lévy stable random variable with $\alpha < 2$ is infinite. It is worth noting that in the case of Gaussian distributions, $C(\alpha) = C(2) = 0$, and hence the tails go to zero as $|x| \to \infty$. Figure 1.2 shows the differences between a Lévy distribution with $\alpha = 1.5$, and a Gaussian distribution with $\alpha = 2$.

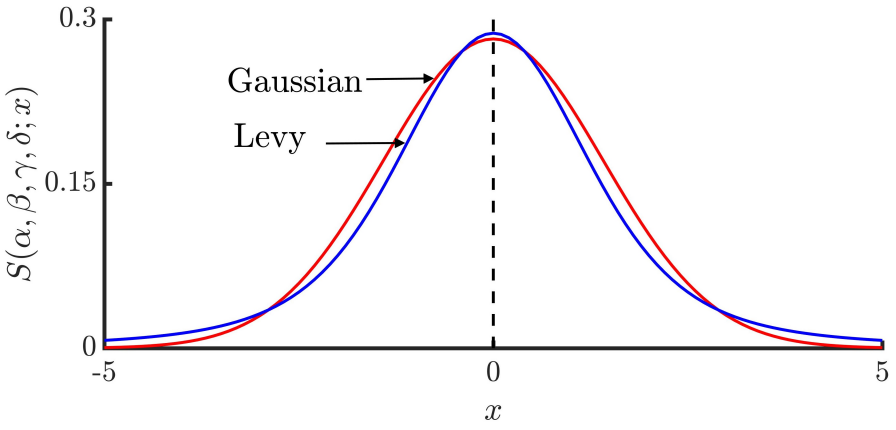

(a) For Lévy distribution, $\alpha = 1.5$, and for Gaussian, $\alpha = 2$. In all cases, $\beta = 0, \gamma = 1$, and $\delta = 0$.

Fig. 1.2: *Cont.*

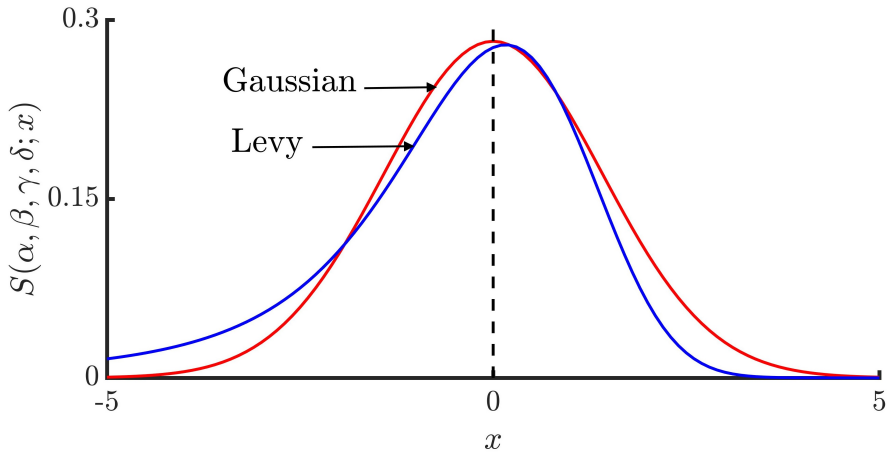

(b) For Lévy distribution, $\alpha = 1.5$, and for Gaussian, $\alpha = 2$. In all cases, $\beta = -1, \gamma = 1$, and $\delta = 0$.

Fig. 1.2: Illustration of the differences between Lévy and Gaussian distributions. A Lévy distribution leads to a heavy-tailed power-law asymptotic behaviour and its shape changes with different values of β. However, in the case of Gaussian distributions, the tails decay exponentially and the value of β has no impact on its shape.

A wide variety of phenomena can be described by the bell-shaped curve of the Gaussian distribution. This can be explained by the most important theorem in statistics, i.e., the *Central Limit Theorem* (CLT). The main idea of this theorem is indeed the description of the behaviour of the sum $Y_N = X_1 + X_2 + \cdots + X_N$, where X_1, $X_2 \cdots$, X_N are independent random variables, which have a common probability distribution function $f_X(x)$. According to this theorem, given the finite mean μ and finite variance σ^2, when N gets large, the random variable Y_N has a Normal distribution with the mean $N\mu$, and the variance $N\sigma^2$. For a long time, it was thought that the sum of a large number of independent and identically distributed random variables have always a Normal behaviour. But, a seminal work by the French mathematician Paul Lévy (Lévy, 1937) showed that the Gaussian distribution is a mem-

ber of Lévy distributions. Since the finite mean and finite variance of the random variables are the requirements for the so-called classical central limit theorem, this question arises:

Can the central limit theorem be extended in the case of the ensemble of random variables whose variances diverge?

Yes, the CLT can be generalized as follows: if we consider the sum $S_N = X_1 + X_2 + \cdots X_N$ of N independent and identically distributed random variables, which do not necessarily have a finite variance then the random variable S_N converges to a random variable whose pdf is a member of Lévy distributions family (Ibe, 2013).

Until now, we have discussed the mathematical and statistical aspects of the Lévy stable random variables whose pdf's have a power-law asymptotic behaviour for $\alpha < 2$. Now, this important question arises:

Similar to the ubiquitous Normal distributions, are there any examples of Lévy distributions in nature?

The answer to this question is "yes". After Paul Lévy, the so-called Lévy flight (henceforth referred to as LF) has been defined as a random walk process where the stochastic displacements made by a walker are Lévy stable random variables, i.e., their corresponding probability distribution function is a Lévy distribution with an asymptotic power-law behaviour as $\sim |x|^{-(\alpha+1)}$, where $|x|$ is the length of the displacements, and $\alpha < 2$. Since the searchers like animals make random movements with the aim of searching for targets in an environment, the Lévy flight is also called the Lévy flight foraging pattern. In the context of organisms movement, the existence of LF for the movement of ants was originally suggested by Shlesinger and Klafter (1986). Cole (1995) also recognized the LF pattern in the random movement of *Drosophila*. Later, the seminal work of Viswanthan (1996) confirmed the LF foraging pattern of sea birds, like *wandering albatross* and *Diomedea exulans*. Following

this paper, thanks to the advances in the methods of tracking the organism movements, such as GPS and satellite-tracking telemetry, the LF foraging patterns have been observed for a variety of organisms, including **social insects:** (1) Reynolds et al. (2007a) studied the movements pattern of displaced *honeybees* while foraging for their hives. The honey bees flight paths were recorded by using harmonic radars. They analysed their results statistically and showed that the bees adopt a LF to optimize their searching mechanisms. (2) *Bumblebees* can fly for long periods of time. They do not tend to land flowers that have been visited previously. This issue motivated Reynolds (2009) to analyse their movements so that they confirmed the existence of the LF searching pattern of bumblebees. (3) Miramontes et al. (2014) suggested that *termite workers* perform LF movements for developing social interactions and that such a strategy can secure them to search for nestmates and food, especially when they are scarce, and (4) The search pattern of the Australian desert *ant Melophorus bagoti* was studied by Reynolds et al. (2014). They found that these ants do random movements whose lengths are distributed exponentially when they are in familiar surroundings. However, when they are not certain about the location of their nests, they do random searches that can be described by a power-law distribution. **Marine predators:** Sims et al. (2008) statistically analysed the displacements of more than 10^6 movements made by different marine predators, such as *sharks, sea turtles, bony fishes, and penguins* and showed that the existence of Lévy flight pattern can lead to higher encounter rates for predators. **Mammals:** (1) Ramos-Fernández et al. (2004) tracked the daily movements of *spider monkeys* and found the evidence of a LF pattern with Lévy exponent $\alpha = 1.11$ for females. (2) Atkinson et al. (2002) showed a power-law distribution in the foraging of a species of African *jackals*, and (3) Regarding human movements, Brockmann et al. (2006) analysed a dataset of more than 10^6 displacements obtained by tracking the bank notes circulation in the United States and confirmed that human travelling exhibit a power-law behaviour as $\sim r^{-(\alpha+1)}$, where r is the displacements length and

$\alpha = 0.59$. **Micro-organisms:** The most important research on the existence of the Lévy foraging pattern of micro-organisms was undertaken by Harris et al. (2012). By using multi-photo microscopy, they tracked the movements of T cells in the mice brains during parasitic infection in the brain. They showed that T cells adopt the Lévy flight searching strategy to find infected brain cells. The pdf for the displacements behaves as a power law as $\sim l^{-(\alpha+1)}$, where l is the length of the displacements, and $\alpha = 1.15$.

In addition to these examples, the book by Viswanathan et al. (2011) is full of examples of species that seem to have adopted a Lévy search strategy and also nowadays, there are increasing interests that scientists show in pointing towards the existence of Lévy distributions in a wide range of particles. Besides the mathematical differences between Lévy and Normal distributions, these experiments compared the trajectories obtained by both distributions. Figure 1.3 illustrates the difference between the trajectories of Brownian motion and Lévy flights.

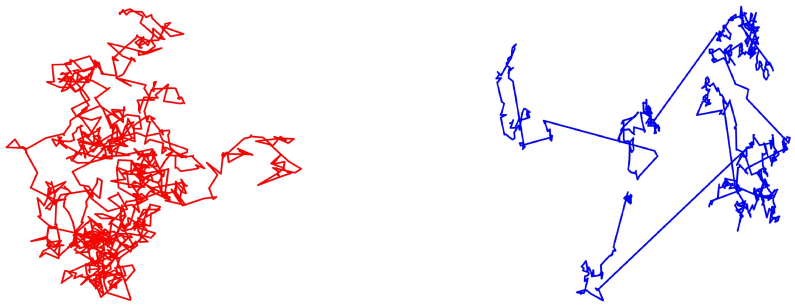

(a) Brownian motion ($\alpha = 2$) **(b)** Lévy flight ($\alpha = 1.5$)

Fig. 1.3: Illustration of differences between the trajectories of 10^3 displacements made by a walker that moves randomly in 2D. In the case of a Lévy distribution ($\alpha = 1.5$), the walker makes occasionally longer jumps between many short displacements.

In the case of a Lévy distribution, the particles make long jumps occasionally between many short displacements. Indeed, such a random search strategy enables species to decrease the probability to return to previous places they once visited. However, in the case of Normal distribution, the particles only make short movements so that some points can be revisited many times. Therefore, the Lévy flight foraging pattern could be an efficient strategy when the targets are distributed sparsely in an environment while the abundance of targets causes the foragers to make movements whose displacements have a Normal distribution.
Up to now, for a CTRW, we have introduced two types of pdfs for the displacements length, namely Gaussian distribution and a Lévy distribution with a power-law asymptotic behaviour. The next task is to mathematically define a pdf for the waiting times.

1.4 Mittag-Leffler distribution

For CTRW processes, similar to pdf's for the length of jumps, exponential and power-law waiting time distributions can also be considered. In the case of an exponential waiting time, the pdf $f_{\mathrm{T}}(t)$ is given by an exponential distribution with parameter $\lambda > 0$ as follows:

$$f_{\mathrm{T}}(t) = \lambda e^{-\lambda t}, \quad t \geq 0, \tag{1.8}$$

where $1/\lambda$ denotes the average time between successive steps made by the walker. In this case, the random process has a Markov (memoryless) property, i.e., its future state is dependent only on the present state and any information in the past is irrelevant.

As a generalization of the exponential distribution, the Mittag-Leffler waiting time distribution $\phi^{ML}(t)$ is given by the following density:

$$\phi^{ML}(t) = -\frac{d}{dt} E_\theta(-t^\theta), \qquad 0 < \theta < 1,$$

where $E_\theta(.)$ denotes the Mittag-Leffler function whose series representation is expressed as follows:

$$E_\theta(z) := \sum_{n=0}^{\infty} \frac{z^n}{\Gamma(\theta n + 1)}, \qquad z \in \mathbb{C}, \quad \theta > 0.$$

The waiting time density $\phi^{ML}(t)$ can also be expressed in terms of the Mittag-Leffler function in two parameters as follows:

$$\phi^{ML}(t) = t^{\theta-1} E_{\theta,\theta}(-t^\theta), \qquad 0 < \theta < 1, \tag{1.9}$$

where $E_{\theta,\eta}(.)$ denotes the generalized Mittag-Leffler function

$$E_{\theta,\eta}(z) := \sum_{n=0}^{\infty} \frac{z^n}{\Gamma(\theta n + \eta)}, \quad z \in \mathbb{C}, \quad \theta > 0, \quad \eta \in \mathbb{R}.$$

The Mittag-Leffler waiting time distribution $\phi^{ML}(t)$ has a power-law asymptotic behaviour for $t \to \infty$ as follows (Gorenflo and Mainardi, 2008b,a):

$$\phi^{ML}(t) \sim \frac{\sin(\theta\pi)}{\pi} \frac{\Gamma(\theta+1)}{t^{\theta+1}}. \tag{1.10}$$

In this case, the average waiting time defined by Eq. 1.1 is infinite, and the CTRW is no longer Markovian. Indeed, it is called as a long-memory process. In Figure 1.4, we show a sketch of the waiting time distribution ϕ^{ML} with $\theta = 0.5$ defined by Eq. 1.9 and its asymptotic behaviour, which highlights a power-law decaying tail as approximated in Eq. 1.10.

As examples of such processes, we can refer to (1) As explained previously, Harris et al. (2012) showed the heavy-tailed asymptotic behaviour for the T cells displacements in the brain. They also analysed the pdf for waiting times and confirmed that T cells pause between consecutive jumps for a time whose duration has a power-law asymptotic behaviour as $\sim t^{-(\theta+1)}$, where $\theta = 0.7$. (2)

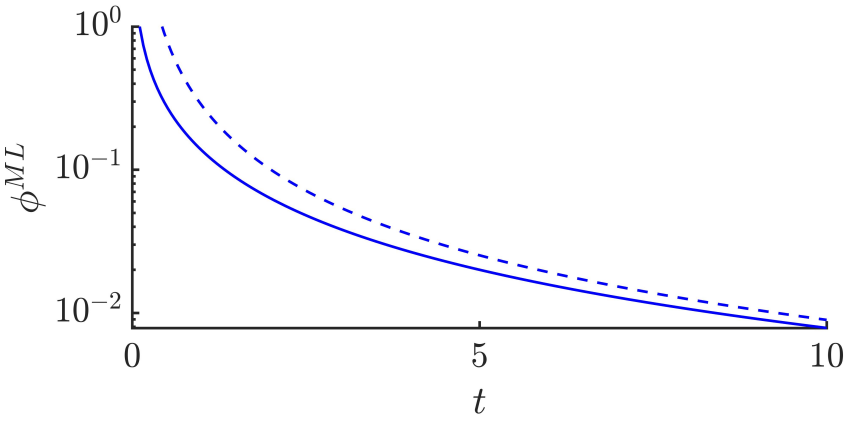

Fig. 1.4: Profile of the Mittag-Leffler waiting time distribution ϕ^{ML} obtained by Eq. 1.9 with $\theta = 0.5$. The dashed curve corresponds to the asymptotic behaviour approximated by Eq. 1.10, highlighting a power-law (algebraic) decaying tail of ϕ^{ML} for $0 < \theta < 1$. The y-axis is in the logarithmic scale.

Brockmann et al. (2006) also revealed a power-law behaviour pdf for human travelling as $\sim t^{-(\theta+1)}$, where $\theta = 0.6$, and (3) One of the most important studies on the application of the Mittag-Leffler function was introduced by the seminal work of Dokoumetzidis and Macheras (2009) in the field of pharmacokinetics. Based on the dataset of drugs, like amiodarone, a drug that is used to treat ventricular arrhythmias and atrial fibrillation, they found that the diffusion of this drug into the bone and spaces of deeper tissues is slow, and for a long time, the drug decays as a power-law, which can be well described by the Mittag-Leffler function.

1.5 From CTRW processes to diffusion equations

In this section, given a CTRW process with the exponential and power-law asymptotic behaviours of the displacement and waiting

time densities, we shall explain how diffusion equations can be derived by using the Master equation defined by Eq. 1.3.

Case (I). Let a large number of particles perform a CTRW such that the pdf for the jump length is a Normal distribution with $\mu_{\mathrm{X}} = 0$, and the pdf for the waiting time is an exponential distribution with parameter $\lambda > 0$ defined by Eqs. 1.6 and 1.8, respectively, i.e.,

$$f_{\mathrm{X}}(x) = \frac{1}{\sqrt{4\pi\sigma^2}} \exp\left\{-\frac{x^2}{4\sigma^2}\right\}, \qquad f_{\mathrm{T}}(t) = \lambda e^{-\lambda t}.$$

Here, the average waiting time $\mu_{\mathrm{T}} = 1/\lambda$, and the length variance $\sigma_{\mathrm{X}}^2 = 2\sigma^2$ are finite. The Fourier and Laplace transforms $\widehat{f_{\mathrm{X}}}(k)$ and $\widetilde{f_{\mathrm{T}}}(s)$ as $k \to 0$ and $s \to 0$ can be obtained as follows:

$$\widehat{f_{\mathrm{X}}}(k) \sim 1 - \sigma^2 k^2, \quad \text{and} \quad \widetilde{f_{\mathrm{T}}}(s) \sim 1 - s/\lambda.$$

By inserting the Fourier and Laplace transforms into the Master equation 1.3, we get

$$s\widetilde{\widehat{P}}(k,s) - \widehat{P}(k,0) = -Dk^2\widetilde{\widehat{P}}(k,s), \tag{1.11}$$

Where $D = \sigma_{\mathrm{X}}^2/2\mu_{\mathrm{T}}$. Considering the Laplace transform of the first-order derivative

$$\mathcal{L}\{g'(t)\} = s\tilde{g}(s) - g(0),$$

and inverting by Laplace, Eq. 1.11 is written in the following form:

$$\frac{\partial\widehat{P}(k,t)}{\partial t} = -Dk^2\widehat{P}(k,t)$$

Now, by considering the Fourier transform of the second-order derivative

$$\mathcal{F}\{f''(x)\} = -k^2\widehat{f}(k),$$

and inverting by Fourier, we obtain the following second-order diffusion equation:

$$\frac{\partial P(x,t)}{\partial t} = D\frac{\partial^2 P(x,t)}{\partial x^2}. \tag{1.12}$$

Here, such a CTRW process with both finite average waiting time and variance leads to a diffusion process known as **classical Brownian motion**.

Case (II). Let a large number of particles perform a CTRW such that the pdf's for the jump length and waiting time exhibit heavy-tailed asymptotic behaviour as follows:

$$f_{\mathrm{X}}(x) \sim |x|^{-(\alpha+1)}, \quad 1 < \alpha < 2 \quad \text{and} \quad f_{\mathrm{T}}(t) \sim t^{-(\theta+1)}, \quad 0 < \theta < 1.$$

First, by considering the Laplace transform of the two-parameter Mittag-Leffler function (Podlubny, 1998) as follows:

$$\mathcal{L}\left\{t^{\eta k+\theta-1}E^{(k)}_{\eta,\theta}(\pm a t^{\theta})\right\} = \frac{k! s^{\eta-\theta}}{(s^{\eta} \mp a)^{k+1}}$$

with $k = 0, \eta = \theta$, and $a = 1$, we get the Laplace transform of the waiting time density $\phi^{ML}(t)$ defined by Eq. 1.9 :

$$\widetilde{f_{\mathrm{T}}}(s) = \mathcal{L}\left\{t^{\theta-1}E_{\theta,\theta}(-t^{\theta})\right\} = \frac{1}{s^{\theta}+1}.$$

By putting $\widetilde{f_{\mathrm{T}}}(s)$ into Master equation 1.3, we get

$$s^{\theta}\widetilde{\widehat{P}}(k,s) - s^{\theta-1}\widehat{P}(k,0) = \left[\widehat{f_{\mathrm{X}}}(k) - 1\right]\widetilde{\widehat{P}}(k,s).$$

By introducing the Caputo fractional derivative in time

$${}^{C}_{0}D^{\theta}_{t} f = \frac{1}{\Gamma(1-\theta)}\int_0^t \frac{\partial f(\tau)/\partial\tau}{(t-\tau)^{\theta}}d\tau, \tag{1.13}$$

whose Laplace transform is

$$\mathcal{L}\left\{{}^{C}_{0}D^{\theta}_{t} f\right\} = s^{\theta}\widetilde{f}(s) - s^{\theta-1}f(0),$$

and inverting the Laplace transform, we get

$$ {}_0^C D_t^\theta \widehat{P}(k,t) = \left[\widehat{f_{\mathrm{X}}}(k) - 1\right] \widehat{P}(k,t). \tag{1.14} $$

According to Eq. 1.4, $\widehat{f_{\mathrm{X}}}(k)$ is given by $\widehat{\lambda}(k) = e^{\Lambda(k)}$, where

$$ \Lambda(k) = i\delta k - \gamma^\alpha |k|^\alpha (1 - i\beta \,\mathrm{sgn}(k) \tan \frac{\alpha\pi}{2}). \tag{1.15} $$

As $|k| \to 0$, we use the approximation $\widehat{f}_X(k) \approx 1 + \Lambda(k)$. Therefore, Eq. 1.14 can be written as follows:

$$ {}_0^C D_t^\theta \widehat{P}(k,t) = \Lambda(k) \widehat{P}(k,t). \tag{1.16} $$

By introducing the positive (left) ${}_{-\infty}D_x^\alpha$ and negative (right) ${}_xD_{+\infty}^\alpha$ Riemann-Liouville fractional derivatives in space:

$$ {}_{-\infty}D_x^\alpha f(x) = \frac{1}{\Gamma(n-\alpha)} \frac{\partial^n}{\partial x^n} \int_{-\infty}^{x} \frac{f(\xi)}{(x-\xi)^{\alpha-n+1}} d\xi, \tag{1.17} $$

$$ {}_xD_{+\infty}^\alpha f(x) = \frac{(-1)^n}{\Gamma(n-\alpha)} \frac{\partial^n}{\partial x^n} \int_{x}^{L} \frac{f(\xi)}{(\xi-x)^{\alpha-n+1}} d\xi, \tag{1.18} $$

where $n = 1 + [\alpha]$ such that $[\alpha] = \max\{m \in \mathbb{Z} | m \leq \alpha\}$ and $\mathbb{Z}$ is the set of integers. Here, we get $n = 2$ as in this study $1 < \alpha < 2$. The Fourier transforms of the left and right Riemann-Liouville can be obtained as follows:

$$ \mathcal{F}\{{}_{-\infty}D_x^\alpha f(x)\} = (ik)^\alpha \widehat{f}(k), \quad \text{and} \quad \mathcal{F}\{{}_xD_{+\infty}^\alpha f(x)\} = (-ik)^\alpha \widehat{f}(k) \tag{1.19} $$

Now, by assuming that $\delta = 0$, we write $\Lambda(k)$ defined by Eq. 1.15

in the following form:

$$\begin{aligned}
\Lambda(k) &= -\gamma^\alpha |k|^\alpha (1 - i\beta \operatorname{sgn}(k) \tan \frac{\alpha\pi}{2}) \\
&= -\gamma^\alpha |k|^\alpha \left[(\frac{1+\beta}{2} + \frac{1-\beta}{2}) - i(\frac{1+\beta}{2} - \frac{1-\beta}{2}) \operatorname{sgn}(k) \frac{\sin \frac{\alpha\pi}{2}}{\cos \frac{\alpha\pi}{2}} \right] \\
&= -\gamma^\alpha |k|^\alpha \left[\frac{1-\beta}{2} \left(1 + i \operatorname{sgn}(k) \sin \frac{\alpha\pi}{2} / \cos \frac{\alpha\pi}{2} \right) \right. \\
&\left. + \frac{1+\beta}{2} \left(1 - i \operatorname{sgn}(k) \sin \frac{\alpha\pi}{2} / \cos \frac{\alpha\pi}{2} \right) \right] \\
&= -\gamma^\alpha \left[\frac{1-\beta}{2\cos \frac{\alpha\pi}{2}} |k|^\alpha \left(\cos \frac{\alpha\pi}{2} + i \operatorname{sgn}(k) \sin \frac{\alpha\pi}{2} \right) \right. \\
&\left. + \frac{1+\beta}{2\cos \frac{\alpha\pi}{2}} |k|^\alpha \left(\cos \frac{\alpha\pi}{2} - i \operatorname{sgn}(k) \sin \frac{\alpha\pi}{2} \right) \right] \\
&= -\gamma^\alpha \left[\frac{1-\beta}{2\cos \frac{\alpha\pi}{2}} (ik)^\alpha + \frac{1+\beta}{2\cos \frac{\alpha\pi}{2}} (-ik)^\alpha \right] \qquad (1.20)
\end{aligned}$$

By inserting Eq. 1.20 into Eq. 1.16, we get

$$ {}_0^C D_t^\theta \widehat{P}(k,t) = \gamma^\alpha \left[l(ik)^\alpha + r(-ik)^\alpha \right] \widehat{P}(k,t), \qquad (1.21)$$

where $l = -\dfrac{1-\beta}{2\cos \frac{\alpha\pi}{2}}$ and $r = -\dfrac{1+\beta}{2\cos \frac{\alpha\pi}{2}}$.

By inverting the Fourier transform and considering Eq. 1.19, we get the following space-time fractional order diffusion equation:

$$ {}_0^C D_t^\theta P(x,t) = \gamma^\alpha \left[l {}_{-\infty} D_x^\alpha P(x,t) + r {}_x D_{+\infty}^\alpha P(x,t) \right]. \qquad (1.22)$$

Here, such a CTRW process with diverging average waiting time and/or infinite variance of the jump length leads to a diffusion process known as **anomalous diffusion**.

Most of the experimental studies evaluate the type of diffusion processes by using the mean-squared displacement (MSD) of the particles doing random movements. The MSD can be approximated by $\sim \int_{-\infty}^{\infty} x^2 P(x,t)dx$, where $P(x,t)$ is the probability of finding the particles at x at time t, which is the solution of diffusion Eqs. 1.12 and 1.22. In the case of Normal diffusion processes (Brownian motion), the MSD behaves linearly as $\sim t$. However, in the case of anomalous diffusion processes, the MSD exhibits a power-law behaviour as $\sim t^{\zeta}$, where $0 < \zeta < 2$. Anomalous diffusion processes can be categorized by the scaling exponent ζ. When $0 < \zeta < 1$, we get sub-diffusion processes in which the particles spread slower than expected from classical Brownian motion, as the particles tend to wait longer between jumps, which yields a power-law asymptotic behaviour for the waiting time pdf. When $1 < \zeta < 2$, we get super-diffusion processes in which the particles spread faster than expected from classical Brownian motion. In that case, the pdf for jumps has a power-law asymptotic behaviour. It should be noted that the solutions of diffusion Eqs. 1.12 and 1.22 can also represent the concentration (density) of particles $C(x,t)$, as the number of particles per unit length at position x at time t. Because if we consider N particles with the same probability $P(x,t)$ then $C(x,t) = NP(x,t)$ also satisfies the resulting diffusion equations.

One of the negative characteristics of (pure) Lévy flight distributions is divergent variance and mean. Therefore, the walker can make displacements with arbitrary lengths. But, the physiological and environmental constraints can prevent such long displacements. Therefore, Mantegna and Stanley (1994) introduced truncated (also called tempered) Lévy flights (TLF) distributions, leading to a finite variance. In fact, the power-law behaviour of the Lévy distribution tails is retained in a finite space. However, the sum of a large number of random variables with TLF distributions behaves like a Gaussian distribution. Rosiński (2007) proposed exponentially TLF distributions, which are asymptotically defined as $\sim e^{-\lambda x}|x|^{-(\alpha+1)}$, where λ is a truncation parameter with SI units

of m^{-1}. With the TLF assumption, we can derive truncated space-fractional-order diffusion equations whose derivations are ignored here. For more details refer to del Castillo-Negrete (2009).

When considering the concept of the CTRW processes and using the Master equation, time and/or space fractional-order equations can be obtained with a power-law asymptotic behaviour assumption for the waiting times and/or jump lengths pdf's. Therefore, one can replace integer-order operators with fractional-order ones, which have a meaningful connection with experiments. Although there are increasing works on detecting the Lévy flight foraging patterns of organisms, nowadays, studies on the resulting space fractional-order diffusion models are related to the theoretical fractional calculus rather than to practical uses in ecology, epidemiology, and biology. While classical diffusion models have been used extensively in those fields for many years, fractional-order versions are much more recent and should be further studied.

1.6 Scope of the thesis

The goal of the present thesis is to study the application of fractional-order diffusion models in immunology and epidemiology. In the context of immunology, as mentioned previously, human T cells follow Lévy flights during parasitic infection in the brain. This fact has motivated us to study the influence of such a movement pattern on the efficacy of the immune system. In the context of epidemiology, the most important work has been done by Hanert et al. (2011), which studies the impact of human travels following Lévy flight on the propagation of epidemics caused by infectious diseases. As the second application, by considering TLF distributions, we develop the model proposed by Hanert et al. (2011).
In what follows, some key questions are raised about these two issues and the subsequent chapters are concerned with their answers.

1.6.1 Space fractional diffusion models in immunology

$CD8^+$ T cells are the most important immune cells that protect the body against pathogens, such as viruses and parasites. In their search for infected cells and pathogens in the body tissues, they need to move. They can thus do their protective mechanisms, such as controlling the growth of intracellular pathogens and killing infected cells. Immunologists have conducted experiments on the movement of the immune cells and confirmed the existence of random and directional movements. In the case of random movements, it was shown that the diffusion process of T cells in some organs is Brownian motion (Miller et al., 2002; Wei et al., 2003). However, later, Harris et al. (2012) confirmed the existence of the Lévy flight foraging pattern of T cells in the brain during a parasitic infection, known as Toxoplasma gondii. Now, the switch from Brownian motion to Lévy flight of T cells has raised this main question.

In comparison to Brownian motion, what advantages does the immune system gain from a Lévy flight searching strategy?

Since the main aim of T cells is to destroy infected cells, one way to answer this general question is to understand *how Lévy flight and Brownian motion searching influence the spatial elimination dynamic and the time evolution of infected brain cells when T cells are killing them.* In Chapter 2, a space-fractional diffusion-order model for the T cells density in the brain and also a mathematical model representing the T cells response to infected cells are presented and the results of classical and fractional models are compared.

It is worth noting that in immunology, fractional-order models have been only derived based on the time-fractional operators, like Caputo defined by Eq. 1.13 (Jajarmi and Baleanu, 2018; Baleanu et al., 2020c). However, space-fractional-order diffusion models defined by Riemann-Liouville operators defined by Eqs. 1.17 and 1.18

have not been used to study the super-diffusion of T cells. Therefore, adopting such an approach in chapter 2 is a new work that illuminates our understanding of the impact of LF displacements of T cells on the spread of infection in the organs of the body.

1.6.2 Space fractional diffusion models in epidemiology

An epidemic is the geographic propagation of an infectious disease that can sometimes spread globally, leading to a pandemic. The speed at which epidemics spreads like waves across an area is dependent on the random motion pattern of individuals. In the case of a Brownian motion, the epidemic waves travel at a constant speed. However, In the case of a Lévy flight, the pathogens can travel larger distances due to the long jumps of infected hosts between short movements. In that case, the epidemic speed grows exponentially. For the former, the speed is obtained by a second-order diffusion model, and for the latter, it is obtained by a space-fractional-order epidemic model.

On the basis of work carried out by del Castillo-Negrete (2009), which investigated the impact of the truncation parameter for the truncated fractional-order Fisher–Kolmogorov equation, in Chapter 3, we propose a truncated space-fractional-order epidemic model and discuss the epidemic speed based on different values of the truncation parameter. Indeed, our aim is to find an answer to the following question by analytical and numerical methods:

How does the truncation parameter affect the propagation pattern of epidemic waves?

In this case, we consider a simple epidemic model, in general, that is formulated based on the directly transmission mechanism of pathogens.

Following Chapter 3, of great importance is to explore the obtained results for a more realistic model and also to derive useful/usable conclusions. Therefore, in Chapter 4, we extend the truncated space-fractional-order models to the West Nile virus epidemic, which happens by indirectly transmission mechanism of viruses, and then we numerically solve the model with the parameter values based on observations. The results of this chapter will answer the following key question:

What potentials/benefits do the truncated space-fractional-order diffusion equations have for the epidemic models?

Indeed, in this work, we extend the implications of a truncated fractional-order Fisher–Kolmogorov equation to epidemic models consisting of two coupled diffusion-reaction equations, which have not previously been studied.

Supporting publications

Farhadi, A., Hanert, E. (2022). A fractional diffusion model of $CD8^+$ T cells response to parasitic infection in the brain. Mathematical Modelling of Natural Phenomena, 17, 3.
doi: 10.1051/mmnp/2022003

Farhadi, A., Hanert, E. (2022). Front Propagation of Exponentially Truncated Fractional-Order Epidemics. Fractal and Fractional, 6(2), 53.
doi: 10.3390/fractalfract6020053

Farhadi, A., Hanert, E. (2022) A tempered space fractional-order diffusion model of West Nile virus epidemics. Journal of mathematical biology (Submitted)

CHAPTER 2

A fractional diffusion model of CD8$^+$ T cells response to parasitic infection in the brain

This chapter reproduces the following article[1]:

A. Farhadi, E. Hanert, A fractional diffusion model of CD8$^+$ T cells response to parasitic infection in the brain, *Mathematical Modelling of Natural Phenomena*, 2022,
doi: 10.1051/mmnp/2022003

Abstract

Toxoplasma gondii (T. gondii) is a parasitic pathogen that causes serious brain diseases in fetuses and patients

[1]Only minor modifications were made.

with immunodeficiency, particularly AIDS patients. In the field of immunology, a large number of studies have shown that effector CD8$^+$ T cells can respond to T. gondii infection in the brain tissue through controlling the proliferation of intracellular parasites and killing infected brain cells. These protective mechanisms do not occur without T cell movement and searching for infected cells, as a fundamental feature of the immune system. Following infection with a pathogen in a tissue, in their search for infected cells, CD8$^+$ T cells can perform different stochastic searches, including Lévy and Brownian random walks. Statistical analysis of CD8$^+$ T cell movement in the brain of T. gondii-infected mouse has determined that the search strategy of CD8$^+$ T cells in response to infected brain cells could be described by a Lévy random walk. In this work, by considering a Lévy distribution for the displacements, we propose a space fractional-order diffusion equation for the T cell density in the infected brain tissue. Furthermore, we derive a mathematical model representing CD8$^+$ T cell response to infected brain cells. By solving the model equations numerically, we perform a comparison between Lévy and Brownian search strategies. we demonstrate that the Lévy search pattern enables CD8$^+$ T cells to spread over the whole brain tissue and hence they can rapidly destroy infected cells distributed throughout the brain tissue. However, with the Brownian motion assumption, CD8$^+$ T cells travel through the brain tissue more slowly, leading to a slower decline of the infected cells faraway from the source of T cells. Our results show that a Lévy search pattern aids CD8$^+$ T cells in accelerating the elimination of infected cells distributed broadly within the brain tissue. We suggest that a Lévy search strategy could be the result of natural evolution, as CD8$^+$ T cells learn to enhance the immune system efficiency against pathogens.

2.1 Introduction

After the discovery of the Toxoplasma gondii (T. gondii) parasite in 1907, it has been extensively studied in various fields, such as morphology, immunology, and identification of diseases caused by T. gondii parasite (Weiss and Kim, 2011; McCabe et al., 1990). From a morphological point of view, there are different forms of the T. gondii parasite that lead to a complex life cycle for T. gondii and widespread infection in almost all warm-blooded vertebrate hosts (Dubey, 2016). Initially, T. gondii oocysts are created in the body of cats, as definitive hosts and then transferred to their feces, which can contaminate the environment, such as soil, water, and food. Subsequently, through the transmission of oocysts into the bodies of secondary hosts, other types of T. gondii parasites, known as tachyzoites and bradyzoites, are formed. In humans, T. gondii can be perilous for the fetus during pregnancy and cause congenital diseases, known as toxoplasmosis, such as hydrocephalus, microcephaly, and blindness (Hampton, 2015). T. gondii parasites can maintain their survival in the brain tissue through the slow proliferation of bradyzoites and the creation of tissue cysts in different types of brain cells (Wohlfert et al., 2017). In adults, following Toxoplasma infection in the brain, in addition to the possibility of developing psychiatric disorders, like schizophrenia (Torrey and Yolken, 2003), the transformation of tissue cysts into free tachyzoites can jeopardize the life of patients suffering from immunodeficiency, particularly AIDS patients (Ferguson et al., 1989; Luft and Remington, 1988). This issue highlights the importance of the immune system in controlling the proliferation of tachyzoites, which are capable of rapid division within the brain cells (Denkers and Gazzinelli, 1998).

The human body is equipped with a complicated and ingenious system, known as the immune system that is composed of molecules, such as cytokines and chemokines, and numerous cells, like B cells and T cells. The goal of the immune system is to combat pathogenic organisms, like bacteria, viruses, and parasites in

the body leading to the control of the pathogen growth and the elimination of the infected cells from the host body. There are two main groups of immune responses: innate immunity and adaptive immunity. Innate immunity includes the first reactions of the immune system against pathogens that enter the body, like changes in the temperature of the host body and nonspecific mechanisms of the innate immune cells, such as the secretion of cytokines that promote the proliferation of other immune cells. These initial mechanisms are not sufficient to clear an infection. However, adaptive immunity comprises specific mechanisms that lead to the neutralization of pathogens through antibodies produced by B cells and the destruction of infected cells by CD8$^+$ T cells. Although innate and adaptive cells have different biological functions, they are closely linked to each other. For instance, in the case of T. gondii infection, initially, the innate immune cells, such as dendritic cells respond to T. gondii tachyzoites. One of these responses is to secrete molecules, like IL$-$12. Then, CD8$^+$ T cells, as the adaptive immune cells, are stimulated by IL$-$12 leading to the secretion of other molecules, such as cytokine IFN$-\gamma$ that can control the growth of intracellular parasites and help T cells to penetrate the brain, as protective and regulatory mechanisms, respectively (Gazzinelli et al., 1994; Wang et al., 2007). Thus, CD8$^+$ T cell deficiency causes inadequate production of the cytokine IFN$-\gamma$, which triggers the multiplication of a large number of tachyzoites in the brain tissue. For more details on basic concepts in immunology, refer to the book (E Paul, 2003) by E. Paul.

Over the last decade, as a fundamental characteristic of the immune system, the movement of immune cells in the body and search patterns in different tissues, including lymph nodes (Wei et al., 2003), skin (Ariotti et al., 2015), brain (Harris et al., 2012), and lungs (Mrass et al., 2017) have been considerably studied. As soon as pathogens enter the body, the immune cells need to move continuously and search for different types of cells, like infected cells in various tissues. For instance, upon infection, naïve T cells, i.e., nonactivated T cells search for antigen-presenting cells, especially

dendritic cells (DCs) in the lymph nodes. Following interactions with DCs, they can convert into effector $CD8^+$ T cells. Effector T cells then move toward infected tissues where they search for infected cells so that they can perform their protective mechanisms. Therefore, the movement of T cells and their search for pathogens during an infection in the body are essential for immune system activities. T cell movement could have two components: directional movement (chemotaxis) and stochastic motion. By chemotaxis, T cells are directed to the infected organs by chemical signals, such as chemokines (Witt et al., 2005; Okada et al., 2005). For example, Landrith et al. (2015) have examined how effector $CD8^+$ T cells are recruited into the T. gondii-infected brain tissue by adhesion molecules, VCAM-1, VLA-4, and chemokines CXCL9/10. However, studies of T cell motility in tissues have proposed that similar to foraging animals, T cells do a random search for their targets (Wei et al., 2003; Miller et al., 2002). Analysis of these random motions suggests two types of search strategy: Brownian motion and Lévy movement. In complex diffusion processes, occasional large jumps between many short displacements can be considered as a distinctive characteristic of a Lévy random walk (RW) versus a Brownian motion. In that case, for a Lévy RW, the probability distribution function (pdf) for the random movements is obtained by a heavy tail distribution with an asymptotic behaviour as $\sim l^{-(\alpha+1)}$, where l is the length of the displacements and $0 < \alpha < 2$ (Metzler and Klafter, 2000). Figure 2.1 shows three sample random displacements of a particle following a Lévy RW. In all cases, initially, the walker is placed at the origin $(x, y) = (0, 0)$ and randomly makes 10^3 steps with different values of α. As the value of α increases, the probability of large displacements decreases so that with $\alpha = 2$, a classical Brownian motion is obtained. For more details on the simulation of Lévy distributions refer to (Chambers et al., 1976; Weron and Weron, 1995). So the existence of large jumps for Lévy RWs enables T cells to travel large distances within the tissues to find their targets.

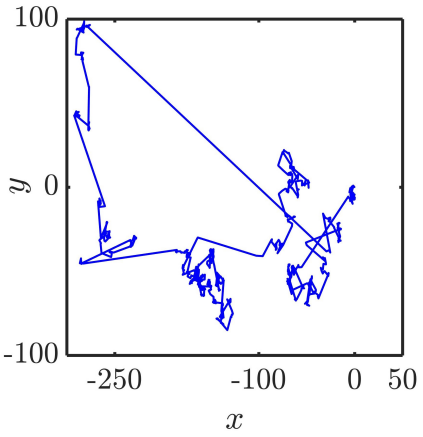

(a) Lévy RW, $\alpha = 1.15$.

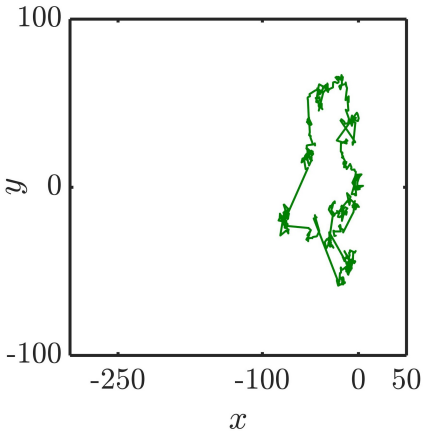

(b) Lévy RW, $\alpha = 1.5$.

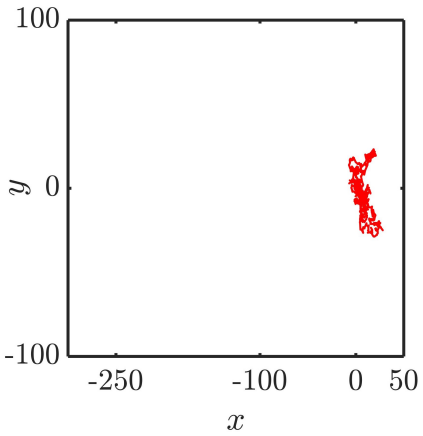

(c) Brownian motion, $\alpha = 2$.

Fig. 2.1: Illustration of the difference between Lévy and Brownian RWs based on the trajectories of their displacements. All trajectories are drawn from a Lévy distribution with different values of α. (a) and (b) In the case of a Lévy RW, there are large jumps between short displacements. (c) As the value of α increases, the probability of large displacements decreases so that with $\alpha = 2$, a classical Brownian motion is obtained.

Studies have shown that due to finding rare DCs and also the lack of information on the exact location of DCs in the lymph nodes, naïve T cells perform a random search that can be described by a Brownian RW (Preston et al., 2006; Riggs et al., 2008). However, the search pattern of effector $CD8^+$ T cells in a peripheral tissue where the tissue is injured by pathogens could be represented by a Lévy RW or a Brownian motion, depending on factors, such as the type of infection and the features of infected tissues. For instance, Effector T cells in inflamed lungs can have a similar foraging pattern to naïve T cells (Moses et al., 2019). However, Harris et al. (2012) observed that $CD8^+$ T cells perform a Lévy RW search strategy in the brain of T. gondii-infected mouse. The difference between T cell search patterns in lymph nods and peripheral tissues may result from factors, such as the properties of tissue and intrinsic differences between nonactivated and effector $CD8^+$ T cells (Krummel et al., 2016).

In addition to $CD8^+$ T cells in the T. gondii-infected brains, there are many species that perform a Lévy RW search for their targets. Some of these species are listed as follows: jackals (Atkinson et al., 2002), spider monkeys (Boyer et al., 2006), honeybees (Reynolds et al., 2007a,b), bumblebees (Lihoreau et al., 2016), fruit flies (Reynolds and Frye, 2007), and large marine predators (Sims et al., 2008; Humphries et al., 2010). In the field of modelling a large number of random walkers, such as living organisms following a specific random motion in an environment, diffusion equations for the density of the random walkers can be obtained. These equations consist of terms with time and space derivatives. For a Brownian motion, a Gaussian probability distribution function (pdf) for the displacements leads to a second-order diffusion equation (Okubo and Levin, 2013). However, for a Lévy RW, a power-law asymptotic behaviour of the pdf for the displacements results in a space-fractional-order diffusion equation with order $1 < \alpha < 2$. In some anomalous diffusion processes, the random walkers tend to pause between displacements, and hence they diffuse slower than predicted by a Brownian motion. Therefore, the pdf for waiting

times between jumps exhibits a power-law asymptotic behaviour. In that case, a time-fractional-order equation with order $0 < \gamma < 1$ is obtained. However, in the case of a Brownian motion, considering a Poissonian pdf for the pausing times leads to a time integer-derivative with order $\gamma = 1$ (Metzler and Klafter, 2000). In recent years, such modelling using fractional derivatives has been applied to a broad range of problems in finance (Scalas et al., 2000; Cartea and del Castillo-Negrete, 2007b), plasma turbulence (del Castillo-Negrete et al., 2004, 2005), epidemiology (Hanert et al., 2011; Hanert, 2012), ecology, and biology (Raghib et al., 2010; Vallaeys et al., 2017). As well as the applications of fractional calculus, designing efficient numerical methods for solving the fractional models is one of the key issues that has been widely studied (Baleanu et al., 2020a; Jajarmi and Baleanu, 2020; Sajjadi et al., 2020; Baleanu et al., 2020b; Jajarmi and Baleanu, 2021; Mohammadi et al., 2018).

In immunology, mathematical models have been widely applied to study the dynamics of host immune responses to tumour cells and viral infections, like hepatitis, human immunodeficiency virus (HIV), and influenza in the form of an ordinary differential system of equations with integer or fractional orders (see for instance (Kuznetsov et al., 1994; Ding and Ye, 2009)). In these models, the interactions between viruses or infected cells and immune responses are considered as predator-prey dynamics, i.e., viruses and infected cells are the prey and CD8$^+$ T cells are the predators. In recent years, researchers have tried to examine the interplay between viruses or tumour cells and immune system cells based on their spread or movements in the organs of the body (Bocharov et al., 2016; Chaplain and Matzavinos, 2006). The resulting models are in the form of a system of reaction and diffusion equations. In these models, it is assumed that T cells search for viruses or tumour cells based on a Brownian motion, and viruses and tumour cells proliferate logistically and spread in the injured tissues relying on a Brownian dispersion.

Observation of the Lévy RW pattern performed by CD8$^+$ T cells in their search for the T. gondii infected brain cells has led

to more studies on such a pattern of the movement in the body (Cannon et al., 2014; Li et al., 2015). Therefore, following such studies, it would be essential to derive appropriate mathematical models based on the Lévy RW that can shed some light on differences with the classical Brownian motion, which has been also observed in the immune system. Such modelling based on the Lévy random motion leads to space-fractional-order diffusion equations. However, recently, in the field of immunology, fractional-order models of infections, such as HIV have been just designed relying on the time-fractional operators (Jajarmi and Baleanu, 2018; Baleanu et al., 2020c; Ali et al., 2020). In these models, $CD4^+$ T cells, as the immune cells, are the target of HIV infection, and the dynamics of free HIV particles, healthy and infected $CD4^+$ T cells have been investigated by numerical and analytical methods. For instance, Baleanu et al. (2020c) performed a comparison of their results by applying ordinary, Caputo, and Caputo-Fabrizio time-fractional operators to their models. However, Ali et al. (2020) introduced a new fractional model by using the conformable fractional derivative and examined the analytical and numerical solutions of their model. However, in these models, the effect of the $CD8^+$ T cells on HIV infection has not been considered. Hence, to our knowledge, applying space-fractional-order operators to modelling the immune system response to infection has been ignored. This is obviously a serious knowledge gap since the function of the immune system is necessarily dependent on the movement of T cells. Thus, the aim of this study is to address this knowledge gap by applying the Lévy foraging pattern of T cells to the spatio-temporal modelling of the interaction between $CD8^+$ T cells and bradyzoite-infected cells during T. gondii infection in the brain. Here, the main idea will be to understand how the Lévy RW of $CD8^+$ T cells can lead to an efficient immune response to the infected brain cells. Therefore, the fractional-order model results will be compared with the results obtained with the classical model to highlight the effect of Lévy RW on killing infected cells distributed broadly within the brain tissue.

We organize the remainder of the paper in the following struc-

ture. In the next section, we derive a space-fractional-order diffusion equation for the CD8$^+$ T cells density and also a space-time model describing the interactions between CD8$^+$ T cells, healthy and infected brain cells. We discuss the system parameters and the estimation of their values in Section 2.3. A numerical method for solving space-fractional-order diffusion equations is applied in Section 2.4. Our model is then used to estimate the efficiency of effector CD8$^+$ T cells for a Lévy RW versus a Brownian motion in Section 2.5, and in the last section, we finish the paper with a review of the results and also some suggestions for future work.

2.2 Model description

In this paper, our goal is to investigate the efficacy of a Lévy search pattern performed by effector CD8$^+$ T cells in the T. gondii-infected brain tissue. When effector T cells enter the brain, they perform random searches to find the infected brain cells. Therefore, we can study the impact of a Lévy random search on the density of infected cells distributed throughout the brain tissue. To do so, we first derive a model with non-local diffusion representing the density of CD8$^+$ T cells, and then according to the T. gondii life cycle in the brain, we shall formulate a model composed of three coupled equations representing the density of healthy and infected brain cells in space and time with no diffusion term.

2.2.1 Modelling the superdiffusion of CD8$^+$ T cells

Like viral pathogens, as a result of T. gondii parasites entering the body, naïve T cells located in the lymph nodes are activated and proliferate due to interactions with dendritic cells. Activated or effector CD8$^+$ T cells can then do their protective mechanisms in the infected tissues of the body, including the brain tissue (John et al., 2009).

It is worth noting that $CD8^+$ T cells can infiltrate into the brain parenchyma (gray and white matter) only during infection (Hawkins and Davis, 2005). In the pathway of $CD8^+$ T cells toward the brain tissue, there are barriers, known as blood-brain barriers (BBBs) that control the penetration of the immune cells into the brain parenchyma (Wilson et al., 2010). However, $CD8^+$ T cells can overcome such barriers through a series of steps leading to a directed migration of $CD8^+$ T cells into the brain tissue. In (Landrith et al., 2015), for T cell infiltration into the brain parenchyma during T. gondii infection, a process consisting of three steps has been considered. Initially, the speed of $CD8^+$ T cells moving in the blood vessels is slowed down by the adhesion molecules. At the next step, they can infiltrate into the perivascular space, and eventually, chemokines lead them to the brain parenchyma. When $CD8^+$ T cells reach the brain, they do random searches for their targets, i.e., infected brain cells. The properties of such random searches have been studied by Harris et al. (2012).

From a statistical point of view, there are basic properties for Brownian and Lévy RWs that can be used to understand their differences. One of these properties is the mean-square displacement (MSD). If the MSD grows linearly as a function of time, the random motion can be described by a Brownian RW, while a nonlinear growth of the MSD represents a Lévy RW. By considering this property, the random search strategy of living organisms in an environment can be determined. For instance, Harris et al. (2012) examined the movement of $CD8^+$ T cells in the brain of T. gondii-infected mouse and suggested that the MSD grows superlinearly, i.e., $< x^2 > \sim t^{1.4}$. It means that a Lévy RW search pattern is adopted by $CD8^+$ T cells in response to Toxoplasma infection in the brain. In that case, $CD8^+$ T cells can diffuse within the brain tissue faster than expected from a Brownian motion leading to superdiffusion. Another property is the probability distribution function (pdf) for the jumps of the random walker. For a Brownian RW, the pdf is a Gaussian function. However, in the case of a Lévy RW, the pdf exhibits a power-law asymptotic behaviour. For instance,

based on the statistical analysis of T cell movement in the infected brain (Harris et al., 2012), the pdf for the displacements of CD8$^+$ T cell has a power-law asymptotic behaviour as $\sim |x|^{-(\alpha+1)}$, where $|x|$ is the length of displacements and $\alpha = 1.15$. Thus, when CD8$^+$ T cells enter the brain tissue from a source, with non-zero probability, they can make large displacements in the brain tissue. For more details on the properties of Lévy and Brownian RWs, refer to (Klafter and Sokolov, 2011).

To derive a fractional-order diffusion equation representing the density of CD8$^+$ T cells in the T. gondii-infected brain, we shall consider the continuous-time random walk (CTRW) processes consisting of a large number of walkers (here T cells) that make random jumps, $x_1, x_2, ..., x_i, ...$ at times $t_1, t_2, ..., t_i, ...$ As the displacements x_i and the waiting times $\tau_i = t_i - t_{i-1}$ are random variables, we define the probability distribution functions (pdf's) $\eta(x)$ and $\psi(\tau)$ for the jumps and waiting times, respectively. By considering a separable CTRW and given τ and ψ, we can get the probability of finding a walker $P(x,t)$ at place x and time t by the Montroll-Weiss equation (Montroll and Weiss, 1965) in Fourier-Laplace form as follows:

$$\widetilde{\widehat{P}}(k,s) = \frac{1-\widetilde{\psi}(s)}{s}\frac{1}{1-\widetilde{\psi}(s)\widehat{\eta}(k)}, \tag{2.1}$$

where $\widetilde{\psi}(s)$ and $\widehat{\eta}(k)$ are the Laplace and Fourier transforms of the pdf's ψ and η, respectively defined as follows:

$$\mathcal{L}\{\psi\} = \widetilde{\psi}(s) = \int_0^{+\infty} e^{-st}\psi(t)dt, \quad \mathcal{F}\{\eta\} = \widehat{\eta}(k) = \int_{-\infty}^{+\infty} e^{ikx}\eta(x)dx.$$

Different CTRW processes can be obtained by different asymptotic behaviours of the jump and waiting time pdf's, which lead to whether integer- or fractional-order diffusion equations. For example, we suppose that the pdf's for the waiting times and jumps exhibit heavy-tailed (power-law) asymptotic behaviours as follows:

$$\psi(\tau) \sim \tau^{-(\gamma+1)}, \qquad \eta(x) \sim |x|^{-(\alpha+1)}, \tag{2.2}$$

where $0 < \gamma < 1$ and $1 < \alpha < 2$. If we use the fact that

$$\mathcal{F}[{}_{-\infty}D_x^{\alpha} f] = (-ik)^{\alpha}\widehat{f}, \quad \mathcal{F}[{}_xD_{+\infty}^{\alpha} f] = (ik)^{\alpha}\widehat{f},$$

and

$$\mathcal{L}[{}_0^C D_t^{\gamma} f] = s^{\gamma}\widetilde{f} - s^{\gamma-1}f(0),$$

where $f(0)$ is the initial condition, ${}_{-\infty}D_x^{\alpha}$ and ${}_xD_{+\infty}^{\alpha}$ are the positive (left) and negative (right) space-fractional-order Riemann-Liouville operators, and ${}_0^C D_t^{\gamma}$ is the time-fractional-order Caputo operator defined as:

$$
\begin{aligned}
{}_{-\infty}D_x^{\alpha} f &= \frac{1}{\Gamma(2-\alpha)}\frac{\partial^2}{\partial x^2}\int_{-\infty}^{x}\frac{f(\xi)}{(x-\xi)^{\alpha-1}}d\xi, \\
{}_xD_{+\infty}^{\alpha} f &= \frac{(-1)^2}{\Gamma(2-\alpha)}\frac{\partial^2}{\partial x^2}\int_{x}^{\infty}\frac{f(\xi)}{(\xi-x)^{\alpha-1}}d\xi, \\
{}_0^C D_t^{\gamma} f &= \frac{1}{\Gamma(1-\gamma)}\int_0^t \frac{\partial f(\tau)/\partial\tau}{(t-\tau)^{\gamma}}d\tau,
\end{aligned}
$$

where $\Gamma(.)$ denotes Euler's gamma function, by taking the inversion of the Laplace and Fourier transforms of Eq. (2.1), one can then find the following space-time fractional-order diffusion equation:

$${}_0^C D_t^{\gamma} P(x,t) = K_{\alpha,\gamma}\left[\frac{1-\beta}{2}{}_{-\infty}D_x^{\alpha}P(x,t) + \frac{1+\beta}{2}{}_xD_{+\infty}^{\alpha}P(x,t)\right], \tag{2.3}$$

where coefficient $K_{\alpha,\gamma}$ represents a generalised diffusivity whose dimension is $[K_{\alpha,\beta}] = \mathrm{m}^{\alpha}\mathrm{s}^{-\gamma}$ and the parameter $\beta \in [-1,1]$ is a skewness parameter that shows a preferred direction of displacements that can be seen in heterogeneous systems. When $\beta = 0$, the distribution is symmetric and space derivative represents a symmetric Riesz derivative. For more details on the derivation of Eq. (2.3), refer to (Metzler and Klafter, 2000; Cartea and del Castillo-Negrete, 2007a). Here, we note that by defining the concentration of walkers $C(x,t)$ in one dimension as the number of walkers per unit length at position x and time t and assuming that there are N

random walkers in total with the same probability $P(x,t)$, we can easily see that $C(x,t) = NP(x,t)$ also satisfies Eq. (2.3).

As an application of Eq. (2.3) to obtain the concentration of walkers following a CTRW defined by (2.2), by considering a large number of CD8$^+$ T cells following a superdiffusion in the T. gondii-infected brain tissue and the fact that the pdf for the T cell displacements has a power-law asymptotic behaviour with order α, where $\alpha = 1.15$, in one dimension, the concentration (density) of CD8$^+$ T cells $E(x,t)$ at position x and time t with the dimensions of the number of T cells per unit length is the solution of the following space-fractional-order diffusion equation:

$$\frac{\partial E(x,t)}{\partial t} = K_\alpha \left[\frac{1-\beta}{2} {}_0D_x^\alpha E(x,t) + \frac{1+\beta}{2} {}_xD_L^\alpha E(x,t) \right], \tag{2.4}$$

where L is the domain length, the parameter K_α is a fractional diffusion coefficient whose dimension is $[K_\alpha] = \mathrm{m}^\alpha \mathrm{s}^{-1}$, and ${}_0D_x^\alpha$ and ${}_xD_L^\alpha$ are the left and right space-fractional Riemann-Liouville derivatives on $[0, L]$, respectively defined as follows:

$${}_0D_x^\alpha E(x,t) = \frac{1}{\Gamma(n-\alpha)} \frac{\partial^n}{\partial x^n} \int_0^x \frac{E(\xi,t)}{(x-\xi)^{\alpha-n+1}} d\xi, \tag{2.5}$$

$${}_xD_L^\alpha E(x,t) = \frac{(-1)^n}{\Gamma(n-\alpha)} \frac{\partial^n}{\partial x^n} \int_x^L \frac{E(\xi,t)}{(\xi-x)^{\alpha-n+1}} d\xi, \tag{2.6}$$

where $n = 1 + [\alpha]$ such that $[\alpha] = \max\{m \in \mathbb{Z} | m \leq \alpha\}$ and $\mathbb{Z}$ is the set of integers. Here, we get $n = 2$ as in this study $\alpha = 1.15$. Since the Riemann-Liouville derivatives are singular on the boundaries of the domain, instead, Caputo derivatives can be used. The left and right Caputo derivatives of order α, respectively are defined as follows:

$${}_0^C D_x^\alpha E(x,t) = \frac{1}{\Gamma(n-\alpha)} \int_0^x \frac{\partial^n E(\xi,t)/\partial \xi^n}{(x-\xi)^{\alpha-n+1}} d\xi, \tag{2.7}$$

$${}_x^C D_L^\alpha E(x,t) = \frac{(-1)^n}{\Gamma(n-\alpha)} \int_x^L \frac{\partial^n E(\xi,t)/\partial \xi^n}{(\xi-x)^{\alpha-n+1}} d\xi. \tag{2.8}$$

For more details on the fractional derivatives, see (Oldham and Spanier, 1974; Podlubny, 1999).
It should be noted that in addition to the power-law asymptotic behaviour of the pdf for the $CD8^+$ T cell jumps in the brain, based on the same experiments in (Harris et al., 2012), the pdf for the waiting times exhibits a power-law asymptotic behaviour as $\sim \tau^{-(\gamma+1)}$, where $\gamma = 0.7$. Here, for the sake of simplicity, we have only considered the space-fractional-order operator in our model.

2.2.2 Modelling $CD8^+$ T cells response to infection

Just as $CD8^+$ T cells cross BBBs to enter the brain, T. gondii parasites can go through such barriers by certain mechanisms (Konradt et al., 2016) and then reach the brain parenchyma. When T. gondii parasites (tachyzoites) enter the brain, they begin to infect brain cells, such as astrocytes, neurons, and microglia. The infection occurs as soon as free parasites attack brain cells and multiply inside them. Tachyzoites are then placed in a covering called parasitophorous vacuole (PV). This stage of infection is called the early stage of the T. gondii life cycle. In order to maintain their survival, tachyzoites need to enter into the second stage of their life cycle. Therefore, there is another form of T. gondii parasites, known as bradyzoites. Similar to tachyzoites, they multiply in a PV, but their growth and proliferation are slower than tachyzoites. PVs containing bradyzoites create intracellular tissue cysts over time that can be stable and persistent in the brain tissue for a long period of time (Skariah et al., 2010).

As a result of parasites entering the brain tissue, effector $CD8^+$ T cells move from lymph nodes to the brain parenchyma. They then exert two protective responses against infected brain cells through (IFN)-γ and perforin molecules. The type of such mechanisms depends on the type of T. gondii parasite. It means that in the case of infection with tachyzoites, effector $CD8^+$ T cells are able to stop the proliferation of intracellular tachyzoites through the secretion

of (IFN)-γ (Denkers, 1999). It is important to note that neurons provide favourable conditions for the creation and stability of tissue cysts in the brain tissue because neurons live longer than other brain cells, and according to in vitro studies, (IFN)-γ mechanism has little effect on the infected neurons compared to other infected brain cells (Schlüter et al., 2001). Effector CD8$^+$ T cells can also identify all bradyzoite-infected brain cells and also infected cells that carry tissue cysts of various sizes. Following the identification, CD8$^+$ T cells bind themselves to the surface of infected cells, enter the tissue cysts, and eventually, through the secretion of perforin, tissue cysts are eliminated from the brain tissue (Suzuki et al., 2010; Tiwari et al., 2019).

Based on the above biological information, to derive a mathematical model representing effector CD8$^+$ T cells response against infected cells, we shall consider the density of four cell populations at position x and time t, the susceptibles (healthy brain cells) $S(x,t)$, tachyzoite-infected brain cells $I_1(x,t)$, bradyzoite-infected brain cells $I_2(x,t)$ and effector CD8$^+$ T cells $E(x,t)$. We assume that susceptibles convert into tachyzoite-infected cells at a rate θ and that the transmission from tachyzoite- to bradyzoite-infected cells occurs at a rate β. In this model, we only consider the perforin-mediated response against infected cells. Hence, it is assumed that bradyzoite-infected cells could be killed at a rate p by effector CD8$^+$ T cells. The parameters d_1, d_2, and d_3 represent the mortality rate of infected cells with tachyzoite, infected cells with bradyzoite, and CD8$^+$ T cells, respectively. Since effector CD8$^+$ T cells present in the infected brain are recruited from lymph nodes toward the brain tissue, the model considers the function $F(x,t)$ representing the source of CD8$^+$ T cells. This model is schematically represented in Figure 2.2.

By taking the schematic representation of the model and Eq. (2.4) into account, we obtain the following model representing the density of healthy, T. gondii-infected brain cells and CD8$^+$ T cells in the brain tissue:

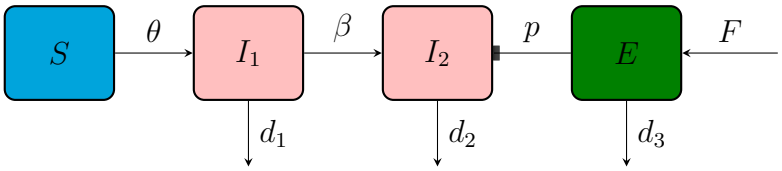

Fig. 2.2: Schematic representation of transmission from susceptibles S to infected brain cells with tachyzoite I_1 at a rate θ, tachyzoite-infected cells conversion into bradyzoite-infected brain cells I_2 at a rate β and effector CD8$^+$ T cells E response to I_2 at a rate p. The function F represents the source of effector CD8$^+$ T cells. The parameters d_1, d_2, and d_3 are the mortality rates of S, I_1 and I_2, respectively.

$$\frac{\partial S(x,t)}{\partial t} = -\theta S(x,t) I_1(x,t), \tag{2.9}$$

$$\frac{\partial I_1(x,t)}{\partial t} = \theta S(x,t) I_1(x,t) - \beta I_1(x,t) - d_1 I_1(x,t), \tag{2.10}$$

$$\frac{\partial I_2(x,t)}{\partial t} = \beta I_1(x,t) - pE(x,t) I_2(x,t) - d_2 I_2(x,t), \tag{2.11}$$

$$\frac{\partial E(x,t)}{\partial t} = K_\alpha \left[\frac{1-\beta}{2} {}_0D_x^\alpha E(x,t) + \frac{1+\beta}{2} {}_xD_L^\alpha E(x,t) \right] + F(x,t) - d_3 E(x,t). \tag{2.12}$$

If it is assumed that effector CD8$^+$ T cells perform a Brownian RW search for infected brain cells, then the model reduces to a classical model with $\alpha = 2$. Therefore, the advantage of such a model is that we can compare the results of a Lévy RW ($\alpha < 2$) with those obtained by the Brownian RW assumption

2.3 Model parametrization

In this section, we shall discuss the value of the parameters defined in Eqs. (2.9)–(2.12). Since there have been very few attempts to model T. gondii infection (Sullivan et al., 2012, 2013) and necessary

experimental data are scant, here we try to estimate the value of the model parameters from direct measurements or by considering the parameter value in other studies.

One of the problems in relation to brain infection with T. gondii is the infection rates of different brain cells from different host species. Extensive studies have been conducted on the infection rate of brain cells by free tachyzoites (see for instance (Halonen et al., 1996; Lüder et al., 1999)). When we investigate the results of the experiments, we see that there are many differences in the value of rates that are mainly due to factors, such as the type of brain cells, the brain regions where the cells come from, the host species (rat, human, and mouse), and the type of Toxoplasma parasite. For instance, the rate of infection by the first type of parasites (RH strains) is higher than the second type (ME49 and Prugniaud). Neurons of the hippocampus region of the brain from rats are infected by T. gondii at a lower rate than astrocytes, while it is more likely that cortical neurons from rats are infected. According to in vitro studies (Halonen et al., 1996; Lüder et al., 1999), if we consider a range of infection rate of 5% to 30% based on the type of brain cells, then by adding 10^5 tachyzoites to the cultures one day after infection, and assuming that each infected cell egresses 8 to 16 tachyzoites, we can estimate a range of the infection rate given by $\theta = 4 \times 10^{-6}\, day^{-1} cells^{-1}$ to $\theta = 5 \times 10^{-5}\, day^{-1} cells^{-1}$. For instance, if we consider the infection rate of 5% by 10^5 parasites and also assume that each infected cell egresses 8 tachyzoites, we can then compute $\theta = 0.05 \times 8 \times 10^{-5} = 4 \times 10^{-6}\, day^{-1} cells^{-1}$.

In order to estimate the transmission rate β and the death rates of infected cells d_1 and d_2, we refer to the experiments in (Radke et al., 2001). When free tachyzoites attack brain cells, they multiply inside infected cells by dividing. After 5 divisions, they go out of the infected cells, which leads to infecting the brain cells in their neighbourhood. Tachyzoites have a half-life of 6 hours. Thus, the estimated daily death rate of tachyzoite-infected cells is given by $d_1 = \ln 2/(5 \times 6)\,\mathrm{h}^{-1} \approx 5 \times 10^{-1}\, day^{-1}$. These tachyzoites convert into bradyzoites approximately after 20 divisions, which

results in the estimated transmission rate $\beta = 1/(20 \times 6)\,\mathrm{h}^{-1} = 2 \times 10^{-1}\,day^{-1}$. Bradyzoites have a half-life of 15 hours. If we suppose that bradyzoites go out of the infected cells after 10 divisions, the estimated daily death rate of bradyzoite-infected cells is given by $d_2 = \ln 2/(10 \times 15)\,\mathrm{h}^{-1} \approx 1 \times 10^{-1}\,day^{-1}$.

The average per capita killing rate p is the number of targets (bradyzoite-infected cells at the chronic stage) destroyed per effector CD8$^+$ T cell per day. There are very few studies discussing perforin-mediated response against bradyzoite-infected cells or tissue cysts at the chronic stage of infection (Suzuki et al., 2010; Tiwari et al., 2019). Hence, experimental data are scant. However, based on the experiments during 7 days in (Suzuki et al., 2010), if we assume that on average 50 brain cysts per day are killed by immune CD8$^+$ T cells and also that there are about 5×10^4 T cells per day, then by the definition of p, we can measure directly an average value that is given by $p = 10^{-3}\,day^{-1}cells^{-1}$. Although this value may be better estimated in future works, this estimated value is sufficient for our numerical simulations because, in this work, we aim to perform a comparison between the results of Brownian and Lévy RWs with the same conditions.

In order to obtain an approximation of diffusivity K_α, we follow the observations of Harris et al. (2012). To do so, we know that K_α has SI units of $\mathrm{m}^\alpha\mathrm{s}^{-1}$. Thus, the mean displacement length of diffusion $\mathcal{L}$ can be defined as $\mathcal{L} = (K_\alpha \mathcal{T})^{1/\alpha}$, where $\mathcal{T}$ is the corresponding time interval. Hence, based on the findings of Harris et al. (2012) on the diffusion coefficient of CD8$^+$ T cells in the T. gondii-infected brain, if we assume that $\mathcal{L} = 8\,\mu\mathrm{m}$ and $\mathcal{T} = 1\,\mathrm{min}$, the fractional diffusion coefficient can then be estimated as $K_\alpha = (8 \times 10^{-6})^\alpha/60\,\mathrm{m}^\alpha\mathrm{s}^{-1}$. It is important to note that this value could be reduced when no chemokine signals and CXCL10 are present in the infected brain. In that case, CD8$^+$ T cells nevertheless maintain the behaviour of the Lévy search pattern.

2.4 Numerical solution of space-fractional order diffusion equations

Over the past decade, in order to solve time-space fractional-order diffusion equations, analytical methods are replaced by various numerical methods due to the complexities of fractional derivatives. Most of these numerical methods are based on the finite element (FE), finite-difference (FD), and Chebyshev pseudo-spectral schemes. In this work, we have considered the same FE method used by Hanert (2010) to solve fractional-order transport models. More precisely, we have used a piecewise linear finite-element method based on a Galerkin formulation for solving Eq. (2.12). In this method, the exact solution (unknown variable) $E(x,t)$ is expressed as a sum of the unknown coefficients $e_j(t)$ and basis functions $\phi_j(x)$ as follows:

$$E(x,t) \approx \tilde{E}(x,t) = \sum_{j=1}^{N} e_j(t)\phi_j(x).$$

By introducing a partition of the domain $[0, L]$ into $N-1$ subintervals $[x_j, x_{j+1}]$ with a constant length h, i.e., $x_1 = 0, x_N = L$, and $x_{j+1} - x_j = h$ for $j = 1, \ldots, N-1$, we can consider the piecewise linear basis functions $\phi_j(x)$ for $j = 1, 2, \ldots, N$ as follows:

$$\phi_1(x) = \begin{cases} \dfrac{x_2 - x}{x_2 - x_1} & : x_1 \le x \le x_2, \\ 0 & : x \notin [x_1, x_2]. \end{cases}$$

for $j = 2, ..., N-1$,

$$\phi_j(x) = \begin{cases} \dfrac{x - x_{j-1}}{x_j - x_{j-1}} & : x_{j-1} \le x \le x_j, \\ \dfrac{x_{j+1} - x}{x_{j+1} - x_j} & : x_j \le x \le x_{j+1}, \\ 0 & : x \notin [x_{j-1}, x_{j+1}]. \end{cases}$$

and for $j = N$,

$$\phi_N(x) = \begin{cases} \dfrac{x - x_{N-1}}{x_N - x_{N-1}} & : x_{N-1} \leq x \leq x_N, \\ 0 & : x \notin [x_{N-1}, x_N]. \end{cases}$$

Now we approximate the source term $F(x,t)$ by the same discretization as the model solution as follows:

$$F(x,t) \approx \tilde{F}(x,t) = \sum_{j=1}^{N} f_j(t)\phi_j(x).$$

Since the basis functions $\phi_j(x)$ for $j = 1, 2, ..., N$ have a value of 1 at node x_j and 0 at other nodes, $f_j(t) = F(x_j, t)$. By using a Galerkin formulation, we replace $\tilde{E}(x,t)$ and $\tilde{F}(x,t)$ in the model equation and then by orthogonalizing the discrete equation with respect to all ϕ_j, we get the following equation:

$$\begin{aligned} \left(\int_0^L \phi_i\phi_j dx\right)\frac{de_j}{dt}(t) &= \left(K_\alpha \int_0^L \phi_i \frac{d^2}{dx^2} G_{\alpha\beta}(x,\phi_j)dx,\right) e_j(t) \\ &+ \left(\int_0^L \phi_i\phi_j dx\right) F(x_j,t) \\ &- d_3\left(\int_0^L \phi_i\phi_j dx\right) e_j(t), \end{aligned}$$

for $i, j = 1, ..., N$ and

$$\begin{aligned} G_{\alpha\beta}(x,\phi_j) &\equiv \frac{1-\beta}{2\Gamma(2-\alpha)}\int_0^x \frac{\phi_j(\xi)}{(x-\xi)^{\alpha-1}}d\xi \\ &+ \frac{1+\beta}{2\Gamma(2-\alpha)}\int_x^L \frac{\phi_j(\xi)}{(\xi-x)^{\alpha-1}}d\xi. \end{aligned}$$

By performing integration by parts (see Hanert (2010) for details), we get a semi-discrete equation in a matrix form as follows:

$$\mathbf{M}\frac{d\mathbf{e}}{dt}(t) = \mathbf{D}\mathbf{e}(t) + \mathbf{M}\left(\mathbf{f}(t) - d_3\mathbf{e}(t)\right), \tag{2.13}$$

where $\mathbf{e}(t) = [e_1(t) \ \dots \ e_N(t)]^T$ is the vector of unknown coefficients at time t and the elements of the vector $\mathbf{f}(t) = [F(x_1, t) \dots F(x_N, t)]^T$ are the known values of the source term at a node j at time t. The elements of the mass matrix $\mathbf{M}$ and the diffusion matrix $\mathbf{D}$ read:

$$M_{ij} = \int_0^L \phi_i \phi_j dx, \qquad D_{ij} = -K_\alpha \int_0^L \frac{d\phi_i}{dx}(x) \frac{d}{dx} G_{\alpha\beta}(x, \phi_j) dx,$$

where $\frac{d}{dx} G_{\alpha\beta}(x, \phi_j) \equiv \frac{1-\beta}{2} {}_0D_x^{\alpha-1}\phi_j(x) + \frac{1+\beta}{2} {}_xD_L^{\alpha-1}\phi_j(x)$ is a combination of the left and right Riemann-Liouville derivatives of order $\alpha - 1$ of ϕ_j. Finally, we can discretize Eq. (2.13) by using standard time integration methods. Here, a third-order Adams-Bashforth scheme has been considered. To solve Eq. (2.12), we also need to consider initial and boundary conditions.

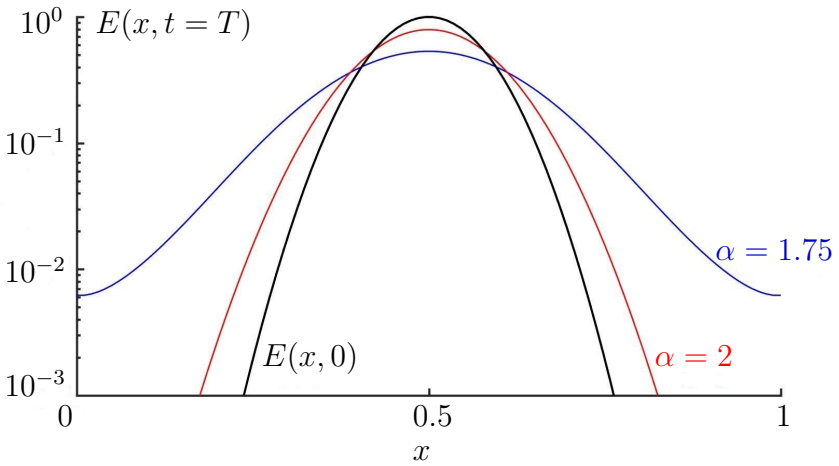

Fig. 2.3: Numerical solution of Eq. (2.12) with $F(x, t) = 0$, $d_3 = 0$ at time T for $\alpha = 2$ and $\alpha = 1.75$. Black curve shows a Gaussian function, as the initial condition. In the case of a Brownian motion ($\alpha = 2$), the solution tails decay exponentially (red curve). But, for a Lévy RW ($\alpha < 2$), the solution has a power-law asymptotic behaviour (blue curve). Here, The y-axis is in a logarithmic scale.

Here, we present an example to illustrate how different values of the parameter α affect the behaviour of the solution. We have

solved Eq. (2.12) with $F(x,t) = 0$, and $d_3 = 0$. Figure 2.3, black curve shows a Gaussian function, as the initial condition. In the case of a Brownian motion ($\alpha = 2$), the solution tails decay exponentially (Figure 2.3, red curve). But, for a Lévy RW ($\alpha < 2$), the solution has a power-law asymptotic behaviour (Figure 2.3, blue curve). Since with a Lévy RW, particles can make large displacements, as we see, the solution decays more slowly compared to the Brownian motion assumption.

2.5 Effect of Lévy RW of CD8$^+$ T cells on the infected cells

In this section, by using the model Eqs. (2.9)–(2.12) with the parameter values estimated in Section 2.3, we investigate the influence of a Lévy RW search performed by T cells on the density of infected cells in the brain. To do so, we can consider a comparison between the classical model based on the Brownian RW assumption ($\alpha = 2$) and the fractional model relying on the Lévy RW assumption ($\alpha = 1.15$).

In order to solve the proposed model, we need to define a computational domain L as a part of the brain tissue and the source function $F(x,t)$ in Eq. (2.12). The Brain tissue is composed of two kinds of tissue: grey matter and white matter. Based on the microscopic studies, tissue cysts can be formed in all regions of the brain tissue, but most of them are distributed in the cerebral cortex and hippocampus regions (Berenreiterová et al., 2011). The cerebral cortex is the outer layer of grey matter that covers the brain. Hence, we assume that the computational domain is a part of the cerebral cortex. A detailed description of the cerebral cortex is provided in (Von Economo, 2009). We define the source term by

$$F(x,t) := f(t)\delta(x - L/2),$$

where the time-dependent function $f(t)$ gives the number of CD8$^+$ T cells entering the domain in the middle per unit of time at time

t and $\delta(x - L/2)$ is the Dirac delta function centred in the middle of the domain. We define the input function $f(t)$ as a decreasing function given by $f(t) := rNe^{-rt}$, where N and r represent the number of CD8$^+$ T cells and the rate at which they enter the domain, respectively. To estimate the input rate r, we followed the observations of John et al. (2009) who studied the kinetics of CD8$^+$ T cells in the T. gondii infected brains. If we assume that the death rate of CD8$^+$ T cells is equal to $10^{-1}\,day^{-1}$ and consider a maximum number of CD8$^+$ T cells in the brain by day 14, we can then estimate the value of the input rate to be given by $r = 8 \times 10^{-2}\,day^{-1}$. Here, it is assumed that CD8$^+$ T cells enter the brain with a delay on day 3 (John et al., 2009). It should be noted that in the numerical simulations, we consider the values of N according to the estimations of Harris et al. (2012) (see supplementary information in (Harris et al., 2012)).

In order to compare the efficiency of CD8$^+$ T cells for Lévy RW versus Brownian RW, we define the average number of bradyzoite-infected cells $n(t)$ during simulation time as follows:

$$n(t) := \int_0^L I_2(x,t)dx, \tag{2.14}$$

where $I_2(x,t)$ is the density of bradyzoite-infected cells (tissue cysts) with units of the number of cells per mm. We discretize Eqs. (2.9)–(2.12) with a piecewise-linear FE method based on a Galerkin formulation. For more details on the discretization of the model equations, see Section 2.4 and appendix A.1. Eq. (2.12) needs to be solved with appropriate boundary conditions that guarantee mass conservation in the numerical simulations (see appendix A.2 for details).

In the first numerical simulation, we consider constant initial conditions $S(x,0) = 2.5 \times 10^4$ healthy brain cells and $I_1(x,0) = 150$ tachyzoite-infected cells per mm over the whole domain. We compare the average number of infected cells $n(t)$ for Lévy and Brownian RWs of CD8$^+$ T cells over the domain $[0, L]$ of the brain tissue. Here, we suppose that $L = 14\,\text{mm}$. According to our model, in-

fected cells with tachyzoites I_1 and bradyzoites I_2 will first increase in a period $[0, T_0]$ and then tend to 0 after T_0. The time evolution of the average number of infected cells $n(t)$ over the domain $[0, 14]$ with different foraging patterns of $CD8^+$ T cells is shown in Figure 2.4.

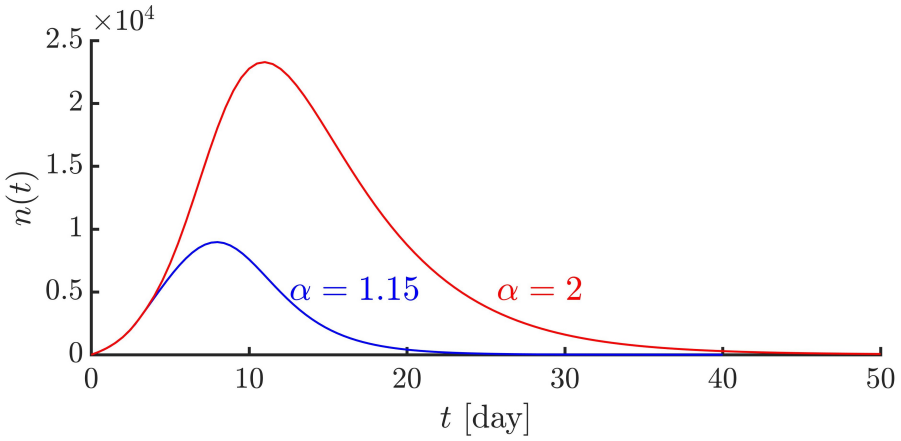

Fig. 2.4: Time evolution of the average number of infected cells $n(t)$ obtained by Eq. (2.14) over the domain $[0, 14]$ with Lévy RW ($\alpha = 1.15$) and Brownian RW ($\alpha = 2$). The average value of $n(t)$ in the period $[0, 30]$ for Lévy RW ($\bar{N}_L$) is equal to 26% of that value for Brownian RW ($\bar{N}_B$), highlighting the fact that a Lévy RW search strategy is more efficient than a Brownian motion in killing infected cells distributed in a large distance of the brain tissue.

Figure 2.4 shows that in the case of a Lévy RW, $n(t)$ reaches its maximum value at time $t = 8$ and after that tends to 0 at time $t \approx 35$. However, in the case of a Brownian motion, $n(t)$ grows quickly and reaches its maximum value at time $t = 11$ and then decreases such that $n(50) = 60$. Here, we define the average of $n(t)$ in a period $[0, T]$ by

$$\bar{N} = \int_0^T n(t)dt/T.$$

That quantity is computed for Brownian RW ($\bar{N}_B$) and Lévy RW ($\bar{N}_L$). By taking the ratio between the values of $\bar{N}_B$ and $\bar{N}_L$, we get $\bar{N}_L = 0.26\bar{N}_B$ in the period $[0, 30]$. This result shows that a Lévy foraging pattern of CD8$^+$ T cells is about four times more efficient than a Brownian motion in detecting and killing infected cells distributed throughout the brain tissue. To illustrate this result, we consider the diffusion profiles for CD8$^+$ T cells on the domain $[0, 14]$ with Lévy and Brownian RWs, which are shown in Figure 2.5 and 2.6.

Figure 2.5 and 2.6 show that the difference between Brownian and Lévy CD8$^+$ T cell density models is most obvious in the tails of T cell distribution. The Lévy RW search strategy increases the number of T cells further away from the source more than a Brownian motion and thus leads to an increase in the thickness of T cell distribution tails. However, for a Brownian motion, CD8$^+$ T cells are present more around the source, and hence they are not able to successfully eradicate infected cells located further away from the source (see Figure 2.5(a) and Figure 2.6(a)). T cells with a Lévy search strategy can travel larger distances and hence scan the entire tissue much more rapidly (see Figure 2.5(b) and Figure 2.6(b)).

The objective of CD8$^+$ T cell search is to remove all or nearly all infected cells from infected tissues. Since a Lévy RW search allows CD8$^+$ T cells to scan further distances from the source more efficiently than a Brownian motion, our results suggest that a Lévy RW search can lead to a complete detection of T. gondii-infected cells in the brain tissue. For instance, the average number of infected cells $n(t)$ over the domain $[0, 14]$ with a Lévy RW vanishes after 35 days, while with the Brownian motion assumption, $n(50) = 60$.

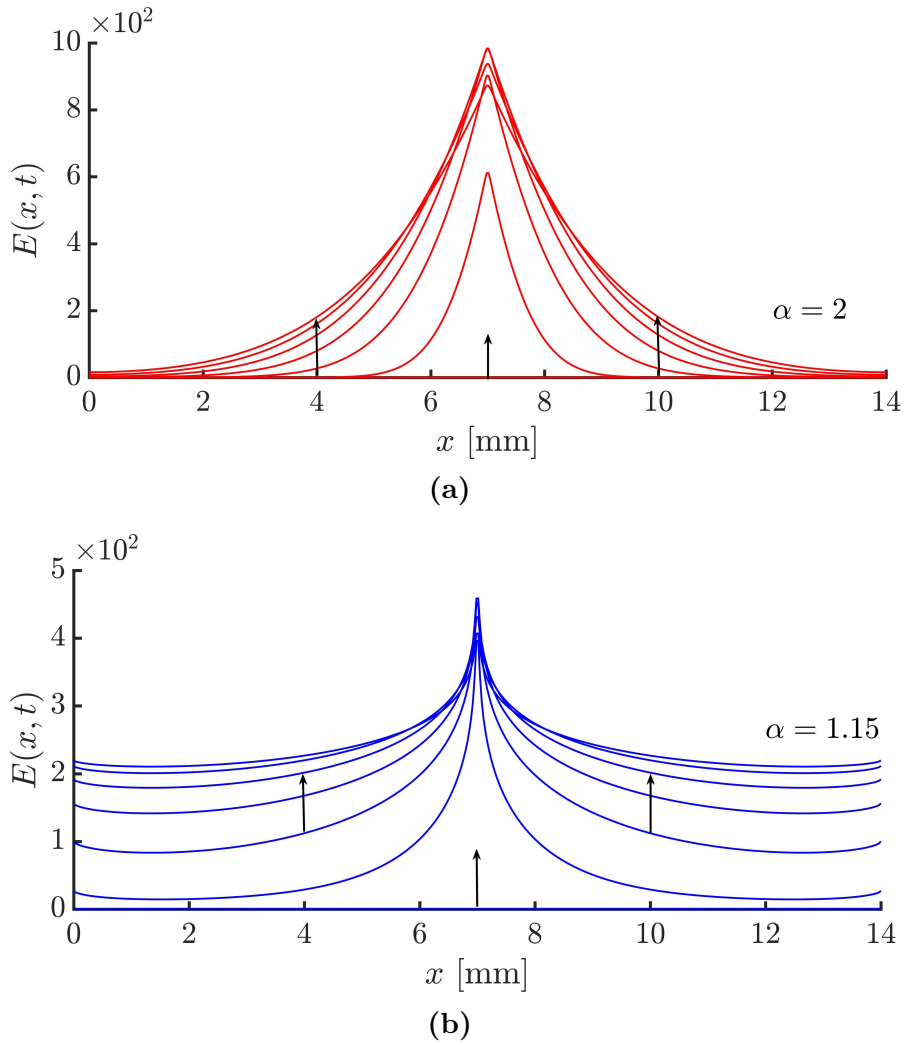

Fig. 2.5: Diffusion profiles for $CD8^+$ T cells density at different time instants on the domain $[0, 14]$ with Lévy RW ($\alpha = 1.15$) and Brownian RW ($\alpha = 2$) obtained by solving Eq. (2.12), highlighting the fact that Lévy RW assumption of T cells ($\alpha = 1.15$) increases the number of T cells further away from the source more than a Brownian motion ($\alpha = 2$). The arrows indicate the direction of diffusion of $CD8^+$ T cells starting from the zero initial condition represented on the x-axis until reaching the maximum number of T cells on day 14. Here, we assumed that $CD8^+$ T cells enter the brain with a delay on day 3. The time interval between profiles starting from day 4 is set to 2 days.

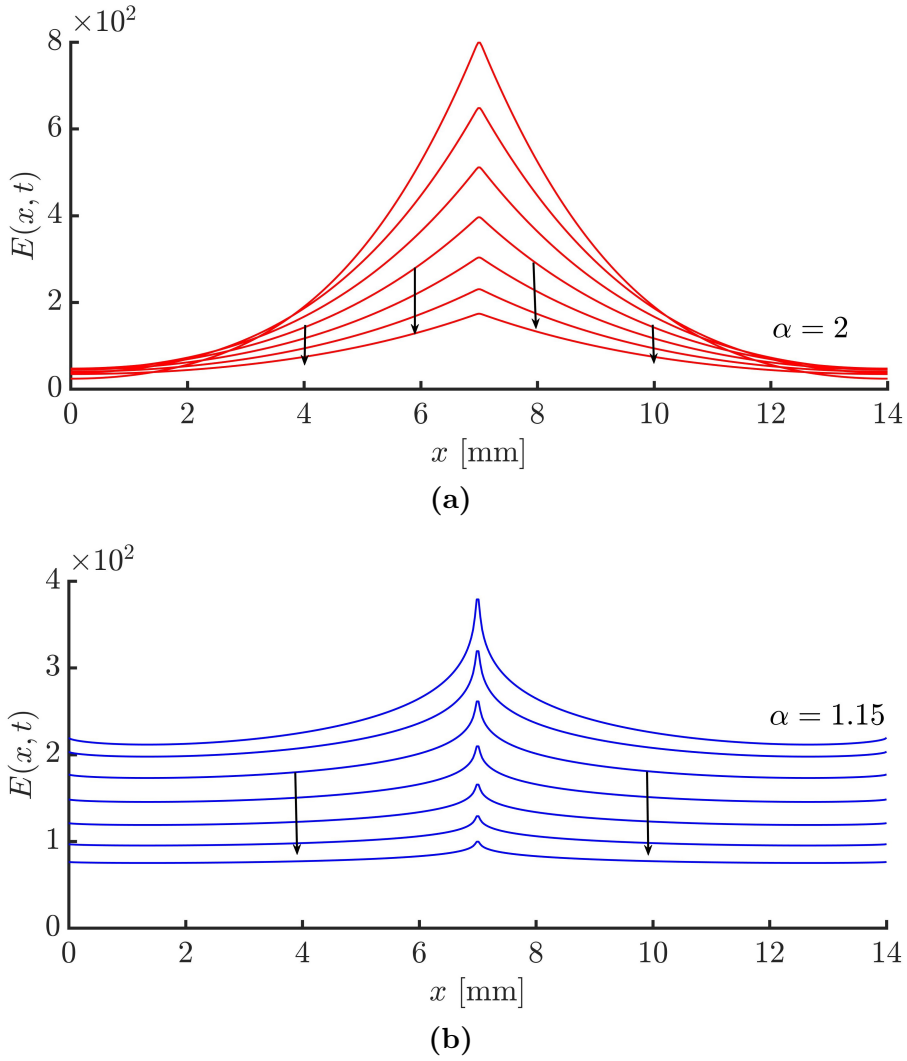

Fig. 2.6: Diffusion profiles for CD8$^+$ T cells density at different time instants on the domain $[0, 14]$ with Lévy RW ($\alpha = 1.15$) and Brownian RW ($\alpha = 2$) obtained by solving Eq. (2.12), highlighting the fact that Lévy RW assumption of T cells ($\alpha = 1.15$) increases the number of T cells further away from the source more than a Brownian motion ($\alpha = 2$). The arrows indicate the decrease in the number of T cells after day 14. The time interval between profiles starting from day 16 is set to 4 days.

We here note that from a biological point of view, when initially the infection load (burden) in the brain tissue is growing, activated $CD8^+$ T cells migrate from lymph nodes to the brain tissue to eliminate the infected brain cells. In that case, the number of immune cells throughout the tissue increases so that the infection load decreases. At this stage, the spatial propagation of $CD8^+$ T cells throughout the tissue in the case of Brownian and Lévy random walks are shown in Figure 2.5(a) and 2.5(b), respectively. Once the infection is resolved, the number of $CD8^+$ T cells declines. This is called the "contraction phase". Here, the spatial decline of T cells in the case of Brownian and Lévy random walks are compared in Figure 2.6(a) and 2.6(b), respectively, and finally, T cells could persist at a level for long periods of time in the tissue. Figure 2.4 shows the time evolution of the infection load during the immune response to the infected brain cells.

In order to highlight the efficiency of Lévy RW versus Brownian RW on the domain $[0, 14]$, we can also compute a time such that the average number of infected cells at that time is equal to 1% of the maximum value of $n(t)$ for $\alpha = 2\,(t_B)$ and $\alpha = 1.15\,(t_L)$. By taking the ratio between the values of t_B and t_L for the domain $[0, 14]$, we get $t_L = 0.58t_B$. However, that ratio for the domain $[0, 6]$ is approximately 1. Here, if we increase the length of the domain from 6 mm to 20 mm, then t_L and t_B increase from 24 to 25 days and from 24 to 50 days, respectively. In other words, the ratio t_L/t_B decreases from 1 to 0.5 (see Figure 2.7).
The numerical result shown in Figure 2.7 has been obtained by considering the time dynamics of the infection load throughout the tissue with different lengths. As the domain of infection gets larger, the average number of infected cells $n(t)$ after reaching its maximum value with a Brownian motion decreases more slowly compared to a Lévy RW search. Therefore, this result highlights the importance of a Lévy RW search pattern for accelerating the elimination of infected cells distributed broadly within the brain tissue.

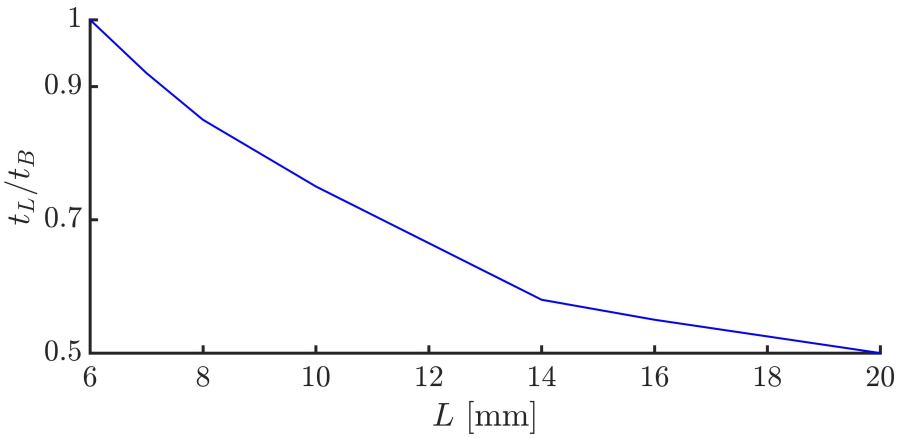

Fig. 2.7: The ratio t_L/t_B versus the length of the domain L. As L increases, the average number of infected cells reaches 1% of its maximum value rapidly with the Lévy RW compared to the Brownian motion assumption. It highlights the importance of a Lévy search pattern for accelerating the elimination of infected cells distributed broadly in the brain tissue.

The final example illustrates the differences between the elimination dynamics of infected cells with Lévy and Brownian RWs. Here, we consider the following model for the density of CD8$^+$ T cells and bradyzoite-infected cells:

$$\frac{\partial I_2(x,t)}{\partial t} = -pE(x,t)I_2(x,t), \tag{2.15}$$

$$\frac{\partial E(x,t)}{\partial t} = K_\alpha \left[\frac{1-\beta}{2}{}_0D_x^\alpha E(x,t) + \frac{1+\beta}{2}{}_xD_L^\alpha E(x,t)\right] + F(x,t) - d_3E(x,t), \tag{2.16}$$

with the initial condition $I_2(x,0) = I_0$. We suppose that an equal number of CD8$^+$ T cells per unit of time at time t enter the right-hand side of the domain $L = [0, 14]$ with a Lévy RW and the left-hand side of the domain with a Brownian motion. Here, the simulation has a duration of 5 days and $I_0 = 300$ infected cells per mm over the domain.

The elimination dynamics of the infected cells with Lévy and Brownian RWs are shown in Figure 2.8. $CD8^+$ T cells with a Lévy RW can spread across the whole domain on the right, $[7, 14]$, and hence they can rapidly destroy infected cells distributed over the entire tissue. However, $CD8^+$ T cells with a Brownian RW travel through the tissue on the left, $[0, 7]$, more slowly, leading to a slower decline of the infected cells faraway from the source. In this example, with the Lévy RW search pattern, about 90% of infected cells are killed. However, with a Brownian motion, about 36% of infected cells are eliminated from the domain $[0, 7]$.

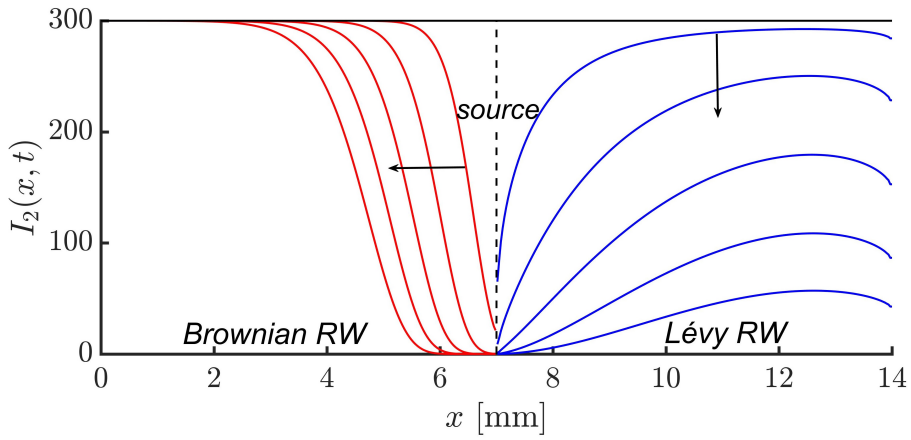

Fig. 2.8: Profiles for infected cells densities at different time instants on the domain $[0, 14]$ with Lévy RW ($\alpha = 1.15$) and Brownian RW ($\alpha = 2$) obtained by solving Eqs. (2.15) and (2.16). The equal number of $CD8^+$ T cells enter the right-hand side of the domain with a Lévy RW and the left-hand side with a Brownian RW, leading to rapid elimination of infected cells over the whole domain on the right with a Lévy RW (blue curves), and a slower decline of infected cells faraway from the source with a Brownian RW (red curves). The arrows show the direction of the model solutions over time beginning from the initial condition of infected cells displayed by a black horizontal line. Here, the simulation has a duration of 5 days and the time interval between profiles is set to 1 day.

Suzuki et al. (2010) studied the removal of tissue cysts in the brains of mice infected with T. gondii by perforin-mediated protective immunity. They transferred the immune T cells to the infected brains and then observed a significant decrease in the number of tissue cysts. They suggested that a local expansion of CD8$^+$ T cells in the brain tissue could lead to the high destruction of tissue cysts. In our model, we considered the impact of the protective mechanism of CD8$^+$ T cells by perforin on the bradyzoite-infected cells. Our results suggest that the Lévy RW search enables T cells to accelerate the elimination of tissue cysts. Thus, we predict that in addition to possible reasons for high reduction of cysts, such as a local proliferation of CD8$^+$ T cells, the Lévy RW search strategy performed by CD8$^+$ T cells can be a possible factor for marked decreases in tissue cyst numbers in the T. gondii-infected brain.

2.6 Conclusion

In their search for targets, many species in almost any biological environment do random searches when their intellectual capacities are constrained by the distribution of their targets. For instance, T cells can perform different search patterns for their targets across different tissues. Mathematical models are useful tools to study how the search strategies performed by T cells can lead to an efficient immune response against pathogens. Among all foraging patterns in tissues, random motion of CD8$^+$ T cells in the T. gondii-infected brain is considerable due to a switch in the random search strategy of T cells from a Brownian motion observed in other tissues to a Lévy RW search in the brain tissue. Hence, studying the effective role of a Lévy RW search indeed requires specific tools. One of them is to use fractional diffusion equations to obtain the density of T cells in the infected brain.

In this work, we have derived a space fractional-order equation consisting of fractional-order diffusion and reaction terms to get the density of T cells in the infected brain. The fractional diffusion

with order $\alpha < 2$ represents a complex dispersion of T cells called superdiffusion, and the reaction terms describe the recruitment of T cells from lymph nodes into the brain and their natural death. When $\alpha = 2$, the resulting equation represents the Brownian motion. Hence, we were able to perform a comparison between the results of Lévy and Brownian RWs. Based on the T. gondii life cycle in the brain, we have also derived space-time reaction equations representing the density of tachyzoite- and bradyzoite-infected cells in the brain tissue. This allowed us to study the effect of the Lévy RW search of $CD8^+$ T cells on the bradyzoite-infected cell (tissue cysts) density by the perforin-mediated immune response. Our simulation results have shown that the average number of infected cells ($\bar{N}$) in the period $[0, 30]$ with a Lévy RW on the domain $[0, 14]$ is 26% of $\bar{N}$ with the Brownian motion. This means that $CD8^+$ T cells with a Lévy RW search are more successful than a Brownian motion in response to infection because T cells can travel faraway from the source, leading to more eradication of the cysts in the brain. Furthermore, as T. gondii parasites are capable of infecting large areas of the brain tissue, a Lévy RW search allows $CD8^+$ T cells to scan large distances, which results in a complete detection of infected cells and hence all or nearly all infected cells are eliminated from the brain tissue. However, with the Brownian motion assumption, infected cells located further away from the source could be out of reach of $CD8^+$ T cells.

We here note that Harris et al. (2012) have also shown the efficiency of effector $CD8^+$ T cells for Lévy RW versus Brownian RW. In their model, the efficiency has been defined based on the sum of T cells displacements at the moment when the first T cell reaches a target at the origin of a sphere. They showed that in the case of a Lévy RW, the sum of the displacements to reach a target is less than a Brownian motion, and hence a Lévy RW search is more efficient. However, our model provides a much more realistic picture of the efficient role of the Lévy search strategy on the protective mechanism of $CD8^+$ T cells.

It is noteworthy to point out that the model could be further

improved by considering some issues that have been ignored. One of them is the effect of the anti-parasitic mechanism of effector CD8$^+$ T cells by IFN-γ on controlling the rapid division of tachyzoites. In (Wodarz et al., 2002), the two protective mechanisms of CD8$^+$ T cells by perforin and IFN-γ are referred to as the lytic and nonlytic responses of the immune system against pathogens, respectively. This model may therefore be improved by considering both the lytic and non-lytic immune responses using the same approach that Wodarz et al. (2002) applied to develop viral infection models.

Another issue is the study of non-Markovian property in anomalous dispersions. According to observations of Harris et al. (2012), when CD8$^+$ T cells make a displacement, the probability distribution function for the waiting or pausing times exhibits a power-law asymptotic behaviour as $\sim \tau^{-(\gamma+1)}$ with $\gamma = 0.7$. In that case, the anomalous diffusion of CD8$^+$ T cells has a non-Markovian effect. By considering a large number of CD8$^+$ T cells, for the T cell density in the brain, a time fractional-order diffusion equation with order $0 < \gamma < 1$ is obtained. However, for a Brownian motion, the time derivative order is equal to 1 and the diffusion has a Markovian property. For solving space-time fractional-order equations, there are some efficient numerical methods based on Chebyshev pseudospectral method. For instance, see (Hanert, 2011; Hanert and Piret, 2014).

CHAPTER 3

Front propagation of exponentially truncated fractional-order epidemics

This chapter reproduces the following article[1]:

A. Farhadi, E. Hanert, Front Propagation of Exponentially Truncated Fractional-Order Epidemics, *Fractal and Fractional*, 2022, doi: 10.3390/fractalfract6020053

Abstract

The existence of landscape constraints in the home range of living organisms that adopt Lévy-flight movement patterns, prevents them from making arbitrarily large displacements. Their random movements indeed occur in a finite

[1]Only minor modifications were made.

space with an upper bound. In order to make realistic models, by introducing exponentially truncated Lévy flights, such an upper bound can thus be taken into account in the reaction-diffusion models. In this work, we have investigated the influence of the λ-truncated fractional-order diffusion operator on the spatial propagation of the epidemics caused by infectious diseases, where λ is the truncation parameter. Analytical and numerical simulations show that depending on the value of λ, different asymptotic behaviours of the travelling-wave solutions can be identified. For small values of λ ($\lambda \gtrsim 0$), the tails of the infective waves can decay algebraically leading to an exponential growth of the epidemic speed. In that case, the truncation has no impact on the superdiffusive epidemics. By increasing the value of λ, the algebraic decaying tails can be tamed leading to either an upper bound on the epidemic speed representing the maximum speed value or the generation of the infective waves of a constant shape propagating at a minimum constant speed as observed in the classical models (second-order diffusion epidemic models). Our findings suggest that the truncated fractional-order diffusion equations have the potential to model the epidemics of animals performing Lévy flights, as the animal diseases can spread more smoothly than the exponential acceleration of the human disease epidemics.

3.1 Introduction

Infectious pathogens, such as viruses are the microorganisms that can cause infectious diseases following their presence and growth in humans and animals (hosts) (Cleaveland et al., 2001). One of the characteristics of infectious diseases is the ability of pathogens to be transmitted between individuals by either close contact between infected and non-infected (susceptible) individuals or a secondary host that carries the pathogens. Infectious diseases are thus also called communicable or transmissible diseases. Influenza,

novel coronavirus (COVID-19), malaria, dengue fever, and West Nile virus are examples of infectious diseases. The propagation of infectious pathogens into non-infected regions leads to the spatial expansion of transmissible diseases and as a result, a large number of susceptible individuals can be infected so that an epidemic occurs. In some cases, a human epidemic can propagate over the entire globe, which is known as a pandemic. The 1918 Spanish influenza and COVID-19 are examples of classic and novel pandemics, respectively, (Nelson and Williams, 2014; Ciotti et al., 2020).

In epidemiology, mathematical models have been widely used to study the temporal and spatial dynamics of infectious diseases. Assuming the spatial homogeneity of the environment leads to the models that encompass the temporal dynamics of infectious diseases (Brauer, 2008; Cruz-Pacheco et al., 2005; Esteva and Vargas, 1998; Chen et al., 2020). These models vary based on the characteristics of the particular disease, such as the transmission mechanism by either close contact or secondary hosts (see (Keeling and Rohani, 2011) for an extensive review of various mathematical models of animal and human infectious diseases). One of the purposes of such models is to derive the basic reproductive number that indicates the potential for the propagation of infectious diseases within a population. When its value is greater than unity, it shows that the infection is capable of invading the susceptible population, leading to the occurrence of an epidemic. Since this number is dependent on the model parameters, some strategies can be taken into account to control the propagation of the epidemics (Van den Driessche and Watmough, 2008; Bowman et al., 2005). However, considering the random mobility of hosts and also the spatial heterogeneity of the environment lead to the reaction-diffusion models that describe the spatial dynamics of infectious diseases (Wu, 2008; Maidana and Yang, 2009, 2008). As an original model of this type, Källén et al. (Källén et al., 1985) studied the spatial spread of rabies among foxes. The main advantage of the reaction-diffusion epidemic models is to understand how fast an infectious disease can propagate. In that case, in order to control the spatial spread of the diseases,

the parameters that govern the epidemic speed can be distinguished (Murray, 2001).

The type of host random mobility is a key factor that affects the epidemic speed and the patterns of the epidemic spread. Brownian motion and Lévy flight are two different patterns of random movements. Brownian motion is a normal dispersion process in which particles (walkers) make short movements such that the probability distribution function (pdf) of the displacement is obtained by the normal (Gaussian) distribution (Okubo and Levin, 2001). Considering Brownian motion pattern of susceptible and infective individuals leads to a second-order reaction-diffusion epidemic model. In that case, the epidemic waves propagate at a constant speed and the tails of the epidemic's fronts decay exponentially. Such classical models have been applied to estimate the propagation speed of the plague in the 14th century and rabies in Europe (Murray, 2001; Shigesada and Kawasaki, 1997). However, Lévy-flight mobility pattern represents an anomalous diffusion process in which the walkers make occasionally large jumps between many short movements such that the pdf of the displacement is obtained by a power-law distribution with an asymptotic behaviour as $l^{-(\alpha+1)}$, where l is the length of the displacement and $0 < \alpha < 2$ (Metzler and Klafter, 2000). Different studies have shown that the random movement of many living organisms can be described by Lévy flights, including large marine predators (Sims et al., 2008; Humphries et al., 2010), fruit flies (Reynolds and Frye, 2007), bumblebees (Lihoreau et al., 2016), honeybees (Reynolds et al., 2007a,b), albatrosses (Humphries et al., 2013) and even humans (Brockmann et al., 2006). Considering a population of the walkers performing a Lévy-flight mobility pattern leads to a fractional-order reaction-diffusion equation whose solution represents the walker densities (Metzler and Klafter, 2000; Chaves, 1998). From an applied point of view, fractional-order models have been used in a broad range of problems in ecology (Hanert, 2012; Vallaeys et al., 2017), biology (Raghib et al., 2010), plasma turbulence (del Castillo-Negrete et al., 2004, 2005), finance (Cartea and del

Castillo-Negrete, 2007b) and also recently numerous studies have been conducted on the subjects of bifurcation analysis, stability, and optimal control of fractional-order systems, such as predator-prey models (Yuan et al., 2021; Huang et al., 2020), neural networks (Xu et al., 2021a; Huang et al., 2019; Xu et al., 2021b), and diffusive mussel-algae models (Djilali et al., 2020). As an application of space fractional-order diffusion equations in epidemiology, Hanert et al. (2011) have shown that such equations can be applied to model the modern epidemics, such as avian influenza, and even SARS and also that the fractional-order diffusion operators make the epidemic waves travel at an exponential speed and the tails of the wave solutions decay algebraically as a power-law.

The existence of landscape and physiological constraints in the home range of living organisms following a pure Lévy-flight mobility pattern, can prevent arbitrarily large movements. To make realistic displacements, the tails of the power-law distribution must be truncated. In that case, the pure Lévy distribution is replaced by a truncated power-law distribution whose tail decays more quickly than it does in the pure Lévy case. Mantegna and Stanley (1994) and Koponen (1995) originally introduced truncated Lévy processes and after that Rosiński (2007) proposed an exponentially truncated (tempered) Lévy process that yields a smoother decay than the abrupt cutoff. The pure power-law distributions result in diverging measurable quantities, such as variance and moments that cannot be observed in physically realizable systems. However, the truncated Lévy flight leads to the finite moments. The exponentially tempered Lévy distribution exhibits an asymptotic behaviour as $\sim e^{-\lambda l} l^{-(\alpha+1)}$, where l is the length of the displacement, $0 < \alpha < 2$, and $\lambda > 0$ is the truncation parameter. When $\lambda = 0$, it leads to a pure Lévy flight distribution. Considering a large number of random walkers performing a truncated Lévy flight leads to a truncated fractional-order diffusion equation whose solution represents the walker densities (Cartea and del Castillo-Negrete, 2007a; Baeumer and Meerschaert, 2010). As an application of such equations, Vallaeys et al. (2017) estimated isolation distances between

genetically modified (GM) and non-GM crops by considering the fact that the honeybees mobility pattern can be well described by truncated Lévy flights. del Castillo-Negrete (2009) examined the influence of the truncation on the travelling-wave solutions of a truncated fractional-order Fisher–Kolmogorov equation. It would be of interest to investigate the results of such an equation in the epidemic models, as modern epidemics do not follow Brownian dynamics and can lead to accelerated waves of infectious diseases (Small et al., 2007; Mundt et al., 2009). Hence, in this study, we apply the random mobility of infective individuals following truncated Lévy flights to an epidemic model and explore the epidemic speed based on the different values of the truncation parameter.

The remainder of the paper is organized as follows. In Section 3.2, we introduce the space fractional-order operators. In Section 3.3, we first review the classical and untruncated fractional-order epidemic models, then formulate a truncated fractional-order epidemic model and finally, discuss the epidemic speed of the new model. In Section 3.4, we explore our analytical results by numerically solving the model and conclusion is given in Section 3.5.

3.2 Preliminaries for fractional-order operators

In this section, we shall give some definitions and notations that are required for this work. In the field of fractional models, the classical operators in time and/or space are replaced by the fractional derivative operators that are defined as follows.

For a given function f, the untruncated space fractional-order derivative operator of order α with a shorthand notation $\mathcal{D}_x^\alpha$ or $d^\alpha/d|x|^\alpha$ is defined as (Cartea and del Castillo-Negrete, 2007a):

$$\mathcal{D}_x^\alpha f(x) = l\, {}_{-\infty}D_x^\alpha f(x) + r\, {}_xD_\infty^\alpha f(x), \tag{3.1}$$

where ${}_{-\infty}D_x^\alpha$ and ${}_xD_\infty^\alpha$ are the positive (left) and negative (right) space-fractional Riemann–Liouville derivatives, respectively, defined

as (Kilbas et al., 1993; Podlubny, 1998):

$$ {}_{-\infty}D_x^{\alpha} f(x) = \frac{1}{\Gamma(n-\alpha)} \frac{\partial^n}{\partial x^n} \int_{-\infty}^{x} \frac{f(\xi)}{(x-\xi)^{\alpha-n+1}} d\xi, \tag{3.2} $$

$$ {}_{x}D_{\infty}^{\alpha} f(x) = \frac{(-1)^n}{\Gamma(n-\alpha)} \frac{\partial^n}{\partial x^n} \int_{x}^{\infty} \frac{f(\xi)}{(\xi-x)^{\alpha-n+1}} d\xi, \tag{3.3} $$

where $\Gamma(.)$ denotes Euler's gamma function and $n = 1 + [\alpha]$ such that $[\alpha] = \max\{m \in \mathbb{Z} | m \leq \alpha\}$ and $\mathbb{Z}$ is the set of integers. For instance, for $1 < \alpha \leq 2$, we get $n = 2$, and the parameters l and r are the weighting factors defined as:

$$ l = -\frac{1-\beta}{2\cos(\alpha\pi/2)}, \qquad r = -\frac{1+\beta}{2\cos(\alpha\pi/2)}, \tag{3.4} $$

where the parameter $\beta \in [-1, 1]$ is a skewness parameter that shows a preferred direction of displacements that can be seen in heterogeneous systems. When $\beta = 0$, the distribution is symmetric and space derivative represents a symmetric Riesz derivative.

Since the Riemann–Liouville derivatives are singular on the boundaries of a bounded domain $[0, L]$, where $L > 0$, instead, Caputo derivatives can be used. The left and right Caputo derivatives of order α are defined as follow (Kilbas et al., 1993; Podlubny, 1998):

$$ {}_{0}^{C}D_x^{\alpha} f(x) = \frac{1}{\Gamma(n-\alpha)} \int_{0}^{x} \frac{\partial^n f(\xi)/\partial\xi^n}{(x-\xi)^{\alpha-n+1}} d\xi, \tag{3.5} $$

$$ {}_{x}^{C}D_L^{\alpha} f(x) = \frac{(-1)^n}{\Gamma(n-\alpha)} \int_{x}^{L} \frac{\partial^n f(\xi)/\partial\xi^n}{(\xi-x)^{\alpha-n+1}} d\xi. \tag{3.6} $$

The $\lambda-$truncated (tempered) fractional-order derivative operator of order α with a shorthand notation $\mathcal{D}_x^{\alpha,\lambda}$ is defined as (Cartea and del Castillo-Negrete, 2007a).

For $0 < \alpha < 1$,

$$ \begin{aligned} \mathcal{D}_x^{\alpha,\lambda} f(x) &= l e^{-\lambda x} {}_{-\infty}D_x^{\alpha}(e^{\lambda x} f(x)) + r e^{\lambda x} {}_{x}D_{\infty}^{\alpha}(e^{-\lambda x} f(x)) \\ &+ \frac{\lambda^{\alpha}}{\cos(\alpha\pi/2)} f(x), \end{aligned} \tag{3.7} $$

For $1 < \alpha < 2$,

$$\begin{aligned} \mathcal{D}_x^{\alpha,\lambda} f(x) &= l e^{-\lambda x}\, {}_{-\infty}D_x^{\alpha}(e^{\lambda x} f(x)) + r e^{\lambda x}\, {}_{x}D_{\infty}^{\alpha}(e^{-\lambda x} f(x)) \\ &+ \frac{\lambda^{\alpha}}{\cos(\alpha\pi/2)} f(x) + \frac{\alpha\beta\lambda^{\alpha-1}}{|\cos(\alpha\pi/2)|}\frac{\partial f}{\partial x}, \end{aligned} \tag{3.8}$$

where the operators ${}_{-\infty}D_x^{\alpha}$ and ${}_{x}D_{\infty}^{\alpha}$ and the parameters l and r are defined by Eqs. (3.2)–(3.4), respectively, and $\lambda \geq 0$ is a truncation parameter with SI units m^{-1}. Now, for $1 < \alpha < 2$, we can define the left and right-sided truncated fractional-order operators ${}_{-\infty}\mathcal{D}_x^{\alpha,\lambda}$ and ${}_{x}\mathcal{D}_{\infty}^{\alpha,\lambda}$, for $\beta = -1$ and $\beta = 1$, respectively, as follows:

$$\begin{aligned} {}_{-\infty}\mathcal{D}_x^{\alpha,\lambda} f(x) = \frac{-1}{\cos(\alpha\pi/2)}\Bigg(& e^{-\lambda x}\, {}_{-\infty}D_x^{\alpha}(e^{\lambda x} f(x)) \\ & - \lambda^{\alpha} f(x) - \alpha\lambda^{\alpha-1}\frac{\partial f}{\partial x}\Bigg). \end{aligned} \tag{3.9}$$

$${}_{x}\mathcal{D}_{\infty}^{\alpha,\lambda} f(x) = \frac{-1}{\cos(\alpha\pi/2)}\left(e^{\lambda x}\, {}_{x}D_{\infty}^{\alpha}(e^{-\lambda x} f(x)) - \lambda^{\alpha} f(x) + \alpha\lambda^{\alpha-1}\frac{\partial f}{\partial x}\right). \tag{3.10}$$

3.3 Spatial propagation of an epidemic

In this section, we investigate the effect of different random movements of individuals on the spatial spread and speed of an epidemic. To do so, we consider a simple version of the epidemic models. The model takes into account the densities of two populations at location x at time t, the susceptibles $S(x,t)$ and the infectives $I(x,t)$. We assume that the susceptibles catch the disease from the infectives at a constant transmission-efficiency rate δ and that the infectives disappear either by recovery from the disease or disease-induced mortality, at a constant rate γ. We model the random movement of susceptibles and infectives by considering

diffusion operators in the model equations. With these assumptions, the densities of susceptiples and infectives vary according to the following equations:

$$\frac{\partial S}{\partial t} = -\delta S(x,t)I(x,t) + \underbrace{\text{diffusion operator}}_{\text{random motion}}, \tag{3.11}$$

$$\frac{\partial I}{\partial t} = \delta S(x,t)I(x,t) - \gamma I(x,t) + \underbrace{\text{diffusion operator}}_{\text{random motion}}. \tag{3.12}$$

In what follows, we shall formulate "diffusion operator" by considering three patterns of random mobility of individuals, namely Brownian motion, pure (untruncated) Lévy flight and truncated Lévy flight, and then discuss the epidemic speed in each case.

3.3.1 Brownian Motion

Brownian motion is a normal dispersion process that the probability distribution function (pdf) for the displacements is a Gaussian (Normal) distribution. In that case, if we assume that the mobility of susceptible and infective individuals is described by Brownian motion, the diffusion operators in Eqs. (3.11) and (3.12) are the second-order diffusion denoted $K\partial^2 S(x,t)/\partial x^2$ and $K\partial^2 I(x,t)/\partial x^2$, respectively, where K represents the diffusion coefficient and has units of $\mathrm{m^2 s^{-1}}$. Therefore, we get

$$\frac{\partial S}{\partial t} = -\delta S(x,t)I(x,t) + K\frac{\partial^2 S(x,t)}{\partial x^2}, \tag{3.13}$$

$$\frac{\partial I}{\partial t} = \delta S(x,t)I(x,t) - \gamma I(x,t) + K\frac{\partial^2 I(x,t)}{\partial x^2}, \tag{3.14}$$

To obtain the epidemic speed, we consider a situation in which the wave of infectives propagates into the susceptible population whose density is uniformly set to be $S(x,0) = S_0$ throughout the entire domain. In that case, the constant epidemic speed at the leading edge, i.e., where $S \approx S_0$ and $I \approx 0$ is given by $c = 2\sqrt{K(\delta S_0 - \gamma)}$ for $K(\delta S_0 - \gamma) > 0$. For more details, refer to (Murray, 2001; Shigesada and Kawasaki, 1997).

3.3.2 Pure (Untruncated) Lévy flights

For pure Lévy flights, the power-law asymptotic behaviour of the pdf for the displacements leads to the space fractional-order diffusion operator $\mathcal{D}_x^\alpha$ defined by Eq. (3.1). If we assume that the susceptible and infective populations perform Lévy flights, the fractional-order epidemic model reads

$$\frac{\partial S}{\partial t} = -\delta S(x,t)I(x,t) + K_\alpha \mathcal{D}_x^\alpha, \tag{3.15}$$

$$\frac{\partial I}{\partial t} = \delta S(x,t)I(x,t) - \gamma I(x,t) + K_\alpha \mathcal{D}_x^\alpha, \tag{3.16}$$

where K_α is the fractional-order diffusivity with units of $\mathrm{m}^\alpha \mathrm{s}^{-1}$. Hanert et al. (2011) investigated the effect of the left-sided fractional diffusion operator on the left-and right-moving fronts. It was shown that the epidemic waves travel to the right side at an unbounded and exponential speed given by $c(t) \sim (1-\lambda)e^{((1-\lambda)/(\alpha+1))t}$ for large values of t and to the left side at a constant speed given by $c = \alpha((1-\lambda)/(\alpha-1))^{(\alpha-1)/\alpha}$, where $\lambda = \gamma/\delta S_0$. It should be noted that in the case of the symmetric fractional operator ($\beta = 0$), the infective waves propagating to the left and right sides have the same speed, i.e., both the left- and right-moving waves accelerate exponentially.

3.3.3 Truncated Lévy flights

In this subsection, we investigate the effect of the truncated Lévy flights on the epidemic speed. To do so, we consider the left-sided truncated fractional-order diffusion operator ${}_{-\infty}\mathcal{D}_x^{\alpha,\lambda}$ defined by Eq. (3.9). Since the movement of susceptible individuals does not change the front speed, for the sake of simplicity, we suppose that there is no diffusion term in the S equation. However, infectious individuals move into the susceptible population. The model

equations then read as follows:

$$\frac{\partial S(x,t)}{\partial t} = -\delta S(x,t)I(x,t), \tag{3.17}$$

$$\frac{\partial I(x,t)}{\partial t} = \delta S(x,t)I(x,t) - \gamma I(x,t) + D_\alpha \left(e^{-\lambda x}\, {}_{-\infty}D_x^\alpha (e^{\lambda x} I(x,t)) - \lambda^\alpha I(x,t)\right), \tag{3.18}$$

where $D_\alpha = K_\alpha / |\cos(\alpha\pi/2)|$. It should be noted that similar to the assumption used by del Castillo-Negrete (2009) for the truncated fractional-order Fisher–Kolmogorov equation, we do not consider the term $\partial I(x,t)/\partial x$ in the I equation. In order to analyse the solutions of Eqs. (3.17) and (3.18), we first make them dimensionless by introducing the following variables:

$$\bar{S} = \frac{S}{S_0}, \quad \bar{I} = \frac{I}{S_0}, \quad \bar{x} = \frac{x}{x_c}, \quad \bar{t} = \frac{t}{t_c},$$

where x_c and t_c are characteristic values of x and t, respectively. In what follows, we estimate these values. The next task is to insert the new dimensionless variables into Eqs. (3.17) and (3.18). That is, we replace S by $S_0\bar{S}$, I by $S_0\bar{I}$, t by $t_c\bar{t}$ and x by $x_c\bar{x}$. The derivative with respect to $\bar{t}$ is derived through the chain rule as

$$\frac{\partial I}{\partial t} = \frac{\partial (S_0\bar{I})}{\partial \bar{t}}\frac{d\bar{t}}{dt} = S_0 \frac{\partial \bar{I}}{\partial \bar{t}}\frac{1}{t_c} = \frac{S_0}{t_c}\frac{\partial \bar{I}}{\partial \bar{t}}, \qquad \frac{\partial S}{\partial t} = \frac{S_0}{t_c}\frac{\partial \bar{S}}{\partial \bar{t}},$$

and the left fractional-order derivative with respect to $\bar{x}$, ${}_{-\infty}D_{\bar{x}}^\alpha$ is also derived as follows:

$${}_{-\infty}D_x^\alpha (e^{\lambda x} I) = S_0\, {}_{-\infty}D_{\bar{x}}^\alpha (e^{\lambda x_c \bar{x}}\bar{I})\left(\frac{d\bar{x}}{dx}\right)^\alpha = \frac{S_0}{x_c^\alpha}\, {}_{-\infty}D_{\bar{x}}^\alpha (e^{\lambda x_c \bar{x}}\bar{I}).$$

Therefore, Eqs. (3.17) and (3.18) now become

$$\frac{S_0}{t_c}\frac{\partial \bar{S}}{\partial \bar{t}} = -\delta S_0^2 \bar{S}\bar{I},$$

$$\frac{S_0}{t_c}\frac{\partial \bar{I}}{\partial \bar{t}} = \delta S_0^2 \bar{S}\bar{I} - \gamma S_0 \bar{I} + \frac{D_\alpha S_0}{x_c^\alpha} e^{-\lambda x_c \bar{x}}\, {}_{-\infty}D_{\bar{x}}^\alpha (e^{\lambda x_c \bar{x}}\bar{I}) - D_\alpha \lambda^\alpha S_0 \bar{I},$$

By choosing $t_c = \dfrac{1}{\delta S_0}$ and $x_c = \left(\dfrac{D_\alpha}{\delta S_0}\right)^{1/\alpha}$, we get the following model in a dimensionless form:

$$\begin{aligned} \frac{\partial S(x,t)}{\partial t} &= -S(x,t)I(x,t), && (3.19)\\ \frac{\partial I(x,t)}{\partial t} &= S(x,t)I(x,t) - \theta I(x,t) \\ &+ e^{-\mu x}\,{}_{-\infty}D_x^{\alpha}(e^{\mu x}I(x,t)), && (3.20) \end{aligned}$$

where we have dropped the overbar "$-$", $\theta = \dfrac{\gamma + D_\alpha \lambda^\alpha}{\delta S_0}$, and $\mu = \lambda\left(\dfrac{D_\alpha}{\delta S_0}\right)^{1/\alpha}$ are dimensionless parameters.

3.3.3.1 Theoretical analysis (right-propagating front)

Here, we look for the speed of the infective waves propagating to the right side. Similar to the theoretical analysis of the model studied in (Hanert et al., 2011), we replace $S(x,t)$ by $1 - s(x,t)$, where $s(x,t)$ is the deviation with respect to the initial density of the susceptible population. Since the epidemic speed can be obtained by the speed of the right-moving fronts in the leading edge region, i.e, where $s \approx 0$ and $I \approx 0$, Eqs. (3.19) and (3.20) in that region can be expressed as

$$\begin{aligned} \frac{\partial s(x,t)}{\partial t} &= I(x,t), && (3.21)\\ \frac{\partial I(x,t)}{\partial t} &= (1-\theta)I(x,t) + e^{-\mu x}\,{}_{-\infty}D_x^{\alpha}(e^{\mu x}I(x,t)). && (3.22) \end{aligned}$$

Here, we assume that $1 - \theta > 0$, which guarantees the existence of the right-moving fronts.

Now, we find the analytical solution of Eq. (3.22), by defining the following localized initial condition:

$$I(x, t=0) = \begin{cases} A & \text{if } x < 0 \\ Ae^{-\nu x} & \text{if } x \geq 0, \end{cases} \qquad (3.23)$$

where A and ν are positive and non-zero constants. We next follow the same method as the one used by del Castillo-Negrete (2009) for the truncated fractional-order Fisher–Kolmogorov equation. First, we assume a solution of Eq. (3.22) in the form of $I(x,t) = e^{-\mu x+(1-\theta)t}\Phi(x,t)$. By substituting this solution into (3.22) and initial condition (3.23), one gets the following fractional-order diffusion equation

$$\frac{\partial \Phi(x,t)}{\partial t} =_{-\infty} D_x^{\alpha}\Phi(x,t), \tag{3.24}$$

with the initial condition

$$\Phi_0(x) = \Phi(x,t=0) = \begin{cases} Ae^{\mu x} & \text{if } x < 0 \\ Ae^{(\mu-\nu)x} & \text{if } x \geq 0. \end{cases} \tag{3.25}$$

Eq. (3.24) with initial condition (3.25) has the general solution of the form

$$\Phi(x,t) = \int_{-\infty}^{\infty} G(x-y,t)\Phi_0(y)dy, \tag{3.26}$$

where $G(x,t) = t^{-1/\alpha}p_\alpha(x/t^{1/\alpha})$ is the Green function of Eq. (3.24) and $p_\alpha(\eta) = (1/2\pi)\int_{-\infty}^{\infty} e^{(ik)^\alpha + ik\eta}dk$ is a skewed Lévy distribution with exponent α. By substituting initial condition (3.25) into Eq. (3.26), we get

$$\begin{aligned} \Phi(x,t) &= \int_{-\infty}^{xt^{-1/\alpha}} Ae^{(\mu-\nu)(x-t^{1/\alpha}\eta)}p_\alpha(\eta)d\eta \\ &+ \int_{xt^{-1/\alpha}}^{\infty} Ae^{\mu(x-t^{1/\alpha}\eta)}p_\alpha(\eta)d\eta \\ &= Ae^{(\mu-\nu)x}\int_{-\infty}^{x/\tau} e^{(\nu-\mu)\tau\eta}p_\alpha(\eta)d\eta \\ &+ Ae^{\mu x}\int_{x/\tau}^{\infty} e^{-\mu\tau\eta}p_\alpha(\eta)d\eta, \end{aligned} \tag{3.27}$$

where $\tau = t^{1/\alpha}$. Now, one can find the solution of Eq. (3.22) in the following form

$$I(x,t) = Ae^{-\nu x+(1-\theta)t}I_1 + Ae^{(1-\theta)t}I_2, \tag{3.28}$$

where $I_1 = \int_{-\infty}^{x/\tau} e^{(\nu-\mu)\tau\eta} p_\alpha(\eta) d\eta$ and $I_2 = \int_{x/\tau}^{\infty} e^{-\mu\tau\eta} p_\alpha(\eta) d\eta$.

The next task is to look for the asymptotic behaviour of the integrals I_1 and I_2 for $x/\tau \to \infty$ with a fixed τ. We first consider the asymptotic behaviour of I_2. By considering the fact that for $\eta > 0$ the Lévy distribution $p_\alpha(\eta)$ exhibits fat tails as $\sim \eta^{-(\alpha+1)}$ (Mainardi et al., 2007; del Castillo-Negrete, 2009), and integration by parts, we get

$$\begin{aligned} I_2 \sim \int_{x/\tau}^{\infty} e^{-\mu\tau\eta}\eta^{-(\alpha+1)} d\eta &= \left[\frac{-1}{\mu\tau} e^{-\mu\tau\eta}\eta^{-(\alpha+1)}\right]_{\eta=x/\tau}^{\eta=\infty} \\ &- \frac{\alpha+1}{\mu\tau}\int_{x/\tau}^{\infty} e^{-\mu\tau\eta}\eta^{-(\alpha+2)} d\eta \\ &= \frac{\tau^\alpha}{\mu}\frac{e^{-\mu x}}{x^{\alpha+1}} - \frac{\alpha+1}{\mu\tau}\int_{x/\tau}^{\infty} e^{-\mu\tau\eta}\eta^{-(\alpha+2)} d\eta \\ &\sim \frac{\tau^\alpha}{\mu}\frac{e^{-\mu x}}{x^{\alpha+1}}. \end{aligned} \tag{3.29}$$

For the first integral I_1, if we define a cutoff Ω with $1 \ll \Omega < x\tau$ so that $p_\alpha(\eta) \sim \eta^{-(\alpha+1)}$, we can then write the integral I_1 as

$$I_1 \sim \int_{-\infty}^{\Omega} e^{(\nu-\mu)\tau\eta} p_\alpha(\eta) d\eta + \int_{\Omega}^{x/\tau} e^{(\nu-\mu)\tau\eta}\eta^{-(\alpha+1)} d\eta. \tag{3.30}$$

Because of the exponential decay of $p_\alpha(\eta)$ at minus infinity (for more details, refer to Mainardi et al. (2007); del Castillo-Negrete (2009)), the first integral converges to a finite value C. By applying an integration by parts to the second integral of Eq. (3.30), we get

$$\begin{aligned} \int_{\Omega}^{x/\tau} e^{(\nu-\mu)\tau\eta}\eta^{-(\alpha+1)} d\eta &= \left[\frac{1}{(\nu-\mu)\tau} e^{(\nu-\mu)\tau\eta}\eta^{-(\alpha+1)}\right]_{\eta=\Omega}^{\eta=x/\tau} \\ &+ \frac{\alpha+1}{(\nu-\mu)\tau}\int_{\Omega}^{x/\tau} e^{(\nu-\mu)\tau\eta}\eta^{-(\alpha+2)} d\eta \\ &\sim \frac{\tau^\alpha}{\nu-\mu}\frac{e^{(\nu-\mu)x}}{x^{\alpha+1}} \end{aligned}$$

Therefore,

$$I_1 \sim C + \frac{\tau^\alpha}{\nu - \mu} \frac{e^{(\nu-\mu)x}}{x^{\alpha+1}}. \tag{3.31}$$

By substituting Eqs. (3.29) and (3.31) into Eq. (3.28), we get

$$I(x,t) \sim ACe^{-\nu x+(1-\theta)t} + A\left(\frac{1}{\nu-\mu} + \frac{1}{\mu}\right)\frac{t}{x^{\alpha+1}} e^{-\mu x+(1-\theta)t}, \tag{3.32}$$

where $\nu \neq \mu$ and $\mu \neq 0$.

In order to find the asymptotic behaviour of $I(x,t)$ for large x, one can find the dominant term in Eq. (3.32) by considering the relative values of ν and μ.

If $\mu < \nu$, the truncation decays slower than the initial condition. In that case, the second term of Eq. (3.32) is the dominant term for large x, i.e.,

$$I(x,t) \sim A\left(\frac{1}{\nu-\mu} + \frac{1}{\mu}\right)\frac{t}{x^{\alpha+1}} e^{-\mu x+(1-\theta)t}. \tag{3.33}$$

By considering the expansion of the exponential function $e^{-\mu x}$, we get

$$I(x,t) \sim A\left(\frac{1}{\nu-\mu} + \frac{1}{\mu}\right) te^{(1-\theta)t}\frac{1}{x^{\alpha+1}}\left(1 - \mu x + \frac{\mu^2}{2}x^2 - \dots\right). \tag{3.34}$$

For $\mu x \ll 1$, the solution of $I(x,t)$ thus decays algebraically as

$$I(x,t) \sim te^{(1-\theta)t}x^{-(\alpha+1)}, \tag{3.35}$$

However, for $\mu x \gg 1$, the algebraic decaying tail of the solution is tempered with the exponential factor $e^{-\mu x}$ as

$$I(x,t) \sim te^{-\mu x+(1-\theta)t}x^{-(\alpha+1)}. \tag{3.36}$$

If $\mu > \nu$, the truncation decays faster than the initial condition. In that case, the first term of Eq. (3.32) is the dominant term for large x, i.e.,

$$I(x,t) \sim e^{-\nu x+(1-\theta)t}, \tag{3.37}$$

which shows an exponentially decaying tail of the solution.

Until now, we have assumed that $\nu \neq \mu$. To explore the case $\nu = \mu$, we cannot use Eq. (3.32). Instead, we need to go back to Eq. (3.30) and write the integral I_1 as

$$I_1 \sim \int_{-\infty}^{\Omega} p_\alpha(\eta) d\eta + \int_{\Omega}^{x/\tau} \eta^{-(\alpha+1)} d\eta. \tag{3.38}$$

By defining the finite value $C = \int_{-\infty}^{\Omega} p_\alpha(\eta) d\eta$ and solving the second integral of Eq. (3.38), we have

$$I_1 \sim C - \frac{\tau^\alpha}{\alpha} \frac{1}{x^\alpha}. \tag{3.39}$$

By substituting Eqs. (3.29) and (3.39) into (3.28), we obtain the solution $I(x,t)$ as

$$I(x,t) \sim ACe^{-\nu x + (1-\theta)t} + A\left(\frac{1}{\mu x^{\alpha+1}} - \frac{1}{\alpha x^\alpha}\right) te^{-\nu x + (1-\theta)t}. \tag{3.40}$$

In this case, the first term of Eq. (3.40) decays slower than the other term. Therefore, it is the dominant term for large x. We conclude that for the case $\nu = \mu$, the solution tail exhibits an exponentially decaying as

$$I(x,t) \sim e^{-\nu x + (1-\theta)t} \tag{3.41}$$

Obviously, the solution of Eq. (3.21), the susceptibles equation, is obtained from the solution of the infectives equation. Thus, the asymptotic behaviour of the susceptible front is the same as the infective front.

The above results are based on the assumption $\mu \neq 0$. However, in the absence of the truncation parameter, i.e., $\mu = 0$, we have to explore the asymptotic behaviour of the following integrals

$$I_1 = \int_{-\infty}^{x/\tau} e^{\nu\tau\eta} p_\alpha(\eta) d\eta, \qquad I_2 = \int_{x/\tau}^{\infty} p_\alpha(\eta) d\eta. \tag{3.42}$$

The analysis of the asymptotic behaviour of these integrals has been studied in (Hanert et al., 2011) and it was shown that the solution $I(x,t)$ has the same algebraically decaying tail as Eq. (3.35).

In order to derive the epidemic speed, we first compute a Lagrangian trajectory $x_L(t)$ of infective fronts such that $I(x_L(t),t) = I_0$, where $I_0 \approx 0$. Given $x_L(t)$, the epidemic speed is given by $c(t) = dx_L(t)/dt$.

In the case of a power-law decaying tail, we find $x_L(t)$ from Eq. (3.35) such that $I(x_L(t),t) = te^{(1-\theta)t}x_L(t)^{-(\alpha+1)} = I_0$. After some calculation, $x_L(t)$ and $c(t)$ can be computed as

$$x_L(t) = I_0^{-1/(\alpha+1)}t^{1/(\alpha+1)}e^{((1-\theta)/(\alpha+1))t}, \quad c(t) \sim (1-\theta)e^{((1-\theta)/(\alpha+1))t}. \tag{3.43}$$

For the truncated algebraically decaying tail, we use Eq. (3.36) to find $I(x_L(t),t) = te^{-\mu x_L(t)+(1-\theta)t}x_L(t)^{-(\alpha+1)} = I_0$. Thus, $x_L(t)$ satisfies the following equation

$$\ln t + (1-\theta)t - \mu x_L(t) - (\alpha+1)\ln x_L(t) = \ln I_0, \tag{3.44}$$

and $c(t)$ can be expressed as

$$c(t) = \frac{(1-\theta) + \dfrac{1}{t}}{\mu + \dfrac{\alpha+1}{x_L(t)}}. \tag{3.45}$$

When $t \to \infty$, the velocity of the fronts converges towards a constant value representing the maximum value of the epidemic speed given by $c_{max} = (1-\theta)/\mu$.

Finally, in the case of exponentially decaying tail, we can use Eq. (3.37) to find $I(x_L(t),t) = e^{-\nu x_L(t)+(1-\theta)t} = I_0$. Thus, $x_L(t) = (-\ln I_0 + (1-\theta)t)/\nu$ and the front moves at a constant velocity $c(t) = \bar{c} = (1-\theta)/\nu$.

3.3.3.2 Theoretical analysis (left-propagating front)

For exploring the impact of the left-sided truncated operator defined by Eq. (3.9) on the left-moving fronts, we consider a travelling-

wave solution of a constant shape as follows:

$$I(x,t) = I(z), \quad s(x,t) = s(z), \quad z = x + ct,$$

where c represents the speed of the epidemic waves moving to the left side. Substituting this solution into Eqs. (3.21) and (3.22), one can find the following system:

$$c\frac{\partial s}{\partial z} = I, \tag{3.46}$$

$$c\frac{\partial I}{\partial z} = (1-\theta)I + e^{-\mu z}\,{}_{-\infty}D_z^{\alpha}(e^{\mu z}I). \tag{3.47}$$

Now we define a solution of the following form

$$I(z) = \hat{I}e^{kz}, \quad s(z) = \hat{s}e^{kz}, \tag{3.48}$$

where k is a parameter depending on the value of c. Considering the fact that ${}_{-\infty}D_z^{\alpha}e^{kz} = k^{\alpha}e^{kz}$ and substituting the solutions (3.48) into Eqs. (3.46) and (3.47), we get the following system:

$$\begin{bmatrix} ck & -1 \\ 0 & ck - (k+\mu)^{\alpha} - (1-\theta) \end{bmatrix} \begin{bmatrix} \hat{s} \\ \hat{I} \end{bmatrix} = \begin{bmatrix} 0 \\ 0 \end{bmatrix}. \tag{3.49}$$

If $ck(ck - (k+\mu)^{\alpha} - (1-\theta)) = 0$, we can find a non-trivial solution. In that case, we get the following relation representing the value of the epidemic speed as a function of the parameter k:

$$c(k) = \frac{1-\theta}{k} + \frac{(k+\mu)^{\alpha}}{k}. \tag{3.50}$$

In order to obtain the minimum epidemic speed, one can minimize Eq. (3.50) with respect to k. For $0 < \alpha < 2$ and $\mu \neq 0$, we cannot analytically calculate the minimum speed c_{min}. In the next section, we thus find it numerically. However, for $0 < \alpha < 2$ and $\mu = 0$, as it is discussed in (Hanert et al., 2011), $c_{min} = \alpha\left((1-\theta)/(\alpha-1)\right)^{(\alpha-1)/\alpha}$ and the corresponding rate of the exponential decay is equal to $k_{min} = \left((1-\theta)/(\alpha-1)\right)^{1/\alpha}$. For $\alpha = 2$, the minimum speed of the classical model is given by $c_{min} = 2\sqrt{1-\theta}$.

3.4 Numerical examples

In order to illustrate the analytical results obtained for the asymptotic behaviour of the infective waves, we numerically solve the model equations on a finite domain $[0, L]$, where $L > 0$. Here, we have used the same method as the one performed by Vallaeys et al. (2017) for solving a symmetric truncated fractional-order diffusion equation. To study more numerical methods for solving the space fractional-order diffusion equations, refer to (Hanert, 2011; Piret and Hanert, 2013; Hanert and Piret, 2014). We discretize Eqs. (3.19) and (3.20) by finite-element (FE) method based on a Galerkin formulation. To illustrate this method more precisely, we discretize the following simple diffusion equation:

$$\frac{\partial I(x,t)}{\partial t} = e^{-\lambda x}\,{}_0D_x^{\alpha}(e^{\lambda x} I(x,t)) - \lambda^{\alpha} I(x,t). \tag{3.51}$$

In this method, the exact solution (unknown variable) $I(x,t)$ is expressed as a sum of the unknown coefficients $e_j(t)$ and basis functions $\phi_j(x)$ as follows:

$$I(x,t) \approx \tilde{I}(x,t) = \sum_{j=1}^{N} e_j(t)\phi_j(x). \tag{3.52}$$

By introducing a partition of the domain $[0, L]$ into $N-1$ subintervals $[x_j, x_{j+1}]$ with a constant length h, i.e., $x_1 = 0, x_N = L$, and $x_{j+1} - x_j = h$ for $j = 1, \ldots, N-1$, we can consider the piecewise linear basis functions $\phi_j(x)$ for $j = 1, 2, \ldots, N$ as follows:

$$\phi_1(x) = \begin{cases} \dfrac{x_2 - x}{x_2 - x_1} & : x_1 \le x \le x_2, \\ 0 & : x \notin [x_1, x_2]. \end{cases}$$

for $j = 2, \ldots, N-1$,

$$\phi_j(x) = \begin{cases} \dfrac{x - x_{j-1}}{x_j - x_{j-1}} & : x_{j-1} \le x \le x_j, \\ \dfrac{x_{j+1} - x}{x_{j+1} - x_j} & : x_j \le x \le x_{j+1}, \\ 0 & : x \notin [x_{j-1}, x_{j+1}]. \end{cases}$$

and for $j = N$,

$$\phi_N(x) = \begin{cases} \dfrac{x - x_{N-1}}{x_N - x_{N-1}} & : x_{N-1} \leq x \leq x_N, \\ 0 & : x \notin [x_{N-1}, x_N]. \end{cases}$$

We also discretize the exponentially truncated unknown solution, i.e., $e^{\lambda x} I(x,t)$ as follows

$$e^{\lambda x} I(x,t) \approx \tilde{I}^l(x,t) = \sum_{j=1}^{N} e_j^l(t)\phi_j(x). \tag{3.53}$$

where $e_j^l(t)$ is the unknown coefficient corresponding to the left truncated solution.

By using a Galerkin formulation, we replace $\tilde{I}(x,t)$ and $\tilde{I}^l(x,t)$ in Eq. (3.51) and then by orthogonalizing the discrete equation with respect to all ϕ_j, we get the following equation:

$$\begin{aligned} \left(\int_0^L \phi_i \phi_j dx\right) \frac{de_j}{dt}(t) &= \left(\int_0^L \phi_i e^{-\lambda x}\, {}_0D_x^\alpha \phi_j dx\right) e_j^l(t) \\ &- \lambda^\alpha \left(\int_0^L \phi_i \phi_j dx\right) e_j(t), \end{aligned}$$

for $i, j = 1, \ldots, N$.

By introducing the following matrices

$$\mathbf{M} := \int_0^L \phi_i \phi_j dx, \qquad \mathbf{D} := \int_0^L \phi_i e^{-\lambda x}\, {}_0D_x^\alpha \phi_j dx,$$

we get the following semi-discrete equation in a matrix form

$$\mathbf{M}\frac{d\mathbf{e}}{dt}(t) = \mathbf{D}\mathbf{e}^l(t) - \lambda^\alpha \mathbf{M}\mathbf{e}(t), \tag{3.54}$$

where $\mathbf{e}(t) = [e_1(t) \ldots e_N(t)]^T$ and $\mathbf{e}^l(t) = \left[e_1^l(t) \ldots e_N^l(t)\right]^T$ are the vector of unknown coefficients at time t. It should be noted that by considering the same method in (Hanert, 2010), the diffusion matrix $\mathbf{D}$ can be expressed as: $\mathbf{D} = -\int_0^L e^{-\lambda x}(\frac{d\phi_i}{dx} - \lambda\phi_i)\, {}_0D_x^{\alpha-1}\phi_j dx$.

Here we use the left Caputo derivative of order $\alpha - 1$ of ϕ_j defined by Eq. (3.5) as Caputo derivatives are easier to handle and also for many applications could prevent mass-balance errors on bounded domains, while such errors can be made by Riemann–Liouville derivatives (for more details, see (Zhang et al., 2007)).

In order to solve Eq. (3.54), the vector $\mathbf{e}^l(t)$ needs to be computed in terms of the vector $\mathbf{e}(t)$. To do so, we use Galerkin formulation for Eqs. (3.52) and (3.53) as follows:

$$\int_0^L \phi_i e^{\lambda x} \tilde{I} dx = \int_0^L \phi_i \tilde{I}^l dx \longrightarrow \left(\int_0^L \phi_i e^{\lambda x} \phi_j dx \right) e_j(t) = \left(\int_0^L \phi_i \phi_j dx \right) e_j^l(t).$$

By defining the matrix

$$\mathbf{W} := \int_0^L \phi_i e^{\lambda x} \phi_j dx,$$

we get $\mathbf{e}^l(t) = \mathbf{M}^{-1}\mathbf{W}\mathbf{e}(t)$. we can thus express Eq. (3.54) as follows

$$\mathbf{M}\frac{d\mathbf{e}}{dt}(t) = \left(\mathbf{D}\mathbf{M}^{-1}\mathbf{W} - \lambda^{\alpha}\mathbf{M}\right)\mathbf{e}(t), \tag{3.55}$$

Finally, in order to discretize Eq. (3.55), we use a third-order Adams–Bashforth method.

In order to solve the model Eqs. (3.19) and (3.20), we use the following initial conditions:

$$S(x, t = 0) = S_0(x) = 1 - h_S \left(1 \pm \tanh\left(\frac{x - x_0}{w_s L}\right)\right),$$

$$I(x, t = 0) = I_0(x) = \begin{cases} h_I e^{-\nu(x - x_0)} & : x \geq x_0, \\ h_I e^{\nu(x - x_0)} & : x \leq x_0, \end{cases}$$

where $h_S = 0.37, w_S = 0.003, h_I = 0.14$, and $\nu = 0.001$. we consider the "+" sign and $x_0 = 9L/10$ for the left-moving front and

the "−" sign and $x_0 = L/30$ for the right-moving front. The dimensionless length of the domain is set to $L = 10^5$ and $L = 3 \times 10^5$ for the left- and right-moving fronts, respectively. For all simulations, $\theta = 0.5$, and the value of the fractional order α is set to 1.2. According to the analytical results, we can consider three different asymptotic behaviours for the right-moving fronts, i.e., $y_1 = x^{-(\alpha+1)}$ (power-law decay), $y_2 = e^{-\mu x} x^{-(\alpha+1)}$ (truncated power-law decay), and $y_3 = e^{-\mu x}$ (exponential decay). In what follows, we shall show how different values of the truncation parameter μ lead to these different asymptotic behaviours.

The algebraic decaying tail of the right-moving fronts are shown in Figure 3.1. Here, we take $\mu = 5 \times 10^{-6} < \nu$. Figure 3.1(a) shows the densities of both the susceptibles and infectives at different times. Figure 3.1(b) and 3.1(c) show that the right-moving fronts for both the susceptibles and infectives exhibit a power-law decaying tail as $y_1 = x^{-(\alpha+1)}$. The Lagrangian trajectory $x_L(t)$ and the epidemic speed $c(t)$ corresponding to this case are shown in Figure 3.2(a) and 3.2(b), respectively.

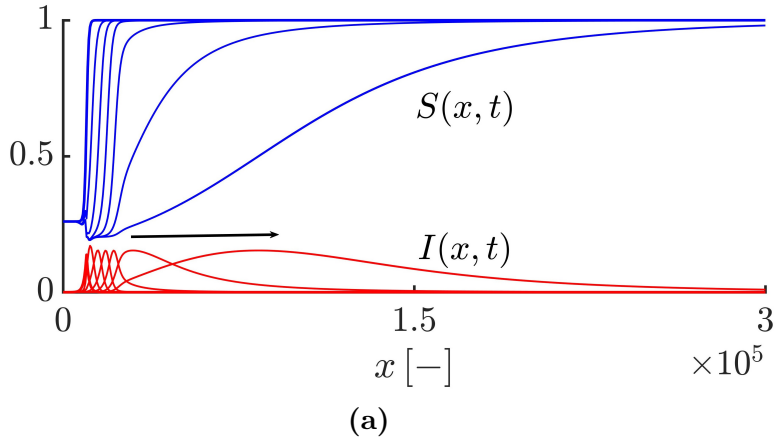

(a)

Fig. 3.1: *Cont.*

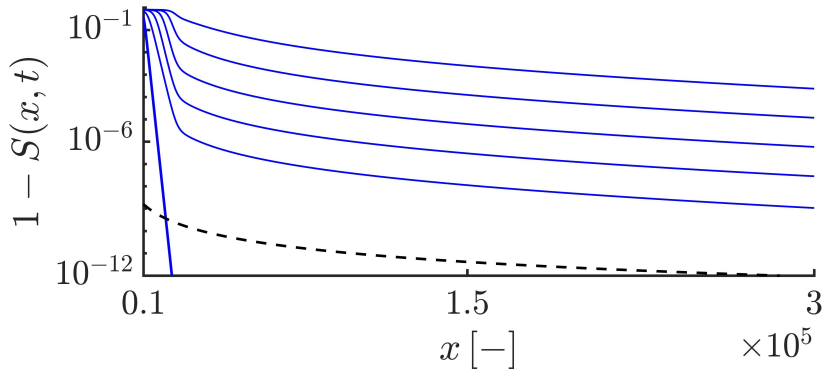

(b)

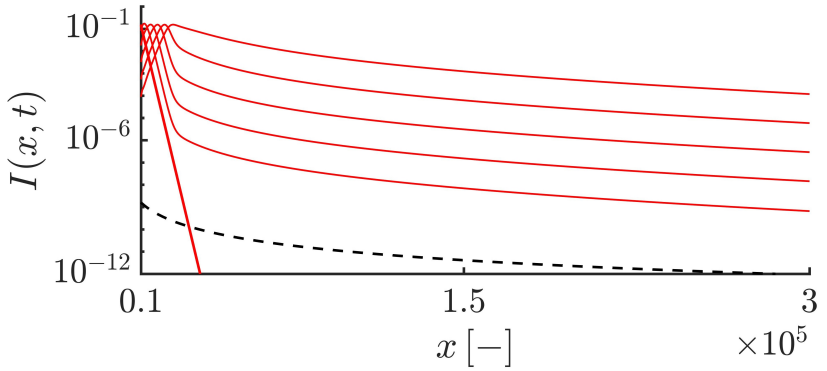

(c)

Fig. 3.1: (**a**) Profiles of the susceptible and infective waves moving to the right side at different times obtained by solving Eqs. (3.19) and (3.20) with $\alpha = 1.2$ and $\mu = 5 \times 10^{-6} < \nu$. The arrow shows the direction of the front propagation. (**b**,**c**) Highlighting an algebraic decaying tail for the susceptible and infective waves, i.e., $1 - S$ and $I \sim y_1 = x^{-(\alpha+1)}$ shown by the black dashed curves. The duration of the simulation and the time interval between curves equal 30 and 6, respectively.

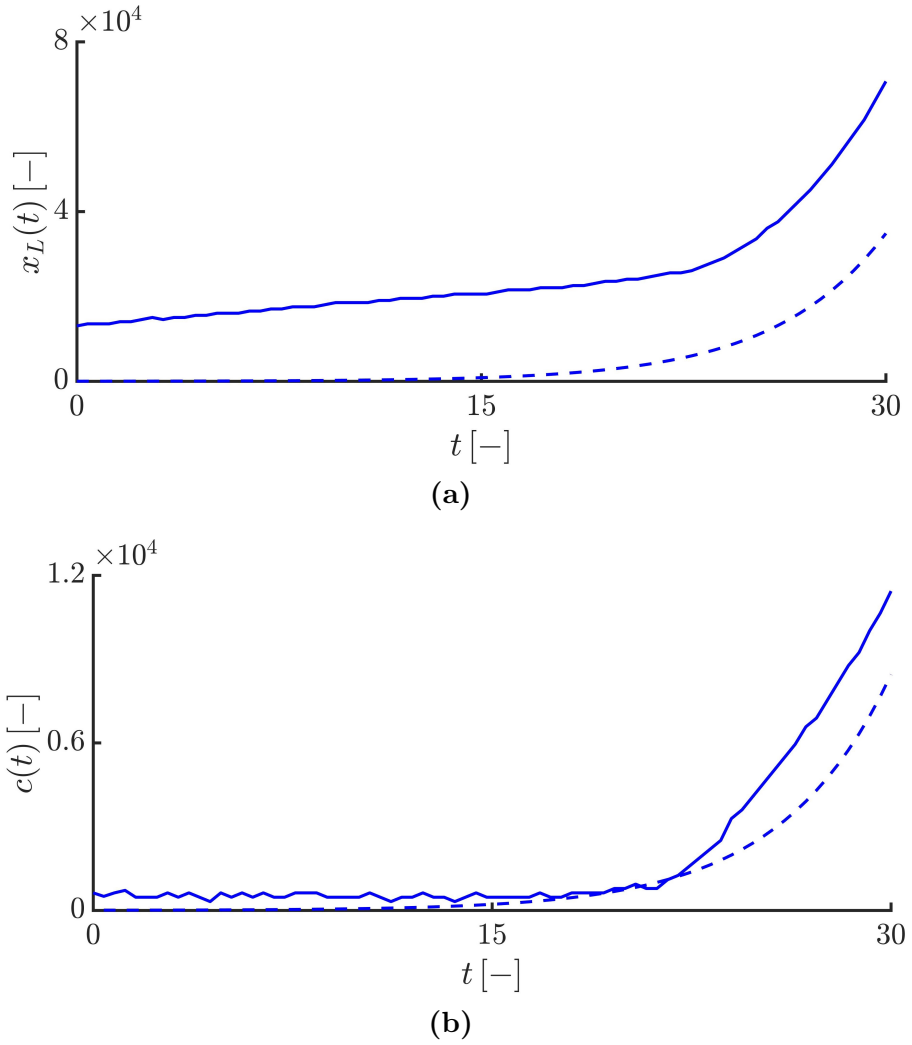

Fig. 3.2: (**a**) Time evolution of the Lagrangian trajectory $x_L(t)$ at the leading edge of the infective waves such that $I(x_L(t), t) = I_0$, where $I_0 = 0.01$. The value of μ is equal to 5×10^{-6}. The dashed curve corresponds to the asymptotic expansion of the Lagrangian trajectory, i.e., $x_L(t) \sim t^{1/(\alpha+1)} e^{((1-\theta)/(\alpha+1))t}$. (**b**) Time evolution of the instantaneous velocity of the right-propagating infective waves obtained by $c(t) = dx_L(t)/dt$. The dashed curve corresponds to the asymptotic expansion of the Lagrangian velocity, i.e., $c(t) \sim (1-\theta) e^{((1-\theta)/(\alpha+1))t}$, highlighting the exponential speed of the epidemic and also the agreement of the numerical result with the analytical velocity.

Figure 3.2(a) shows the time evolution of the Lagrangian trajectory $x_L(t)$ such that $I(x_L(t), t) = I_0$, where $I_0 = 0.01$. Figure 3.2(b) shows the time evolution of the numerical estimation of the instantaneous speed of the points with density $I_0 = 0.01$. Both Figure 3.2(a) and 3.2(b) also show that the results obtained numerically agree well with the asymptotic expansions obtained by Eq. (3.43). It should be noted that the truncation parameter here has no influence on the rapid propagation of the epidemic and the fronts move at an exponential speed similar to the fractional-order epidemic model based on pure Lévy flights (Hanert et al., 2011).

By increasing the value of the truncation parameter μ, the algebraically decaying tail of the solutions can be tamed. If we take $\mu = 10^{-4} < \nu$, both the susceptible and infective fronts propagate so that their tails exhibit a tempered algebraic decaying, i.e., $1 - S$ and $I \sim y_2 = e^{-\mu x} x^{-(\alpha+1)}$ (see Figure 3.3).

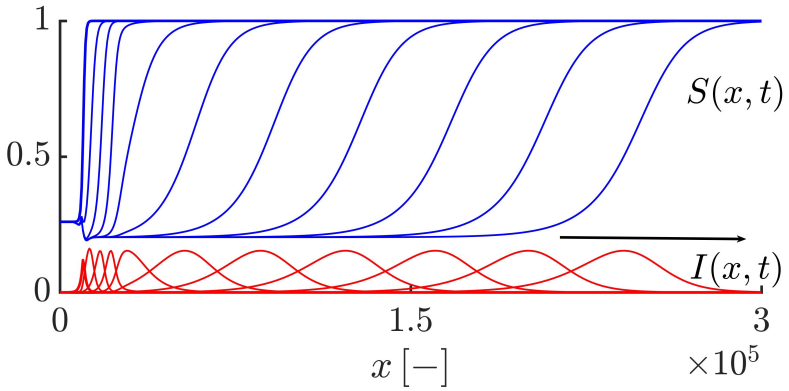

(a)

Fig. 3.3: *Cont.*

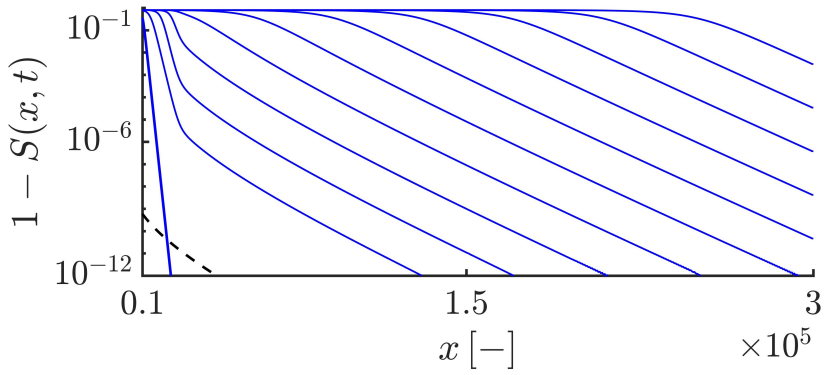

(b)

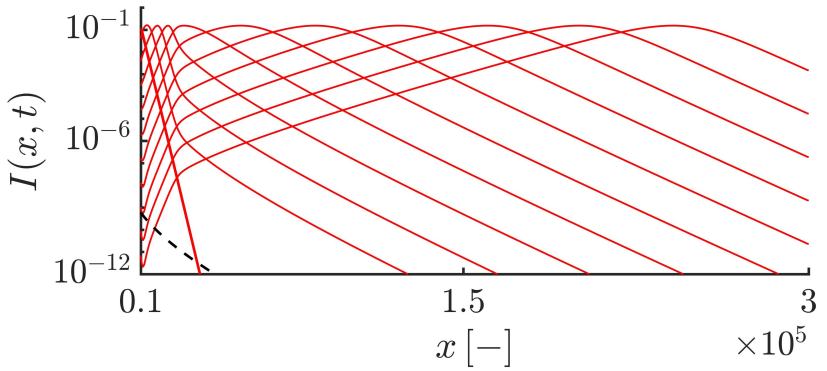

(c)

Fig. 3.3: (**a**) Profiles of the susceptible and infective waves moving to the right side at different times obtained by solving Eqs. (3.19) and (3.20) with $\alpha = 1.2$ and $\mu = 10^{-4} < \nu$. The arrow shows the direction of the front propagation. (**b**,**c**) Highlighting an exponentially tempered algebraic decaying tail for the susceptible and infective waves, i.e., $1 - S$ and $I \sim y_2 = e^{-\mu x} x^{-(\alpha+1)}$ shown by the black dashed curves. The duration of the simulation and the time interval between curves equal 90 and 9, respectively.

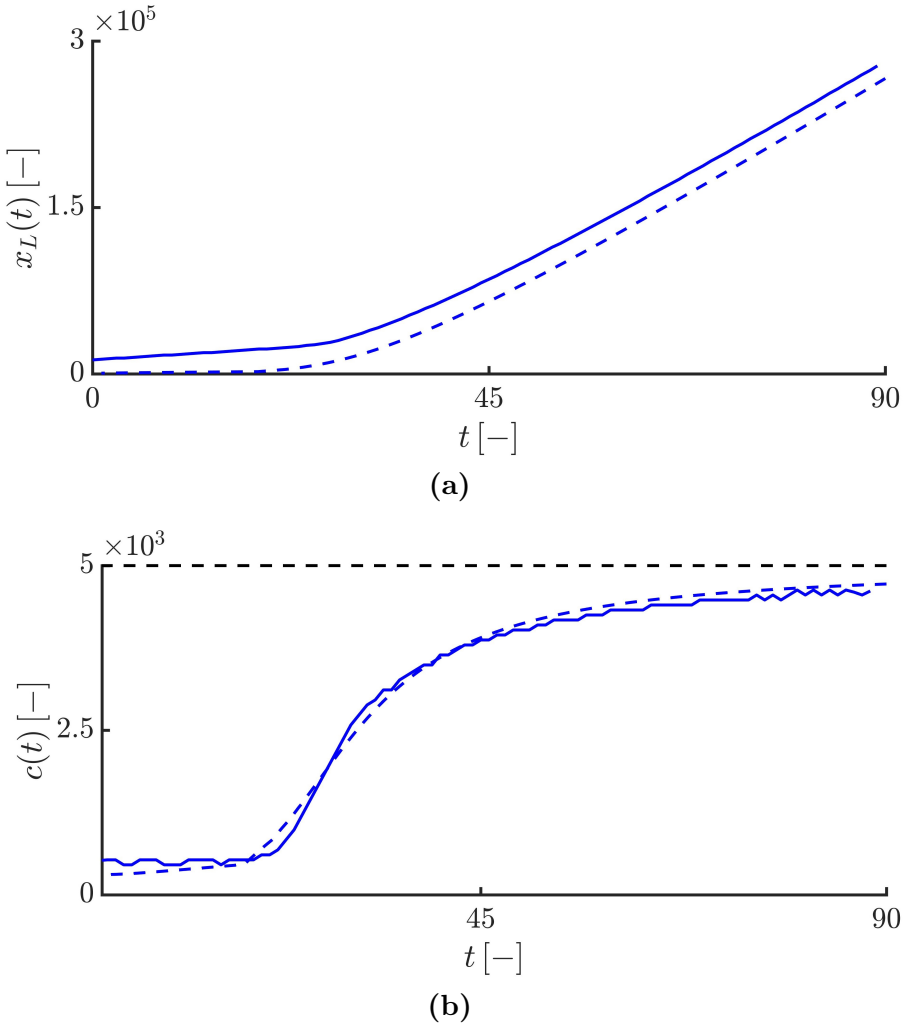

Fig. 3.4: (**a**) Time evolution of the Lagrangian trajectory $x_L(t)$ at the leading edge of the infective waves such that $I(x_L(t),t) = I_0$, where $I_0 = 0.01$. The value of μ is equal to 10^{-4}. The dashed curve corresponds to the analytical Lagrangian trajectory satisfies in the equation $\ln t+(1-\theta)t-\mu x_L(t)-(\alpha+1)\ln x_L(t) = \ln I_0$. (**b**) Time evolution of the instantaneous velocity of the right-propagating infective waves obtained by $c(t) = dx_L(t)/dt$. The dashed curve corresponds to the analytical Lagrangian velocity obtained by $c(t) = ((1-\theta)+1/t)/(\mu+(\alpha+1)/x_L(t))$, highlighting the agreement of the numerical result with the analytical velocity and also the convergence of the epidemic speed towards the maximum epidemic speed value $c_{max} \approx 5 \times 10^3$ (see the black dashed line).

Figure 3.4 shows that the Lagrangian trajectory $x_L(t)$ and the velocity $c(t)$ obtained by numerically solving Eqs. (3.19) and (3.20) are in good agreement with the results obtained analytically by Eqs. (3.44) and (3.45). As expected, the infective fronts initially propagate at the minimum average speed $c_{min} = 5 \times 10^2$ and then the front speed gradually increases so that after some time, it converges towards the maximum front speed value $c_{max} = 5 \times 10^3$.

Figure 3.5 shows the dynamics of the right-moving susceptible and infective fronts for $\mu = 10^{-3}$. As expected, for $\mu \geq \nu$, the tails of the solutions for the susceptible and infective fronts exhibit an exponential decay, i.e, $1 - S$ and $I \sim y_3 = e^{-\nu x}$ (see Figure 3.5(b) and 3.5(c)).

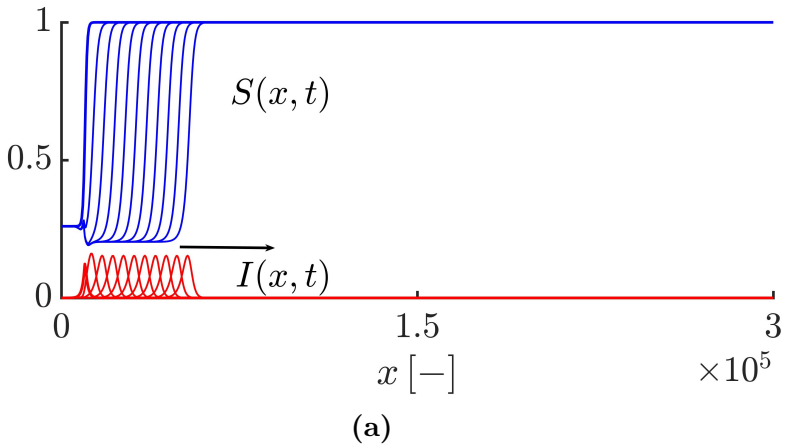

(a)

Fig. 3.5: *Cont.*

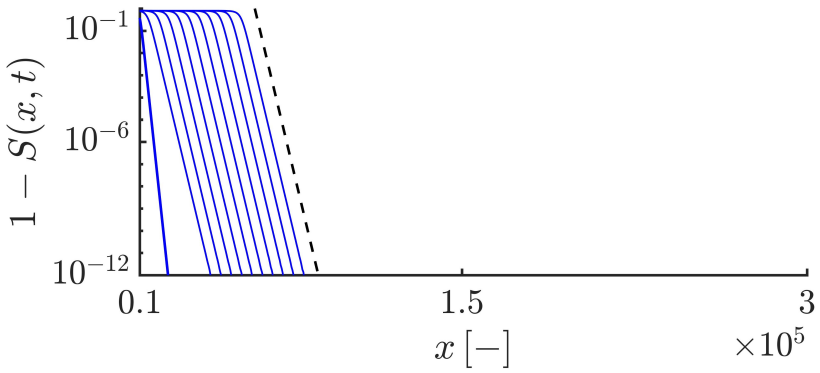

(b)

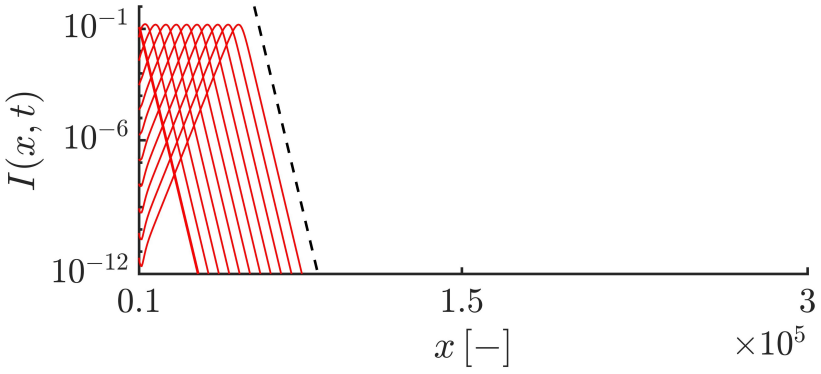

(c)

Fig. 3.5: (**a**) Profiles of the susceptible and infective waves moving to the right side at different times obtained by solving Eqs. (3.19) and (3.20) with $\alpha = 1.2$ and $\mu = 10^{-3} = \nu$. The arrow shows the direction of the front propagation. (**b**,**c**) Highlighting an exponential decaying tail for the susceptible and infective waves, i.e., $1 - S$ and $I \sim y_3 = e^{-\nu x}$ shown by the back dashed curves. The duration of the simulation and the time interval between curves equal 90 and 9, respectively.

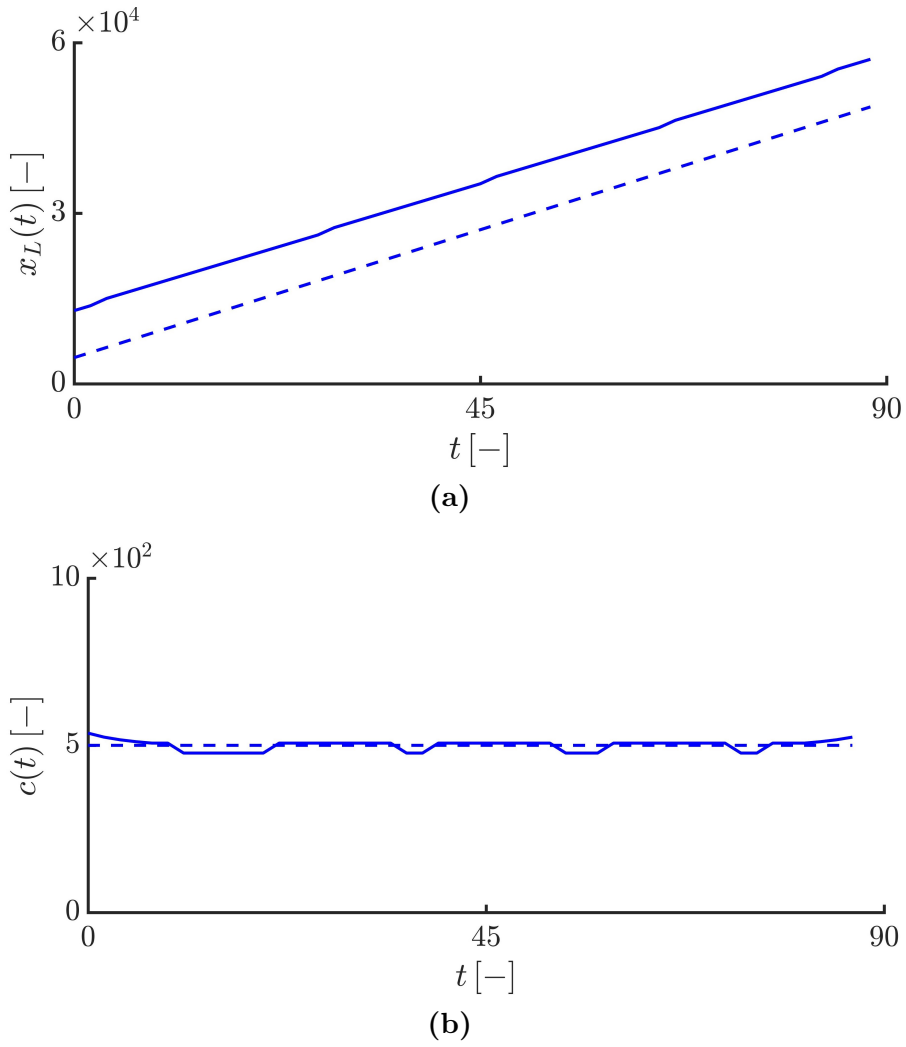

Fig. 3.6: (**a**) Time evolution of the Lagrangian trajectory $x_L(t)$ at the leading edge of the infective waves such that $I(x_L(t), t) = I_0$, where $I_0 = 0.01$. The value of μ is equal to 10^{-3}. The dashed curve corresponds to the asymptotic expansion of the Lagrangian trajectory, i.e., $x_L(t) = (-\ln I_0 + (1-\theta)t)/\nu$. (**b**) Time evolution of the instantaneous velocity of the right-propagating infective waves obtained by $c(t) = dx_L(t)/dt$. The dashed curve corresponds to the constant Lagrangian velocity, i.e., $c(t) = \bar{c} = (1-\theta)/\nu$, highlighting the agreement of the numerical result with the analytical velocity.

Figure 3.6 shows that the Lagrangian trajectory $x_L(t)$ and the velocity $c(t)$ obtained by numerically solving the model equations are in good agreement with the analytical results. In this case, similar to the classical epidemic models, the infective fronts propagate at a constant speed $c = 5 \times 10^2$. It should be noted that since in the first case ($\mu = 5 \times 10^{-6}$), the epidemic fronts propagate over the entire domain during a shorter time compared to the other cases ($\mu = 10^{-4}$ and $\mu = 10^{-3}$), for the first case, we consider the simulation duration equals 30. However, for the others, it is equal to 90.

Figure 3.7 shows the time evolution of the susceptible and infective waves propagating to the left side. Figure 3.7(a) shows the densities of the susceptibles and infectives at different times. Figure 3.7(b) and 3.7(c) show that the tails of the solutions decay exponentially as $\sim y = e^{\nu x}$. Here, the simulation duration is equal to 90. In this case, for all values of the truncation parameter, the fronts move at a constant velocity that is equal to $c = 5 \times 10^2$.

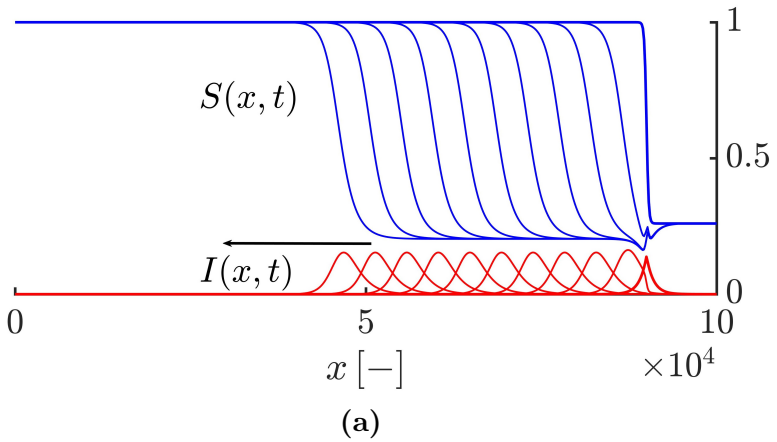

(a)

Fig. 3.7: *Cont.*

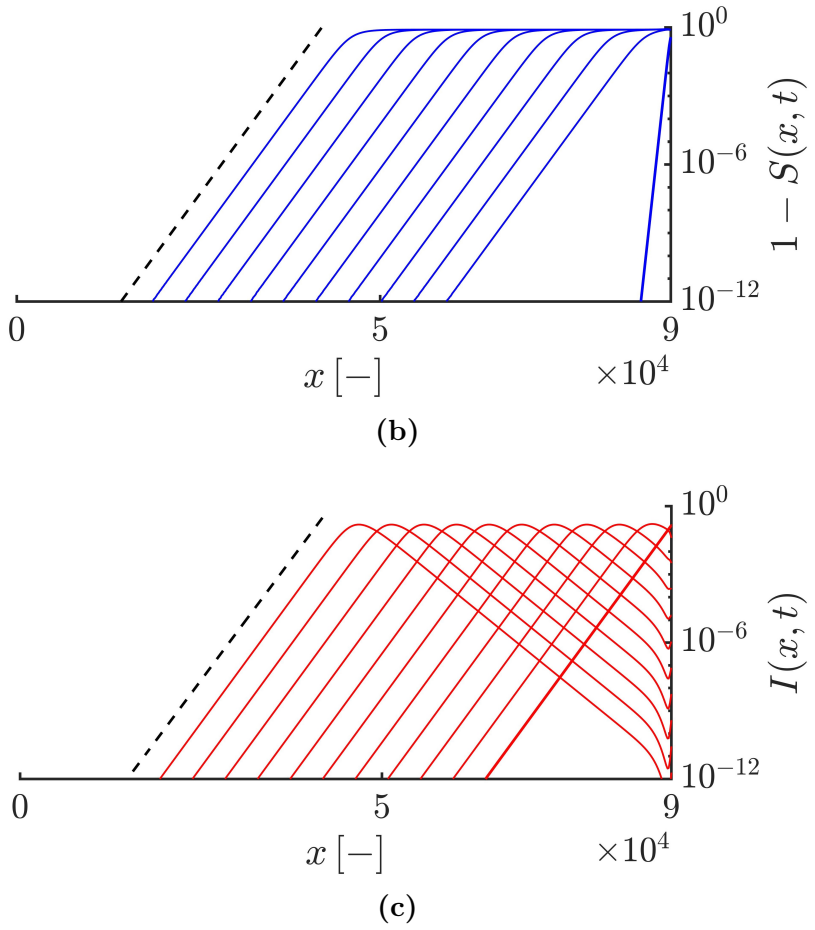

m

Fig. 3.7: (**a**) Profiles of the susceptible and infective waves moving to the left side at different times obtained by solving Eqs. (3.19) and (3.20) with $\alpha = 1.2$ and different values of the truncation parameter $\mu = 5 \times 10^{-6}, 10^{-4}$ and 10^{-3}. The arrow shows the direction of the front propagation. (**b**,**c**) Highlighting an exponential decaying tail for the susceptible and infective waves, i.e., $1 - S$ and $I \sim y = e^{\nu x}$ shown by the black dashed curves. The duration of the simulation and the time interval between curves equal 90 and 9, respectively.

It should be noted that when we consider both the left-and right-

sided truncated fractional-order diffusion operators by choosing the strict values of the skewness parameter β, i.e., $-1 < \beta < 1$, ($\beta = 0$ leads to a symmetric operator), both the left- and right-sided derivatives affect the epidemic speed and the asymptotic behaviour of the front's tail. In that case, both the left- and right-moving front tails exhibit the same asymptotic behaviour based on the values of the truncation parameter. For instance, if the truncation parameter μ is set to 10^{-4}, the tails of both the left- and right-moving fronts decay as $\sim e^{-\mu x} x^{-(\alpha+1)}$.

Figure 3.8(a) shows the time evolution of the Lagrangian trajectory $x_L(t)$ for the constant value of the fractional-order derivative $\alpha = 1.2$ and different values of the truncation parameter μ. As we see, in all cases, the values of $x_L(t)$ initially increase linearly at a constant speed on average equals 5×10^2 and then, for $\mu = 5 \times 10^{-6}$, $x_L(t)$ increases exponentially leading to an exponential and unbounded velocity of the infective fronts (see Figure 3.2(b)), but for $\mu = 10^{-4}$, $x_L(t)$ increases gradually leading to the convergence of the epidemic speed to the maximum velocity value $c_{max} \approx 5 \times 10^3$ (see Figure 3.4(b)), and finally for $\mu = 10^{-3}$, $x_L(t)$ increases linearly leading to the constant speed $c = 5 \times 10^2$ (see Figure 3.6(b)).

Figure 3.8(b) shows the time evolution of the Lagrangian trajectory $x_L(t)$ for different values of the fractional-order derivative α and a constant value of the truncation parameter $\mu = 10^{-4}$. Since, the value of μ is constant, in all cases the Lagrangian velocity converges towards a plateau showing the maximum average speed, but the time to reach that plateau is not the same for different values of α. As we see, the smaller the value of α, i.e., the closer it is to 1, the faster the Lagrangian trajectory accelerates leading to the faster convergence of the front speed towards the maximum speed compared to values of α that are closer to 2.

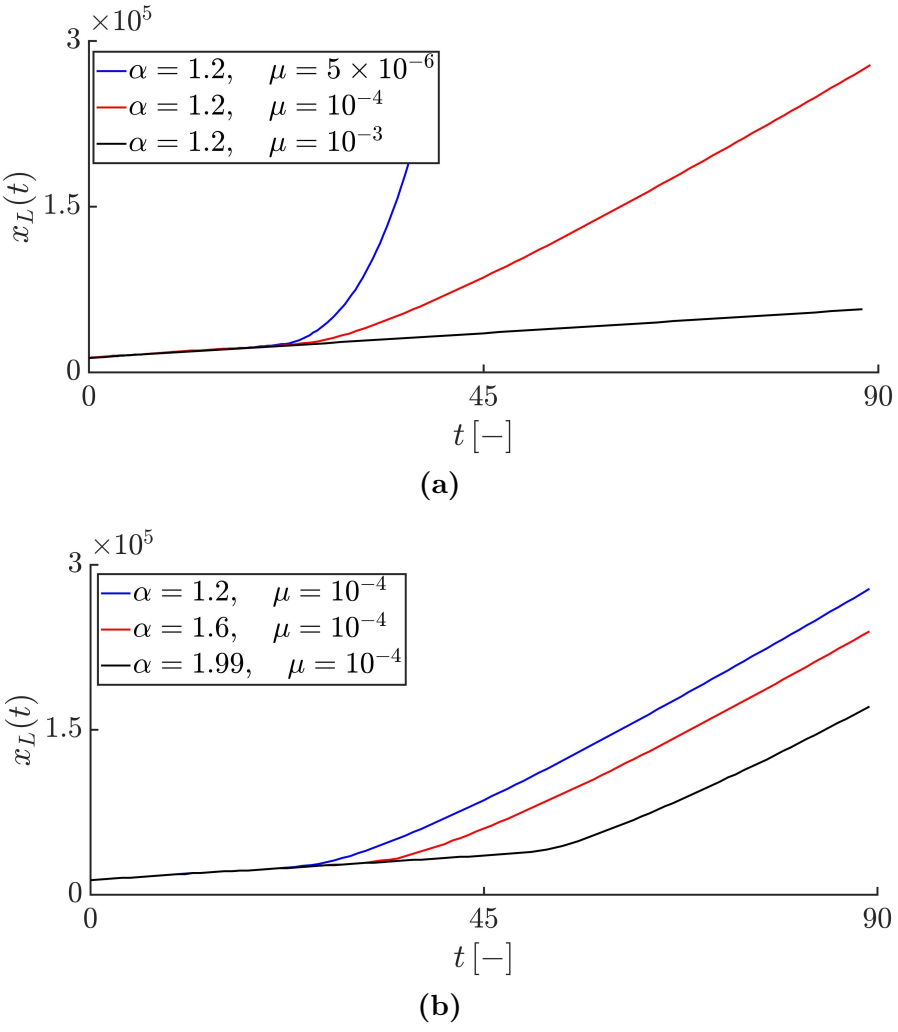

Fig. 3.8: (**a**) Time evolution of the Lagrangian trajectory for fractional-order derivative $\alpha = 1.2$ and different values of the truncation parameter μ. The blue, red and black curves correspond to $\mu = 5 \times 10^{-6}$, $\mu = 10^{-4}$, and $\mu = 10^{-3}$, respectively. (**b**) Time evolution of the Lagrangian trajectory for different values of the fractional-order derivative α and the truncation parameter $\mu = 10^{-4}$. The blue, red and black curves correspond to $\alpha = 1.2$, $\alpha = 1.6$, and $\alpha = 1.99$, respectively.

3.5 Conclusions

In this work, we have investigated the spatial propagation of the epidemics caused by infectious diseases. We have considered a simple version of the epidemic models consisting of susceptible and infective populations. The diffusion process resulting from the random mobility of the infective individuals is taken into account in our model. Based on the previous studies, in the case of the Brownian motion, the infective waves propagate into the susceptible population at a constant speed and the tails of the travelling-wave solutions exhibit an exponential decay, while in the case of pure (untruncated) Lévy flights, the left-sided fractional derivative leads to an exponential and unbounded speed of the infective waves moving to the right side, but generates a constant speed at the left side. In that case, right-moving fronts have an algebraic tail. However, left-moving fronts exhibit an exponential tail.

As a new study, we have applied the truncated Lévy flight to the proposed model. Similar to the results obtained for the λ-truncated fractional-order Fisher–Kolmogorov Equation (del Castillo-Negrete, 2009), for the right-moving fronts, we have shown that the epidemic speed is dependent on the level of the truncation parameter. In this case, we have considered a left-sided truncated fractional-order diffusion operator. For small values of λ ($\lambda \gtrsim 0$), the tails of the infective waves can decay algebraically leading to an exponential growth of the epidemics. In that case, the truncation has no impact on the superdiffusive epidemics. By increasing the value of λ, the algebraic decaying tails can be tamed leading to either an upper bound on the epidemic speed representing the maximum speed or the generation of the infective waves of a constant shape propagating at a minimum constant speed similar to the classical models (second-order diffusion epidemic models). For the left-moving fronts, our numerical results show that for different values of the truncation parameter, the truncated left-sided fractional derivative generates the waves of a constant shape moving at a constant speed. Obviously, considering the strict values of the skewness parameter

β, i.e., $-1 < \beta < 1$, leads to the effect of both the left-and right-sided truncated fractional-order diffusion operators on the epidemic speed. In that case, based on the value of the truncation parameter, the tails of both the left- and right-moving fronts have the same asymptotic behaviour.

From an applied perspective, the untruncated power laws (pure Lévy flights) have some drawbacks. As discussed in (Viswanathan et al., 2008), in nature, due to the finite space, landscape and physiological limitations, the occurrence of arbitrarily large displacements by the individuals following a pure Lévy flight is not realistic. In that case, one individual cannot make displacements beyond an upper bound. By introducing truncated power-laws, such an upper bound can thus be taken into account in the fractional-order diffusion models. As mentioned by Hanert et al. (2011), since modern epidemics caused by human infectious diseases can propagate over the entire globe very quickly, the untruncated fractional-order diffusion epidemic models can better represent such epidemics. However, concerning the infectious diseases of animals doing a Lévy flight, the propagation of the epidemics is smoother. Our findings thus suggest that truncated fractional-order diffusion models are more appropriate for modelling the animal diseases.

The space fractional-order epidemic models could be further improved by considering the non-Markovian diffusion processes in which the pdf for waiting times between displacements have a power-law asymptotic behaviour as $\sim \tau^{-(\gamma+1)}$, where $0 < \gamma < 1$. In that case, the time derivative of order one is replaced by a time fractional derivative of order γ (Metzler and Klafter, 2000). As an example of such diffusion processes, Brockmann et al. (2006) observed that the dispersion of bank notes has memory effects. In order to numerically solve time-space fractional diffusion equations, Hanert (2011) has proposed an efficient and flexible scheme.

CHAPTER 4

A tempered space fractional-order diffusion model of West Nile virus epidemics

Abstract

Understanding how fast epidemic waves propagate across an area is necessary to adopt control and mitigation strategies. The epidemic speed can be mathematically estimated by deriving reaction-diffusion models based on the pattern of infected host movements. West Nile virus (WNv) is an infectious disease that circulates between birds and mosquitoes as the primary and secondary hosts, respectively. For estimating the speed of the WNv epidemic across the USA

during 5 years (1999–2003), previous models were formulated based on the assumption that random movements of wild birds are described by a Brownian motion, which results in second-order reaction-diffusion models. In that case, the epidemic waves travel at a constant speed. However, based on some experiments, the WNv epidemic waves propagated rapidly across North America, leading to a non-constant epidemic speed. In addition, when using classical models, the estimated epidemic speed could be less than the observed range of the wave speed. One way to accelerate the epidemic front speed is to use a Lévy flight dispersion pattern instead of the Brownian motion. In that case, the resulting space fractional diffusion equation however overestimates the infected waves speed. Here, we develop a classical coupled reaction-diffusion model by assuming that the infected reservoirs (birds) could perform truncated Lévy flights, which yields a λ-truncated space-fractional-order diffusion model with order $1 < \alpha < 2$, where $\lambda > 0$ denotes the truncation parameter. Our numerical results confirm that the second-order diffusion model could lead to underestimating the epidemic speed while our proposed model has the potential to rectify this problem. With the new model, the speed initially increases and then reaches a constant and maximum value, which falls within the real speed range. Moreover, we show that the closer the value of α to 1, the faster the epidemic waves reach the maximum speed, and also that for different biting rates, the value of truncation parameter plays an important role in estimating the epidemic speed. We suggest that with the Lévy flight assumption, truncated space-fractional-order diffusion models can provide appropriate estimations of the epidemic speed that is underestimated and overestimated by the models based on pure Brownian and Lévy movements, respectively.

4.1 Introduction

West Nile virus (WNv) is an infectious pathogen that has affected the health of both birds and humans since its outbreak in the USA in 1999. The name of the virus originates from its first identification in the West Nile area of Uganda in 1937 (Smithburn et al., 1940). Several outbreaks have occurred since then in Europe, West Asia, the Middle East, and Africa (Hubálek and Halouzka, 1999; Murgue et al., 2001). In 1999, WNv entered the Western Hemisphere following its emergence in New York and then quickly propagated throughout the USA, leading to an epidemic during 5 years (1999–2003), and hence increased mortality among humans and many species of birds (Nash et al., 2001). In subsequent years, the virus reached central America, Canada, and many central European countries (Giordano et al., 2017; Ziegler et al., 2019).

WNv is classified within mosquito-borne zoonotic diseases and has multiple hosts. A wide variety of wild and domestic birds (more than 300 species) can act as reservoirs to the virus, and humans and other mammals, such as horses are considered incident hosts (Marra et al., 2004). Multiple species of mosquitoes in the culicine family, such as *Culex* are the intermediate (secondary) hosts (Darsie Jr and Ward, 1981). The mechanism of the infection transmission is not direct, i.e., animal to animal or person to person. Indeed, the mosquitoes (vectors) transmit the virus by taking the blood-meals from the birds and humans (Molaei et al., 2006).

For the last two decades, scientists have been utilizing mathematical models to study the temporal and spatial dynamics of WNv based on different characteristics of the birds and mosquitoes populations (Bowman et al., 2005; Kenkre et al., 2005; Lewis et al., 2006b; MAIDANA and YANG, 2008). Vertical transmission of disease, i.e., the transmission of the pathogen from mother to child is one of the aspects that has been taken into account in the mosquitoes population. With such a mechanism, the virus can continue to live in nature for a long time (Goddard et al., 2003; Cruz-Pacheco et al., 2005). In some models, the birth rate of bird populations is con-

sidered (Cruz-Pacheco et al., 2005) while in others, the population of birds is assumed to be constant (Wonham et al., 2004). The population of humans can also be added to models (Bowman et al., 2005; Chen et al., 2016). By taking into account the movements of birds and vectors, WNv temporal models have been extended to reaction-diffusion models. In that case, the speed of epidemic waves across an area and factors that influence it, could be determined. In recent years, most of WNv spatial models have been formulated based on two spatial models. In 2006, the initial spatial model of WNv (Lewis et al., 2006a) was presented based on the temporal model (Wonham et al., 2004), which ignored the vertical transmission of disease and assumed a constant population of birds. Considering the model proposed by Lewis et al. (2006a), the spatial dynamic of WNv has recently been investigated from some aspects, like the analysis of the spreading fronts with free boundaries (Pu et al., 2021; Cheng and Zheng, 2021). The latter (Maidana and Yang, 2009), a more complex model was proposed in 2009, which took the vertical transmission and birth rate of birds into account. The temporal dynamic of that model was studied by Cruz-Pacheco et al. (2005). They showed that the directional movements of birds play an important role in accelerating the epidemic wave speed, especially when the biting rate of mosquitoes is low. The flaw of model proposed by Lewis et al. (2006a) is that the estimated speed for low biting rates does not fall within the reported speed range in the USA (3–3.5 km/day). The underestimation of speed is then rectified in the second model (Maidana and Yang, 2009) by taking into account the directional movement of birds. All of these models assume that the random movement of birds in their home range is based on Brownian motion, resulting in an epidemic with a constant speed.

Recently, there has been increasing interest in studying different patterns of random searches performed by living organisms. In this case, empirical studies on the random movement of species have challenged Brownian motion and pointed towards the existence of Lévy flight foraging patterns for many species in their search for tar-

gets with low availability. Some examples of such species include human T cells in the brain (Harris et al., 2012), marine predators (Sims et al., 2008; Humphries et al., 2010), honeybees (Reynolds et al., 2007a,b), and albatrosses (Humphries et al., 2013). Lévy flight pattern allows species to make occasionally long steps between multiple short displacements. This is an important attitude that distinguishes it from Brownian motion, which only comprises short displacements. In the case of Lévy flights, the searching walker undertakes excursions whose length is derived from a probability distribution function (pdf) exhibiting a heavy-tailed asymptotic behaviour as $\sim |x|^{-(\alpha+1)}$, where $1 < \alpha < 2$ and $|x|$ is the displacements length while for a Brownian motion, the tails of a Normal pdf decay exponentially (Klafter and Sokolov, 2011).

Nowadays, time fractional-order dynamical systems are being studied for modelling a wide range of problems in science, engineering, and medicine. Following the identification of the Lévy flight pattern of the species movements, space fractional-order diffusion equations have been of great significance for modelling the spatial dynamics in biology and ecology (Hanert, 2012; Vallaeys et al., 2017; Farhadi and Hanert, 2022a). In epidemiology, it has also been shown that such models can well describe human epidemics propagating exponentially (Hanert et al., 2011). In recent years, time fractional-order derivative has also been applied to modelling diseases such as, West Nile virus (Sweilam et al., 2019), and HIV-infection (Jajarmi and Baleanu, 2018; Baleanu et al., 2020c).

In this work, our objective is to improve the model proposed by Lewis et al. (2006a) by introducing Lévy flights. On the one hand, Mundt et al. (2009) showed that the WNv epidemic propagated rapidly with a non-constant speed throughout North America. But, such a classical model is a second-order diffusion equation, which relies on the assumption that birds perform a Brownian motion and hence results in a constant speed for the epidemic waves. On the other hand, it could underestimate the epidemic speed for low mosquito biting and recovery rates. To address these drawbacks, we propose a tempered-space fractional-order dif-

fusion model. In recent work, we have recently shown that such fractional-order diffusion models are suitable for modelling the animal epidemics (Farhadi and Hanert, 2022b). Here, we show how symmetric truncated fractional-order diffusion operators affect the propagation pattern of WNv epidemic waves and also the epidemic speed for different values of biting rates. The paper is organized as follows. In the next section, we review the model studied by Lewis et al. (2006a). In Section 4.3, we extend the classical model to a fractional-order diffusion model. Our proposed model is numerically solved and simulation results are discussed in Section 4.4. Finally, we finish the work with conclusions in Section 4.5.

4.2 Model formulation review

In 2006, a space-time model of WNv was proposed by Lewis et al. (2006a). In that work, they first modified a temporal model of WNv derived by Wonham et al. (2004), and then obtained a simplified version of that model by making some assumptions. In that case, to study the spatial dynamics of WNv, they formulated a reaction-diffusion model relying on the Brownian motion of mosquitoes and birds by reducing the number of the model equations. In what follows, we shall review Lewis et al. (2006a) model.

The temporal model simplified by Lewis et al. (2006a) consists of the indirectly transmitted infection between the birds and mosquitoes populations whose numbers at time t are denoted by $N_b(t)$ and $N_m(t)$. The bird population is divided into three sub-populations, namely the susceptibles S_b, the infectives I_b, and the recovered class R_b while the mosquito population is divided into the susceptibles S_m and the infectives I_m sub-populations.
For the mosquito population, assuming that the birth and death rates are equal to μ leads to a constant total population size N_m of mosquitoes. Therefore, $S_m(t) + I_m(t) = N_m$. In the case of the birds, the recruitment birth rate is ignored and, since a large number of bird species have a low mortality rate for the WNv virus

(Komar et al., 2003), the death rate of the birds is assumed to be equal to 0. In that case, the total birds population has a constant size equals N_b. Therefore, $S_b(t) + I_b(t) + R_b(t) = N_b$.

The effective contact rate β_b is defined as the average number of contacts between a susceptible bird and infected mosquitoes per day, which can be given by the product $bp_{mb}N_m/N_b$, where the biting rate b is defined as the average number of bites per mosquito per day and p_{mb} is the probability of the infection transmission from mosquito to the bird. The effective contact rate β_m is defined as the average number of contacts between a susceptible mosquito and infected birds per day, which can be given by the product of the biting rate b, and the probability of the infection transmission from bird to mosquito p_{bm}. Therefore, the indirect infection rates per susceptible mosquitoes and susceptible birds, respectively, are given by:

$$\beta_m \frac{I_b}{N_b} = bp_{bm}\frac{I_b}{N_b}, \qquad \beta_b \frac{I_m}{N_m} = bp_{mb}\frac{N_m}{N_b}\frac{I_m}{N_m} = bp_{mb}\frac{I_m}{N_b}. \tag{4.1}$$

The infected birds are recovered from infection at rate γ and the recovered birds lose the immunity at rate η, and then become susceptible. By considering the above assumptions and the definitions of the parameters, a schematic representation of the model can be obtained in Figure 4.1, leading to formulating a spatially homogeneous model of WNv disease as follows:

$$\frac{dS_m}{dt} = \mu N_m - bp_{bm}\frac{I_b}{N_b}S_m - \mu S_m, \tag{4.2}$$

$$\frac{dI_m}{dt} = bp_{bm}\frac{I_b}{N_b}S_m - \mu I_m, \tag{4.3}$$

$$\frac{dS_b}{dt} = -bp_{mb}\frac{I_m}{N_b}S_b + \eta R_b, \tag{4.4}$$

$$\frac{dI_b}{dt} = bp_{mb}\frac{I_m}{N_b}S_b - \gamma I_b, \tag{4.5}$$

$$\frac{dR_b}{dt} = \gamma I_b - \eta R_b, \tag{4.6}$$

By multiplying both sides of Eq. (4.6) by the integrating factor $e^{\eta t}$, its solution can be obtained in terms of $I_b(t)$ as follows:

$$\frac{d}{dt}(R_b(t)e^{\eta t}) = \gamma e^{\eta t} I_b(t). \tag{4.7}$$

By integrating with respect to t and assuming that $R_b(0) = 0$, we get

$$R_b(t) = e^{-\eta t} \int_0^t \gamma e^{\eta \tau} I_b(\tau) d\tau. \tag{4.8}$$

Since $I_b(t) < N_b$, we have the inequality $R_b(t) \leq \frac{\gamma}{\eta} N_b$. Lewis et al. (2006a) supposed that the recovered birds have no immunity to the infection and could be transmitted to the susceptibles and become infected at any time. In that case, $\eta \to \infty$. Therefore, $R_b(t) \to 0$, and we can ignore Eq. (4.6). Now by considering the relations $S_b(t) + I_b(t) = N_b$ and $S_m(t) + I_m(t) = N_m$, the 5-equation model (4.2)–(4.6) reduces to a model consisting of only the equations for infective mosquitoes and birds as follows:

$$\frac{dI_m}{dt} = bp_{bm}\frac{N_m - I_m(t)}{N_b} I_b(t) - \mu I_m(t), \tag{4.9}$$

$$\frac{dI_b}{dt} = bp_{mb}\frac{N_b - I_b(t)}{N_b} I_m(t) - \gamma I_b(t). \tag{4.10}$$

At the next step, Lewis et al. (2006a) extended the simplified temporal model (4.9) and (4.10) to a space-time model by considering the random movement of the infective mosquitoes and birds. In that case, by assuming that the mosquitoes and birds movements can be represented by a Brownian motion, the second-order diffusion operators $D_m \partial^2 I_m(x,t)/\partial x^2$, and $D_b \partial^2 I_b(x,t)/\partial x^2$ should be added to Eqs. (4.9) and (4.10), respectively, where D_m and D_b represent the diffusion coefficients with SI units of $\mathrm{m^2 s^{-1}}$. Since mosquitoes move much more slowly than birds, we have $D_m \ll D_b$, and the diffusion operator for the infectious mosquito equation can thus be ignored. In that case, one can get the final simplified version of the WNv spatially dependent model proposed by Lewis et al.

(2006a) as follows:

$$\frac{\partial I_m}{\partial t} = bp_{bm}\frac{N_m - I_m(x,t)}{N_b}I_b(x,t) - \mu I_m(x,t), \tag{4.11}$$

$$\frac{\partial I_b}{\partial t} = D_b\frac{\partial^2 I_b(x,t)}{\partial x^2} + bp_{mb}\frac{N_b - I_b(x,t)}{N_b}I_m(x,t) - \gamma I_b(x,t). \tag{4.12}$$

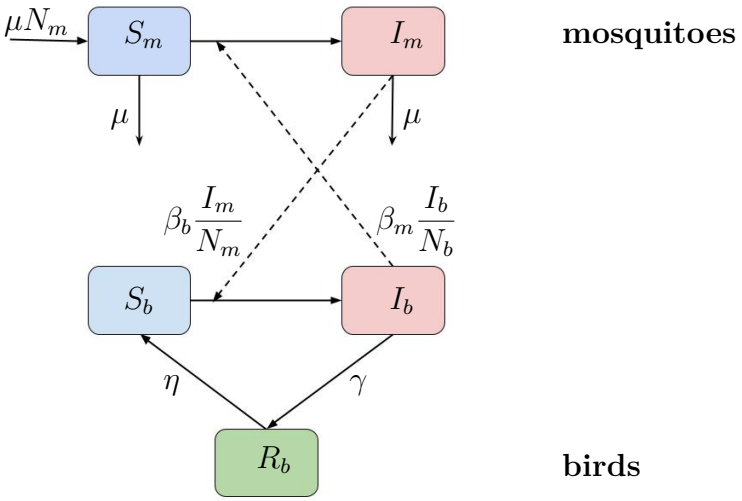

Fig. 4.1: Schematic representation of a compartment model for indirectly transmitted WNv virus between birds and mosquitoes, where S_m and I_m are the susceptible and infected mosquitoes, respectively, and S_b, I_b, and R_b are the susceptible, infected and recovered birds, respectively. The susceptibles S_m receive infection from the infectives I_b at a rate $\beta_m I_b/N_b$, and the susceptibles S_b are infected by the infectives I_m at a rate $\beta_b I_m/N_m$, where N_b and N_m are the constant total population size of birds and mosquitoes, respectively. μ is the birth and death rate of mosquitoes. The transmissions from I_b to R_b and R_b to S_b are represented by a recovery rate γ and a loss of immunity rate η, respectively.

4.3 The extended fractional modelling

The spatio-temporal model (4.11) and (4.12), as a classical model in which the random movement of the infected birds is based on a Brownian motion, has been used to calculate the propagation speed of the WNv epidemic that occurred in North America in 1999. Such a classical approach to modelling spatial dynamics results in travelling waves propagating across a domain at a constant speed. However, Mundt et al. (2009) proposed accelerating waves of the disease across North America, which cannot be obtained by the second-order diffusion models. Hanert et al. (2011) and Farhadi and Hanert (2022a) have shown that the space-fractional-order diffusion models can lead to non-constant speed of the epidemics. It thus seems reasonable to replace the second-order diffusion operator with a suitable fractional-order diffusion one. Here, we use a symmetric truncated-space fractional-order diffusion operator, which could lead to an upper bound on the epidemic speed (Farhadi and Hanert, 2022a). However, un-truncated space fractional-order diffusion models have the potential to model the epidemics propagating at exponential speed (Hanert et al., 2011).

A large number of species of wild birds can be infected with WNv and they certainly adopt different random searching patterns in their home range. Although nowadays increasing studies and experiments are being conducted to show the existence of a Lévy flight foraging pattern for biological and ecological species, there is no strong evidence of such a random movement for all wild birds. Nevertheless, among such birds, based on some experiments (Veit and Lewis, 1996) and references therein, the spread of the house finches population could be included in a combination of short movements and jumps (long movements), which shows a possibility of Lévy movements. It should be noted that the house finches are thought to be important in the transmission of WNv, as they are competent birds in the WNv dissemination such that the *Culex* mosquitoes can frequently feed upon them (Kilpatrick et al., 2007). Therefore, we assume that the infected bird displacements could be

described by a probability distribution function (pdf) that is tempered exponentially and asymptotically behaves as $\sim e^{-\lambda x}|x|^{-(\alpha+1)}$, where $1 < \alpha < 2$ is the fractional-order derivative, $|x|$ is the displacements length, and λ is called truncation parameter, whose dimension is length^{-1} and is defined by $\lambda = 1/L_{trunc}$, where until a distance of the length L_{trunc}, the tails of the pdf for displacements exhibit a power-law decay and after that has an exponential behaviour. It is worth noting that the assumption of truncated Lévy flights is closer to the fact that long movements can not be arbitrarily made by birds within their home range or territory due to environmental and physiological constraints.
Therefore, based on the above explanations, we extend the classical spatial model (4.11)–(4.12) to the following fractional-order model:

$$\frac{\partial I_m}{\partial t} = bp_{bm}\frac{N_m - I_m(x,t)}{N_b} I_b(x,t) - \mu I_m(x,t), \tag{4.13}$$

$$\frac{\partial I_b}{\partial t} = D_{b,\alpha}\mathcal{D}_x^{\alpha,\lambda} I_b(x,t) + bp_{mb}\frac{N_b - I_b(x,t)}{N_b} I_m(x,t) - \gamma I_b(x,t), \tag{4.14}$$

where

$$\mathcal{D}_x^{\alpha,\lambda} I_b(x,t) = \frac{-1}{2\cos(\alpha\pi/2)}\Big(e^{-\lambda x}\,{}_0D_x^{\alpha}(e^{\lambda x} I_b(x,t)) + e^{\lambda x}\,{}_xD_L^{\alpha}(e^{-\lambda x} I_b(x,t)) - 2\lambda^{\alpha} I_b(x,t)\Big), \tag{4.15}$$

and the parameter $D_{b,\alpha}$ denotes a fractional diffusivity with the dimension $[D_{b,\alpha}] = \text{length}^{\alpha}\text{time}^{-1}$, and ${}_0D_x^{\alpha}$ and ${}_xD_L^{\alpha}$ are the left and right Riemann-Liouville fractional derivatives on $[0, L]$, respectively defined as follows:

$${}_0D_x^{\alpha} I_b(x,t) = \frac{1}{\Gamma(n-\alpha)}\frac{\partial^n}{\partial x^n}\int_0^x \frac{I_b(\xi,t)}{(x-\xi)^{\alpha-n+1}} d\xi, \tag{4.16}$$

$${}_xD_L^{\alpha} I_b(x,t) = \frac{(-1)^n}{\Gamma(n-\alpha)}\frac{\partial^n}{\partial x^n}\int_x^L \frac{I_b(\xi,t)}{(\xi-x)^{\alpha-n+1}} d\xi, \tag{4.17}$$

where $n = 1 + [\alpha]$ such that $[\alpha]$ denotes the largest integer less than or equal to α. Here, $1 < \alpha \leq 2$. So we get $n = 2$. More details on fractional derivatives can be found in (Oldham and Spanier, 1974) and (Podlubny, 1999).
It should be noted that under some conditions, such as the ability of migrating birds to infect mosquitoes, migration, as a directional movement has been studied for its contribution to spreading the virus (Peterson et al., 2003). Mathematically, for the infected bird equation, we can consider the advection term $-c\partial I_b/\partial x$, where c is the migration velocity with units of km/day.

4.4 Simulation results and discussion

In this section, we numerically solve the fractional model Eqs. (4.13) and (4.14) by the method explained in appendix A.3. We consider a finite domain $[0, L]$, where L =700 km. Since we have defined a symmetric diffusion operator by Eq. (4.15), the epidemic waves travel to the right and left sides. So we consider a localized initial condition of the exponential form in the middle of the domain for the infected birds and assume that there are initially no infected mosquitoes throughout the domain. Moreover, we impose zero-Neumann boundary conditions on the left and right boundaries, which let the waves go out the boundaries smoothly. So, we have the initial and boundary conditions as follows:

$$I_m(x, t = 0) = 0, \qquad I_b(x, t = 0) = I_0(x) = \begin{cases} e^{-\nu(x-x_0)} & : x \geq x_0, \\ e^{\nu(x-x_0)} & : x \leq x_0, \end{cases} \tag{4.18}$$

$$\begin{aligned} \frac{\partial I_m}{\partial x}(x = 0, t) &= \frac{\partial I_m}{\partial x}(x = L, t) = 0, \\ \frac{\partial I_b}{\partial x}(x = 0, t) &= \frac{\partial I_b}{\partial x}(x = L, t) = 0, \end{aligned} \tag{4.19}$$

where $x_0 = L/2$, and $\nu = 0.8\,\mathrm{km}^{-1}$. The values of the model parameters, their definitions, and corresponding references are sum-

marized in Table 4.1 and 4.2. In the numerical examples, the total population of birds and mosquitoes are set to 20 and 400 per km, i.e., we have the ratio $N_m/N_b = 20$ as it is estimated by Lewis et al. (2006a). For all simulations, we consider a duration of 90 days and set $\alpha = 1.5$, and $c = 0$, where c is the migration velocity. Only the last example illustrates how a non-zero value of c impacts the wave speed.
In the following examples, our main purpose is to compute numerically the epidemic front speed to see how the tempered-space fractional diffusion operator affects the epidemic waves. To do so, a Lagrangian trajectory $x_L(t)$ is numerically computed such that $I_b(x_L(t), t) = I_0$, where $I_0 \approx 0$. Here, I_0 is set to 0.01. Then, the instantaneous speed is given by $v(t) = dx_L(t)/dt$.

It should be noted that since numerous bird species and some types of mosquitoes act as the reservoirs and vectors of WNv, respectively, the epidemic speed is considerably affected by the value of some parameters, such as the recovery rate of birds, and the biting rate of mosquitoes, which can change widely. By considering a zero value of the recovery rate (Work et al., 1955; Wonham et al., 2004), the average duration of infection goes to infinity. So, the number of infected birds and hence the epidemic speed increases. On the other hand, by increasing the value of recovery rates, as observed for some species of birds, such as house finch, common grackle, blue jay (Komar et al., 2003), the mean duration of infection decreases such that the wave speed decreases. In that case, the birds could transfer again to susceptible sub-populations. Here, the disease-induced death rate of birds is not considered (Wonham et al., 2004). But, it has been observed in some bird species (Komar et al., 2003). A non-zero value of that parameter leads to a decrease in the number of infected birds and hence the epidemic speed declines. Regarding the mosquito biting rates, we here considered two values $b = 0.3$ and 0.5 day^{-1}, and discussed our results for each value. For a detailed study on the wave speed sensitivity refer to Maidana and Yang (2009).

Table 4.1: Parameters of West Nile Virus model (4.13)–(4.14)

Parameters	Values	Reference
N_m	400 mosquitoes per km	(Maidana and Yang, 2009)[a]
N_b	20 birds per km	(Lewis et al., 2006a)[b]
D_b	$6\,\mathrm{km}^2\mathrm{day}^{-1}$	(Lewis et al., 2006a)
$D_{b,\alpha}$	$(2.45)^\alpha\,\mathrm{km}^\alpha\mathrm{day}^{-1}$	estimated[c]
b	0.3 and $0.5\,\mathrm{day}^{-1}$	(Maidana and Yang, 2009)
μ	$0.029\,\mathrm{day}^{-1}$	(Lewis et al., 2006a)

[a] Lewis et al. (2006a) set the ratio $N_m/N_b = 20$ and Maidana and Yang (2009) assumed 20 birds per km in their numerical examples. So, we get 400 mosquitoes per km. As another ratio, Maidana and Yang (2009) assumed the ratio 5 and 100 mosquitoes per km.

[b] Lewis et al. (2006a) set the ratio $N_m/N_b = 20$ and Maidana and Yang (2009) assumed 20 birds per km in their numerical examples. So, we get 400 mosquitoes per km. As another ratio, Maidana and Yang (2009) assumed the ratio 5 and 100 mosquitoes per km.

[c] The fractional diffusivity can be defined as $D_{b,\alpha} = \mathcal{L}^\alpha/\mathcal{T}$, where $\mathcal{L}$ is the average length of displacements with units of km over a time duration of $\mathcal{T}$ with units of day. Here, we assume that $\mathcal{L} = 2.45\,\mathrm{km}$ and $\mathcal{T} = 1\,\mathrm{day}$. In that case, the classical diffusivity D_b is obtained for $\alpha = 2$.

Table 4.2: Parameters of West Nile Virus model (4.13)–(4.14)

Parameters	Values	Reference
p_{bm}	0.16	(Lewis et al., 2006a)
p_{mb}	0.88	(Lewis et al., 2006a)
α	BM[a]: $\alpha = 2$/LF[b]: $1 < \alpha < 2$	estimated[c]
λ	PLF[d]: $\lambda = 0$/TLF[e]: $\lambda \neq 0$	estimated[f]
γ	$0.88\,\text{day}^{-1}$	(Maidana and Yang, 2009)

[a]Brownian Motion

[b]Lévy Flight

[c]Since there is no reference for the exact value of fractional order α, we consider an average value of α equals 1.5. But, we show that when α is closer to 1, the epidemic waves faster reach the steady state showing the maximum epidemic speed. However, when α is closer to 2, the epidemic waves could propagate approximately at a constant speed for a longer time until it reaches a maximum speed.

[d]Pure Lévy Flight

[e]Truncated lévy Flight

[f]Our numerical examples show that the truncation parameter is an important factor that determines the maximum value of the epidemic speed for different biting rates. Here, the value of λ is set to $0.11\,\text{km}^{-1}$ and $0.2\,\text{km}^{-1}$ for biting rates 0.3 and 0.5 day^{-1}, respectively.

In the case of a Brownian motion pattern of bird movements, by solving the model equations (4.11)–(4.12) for the biting rate $b = 0.3\,\text{day}^{-1}$, we show the spatial propagation of the infected mosquitoes and birds populations in Fig. 4.2(a) and 4.2(b), respectively.

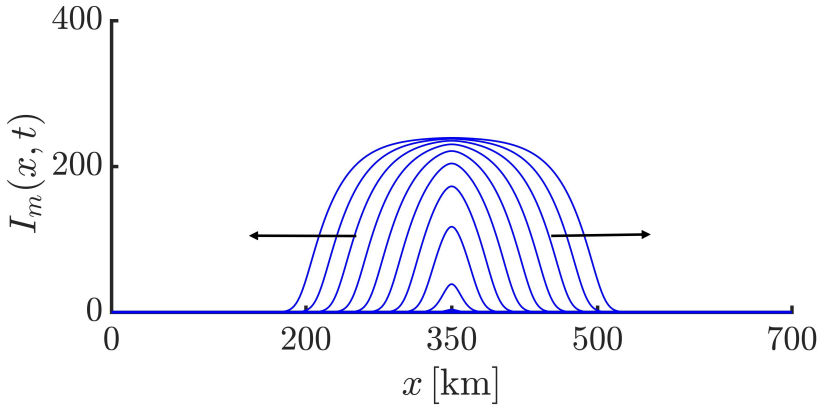

(a)

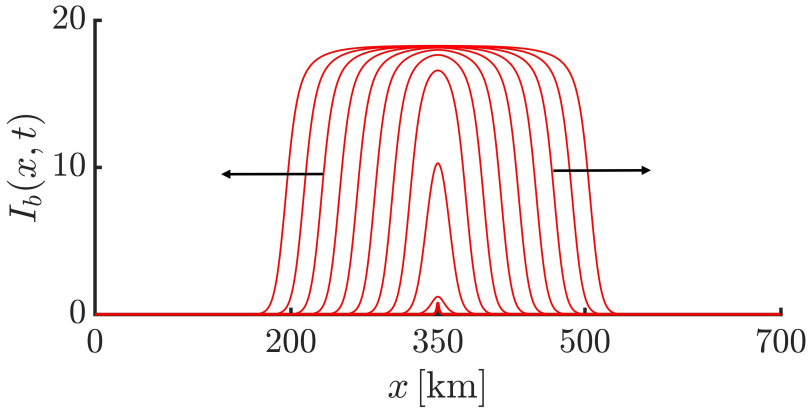

(b)

Fig. 4.2: *Cont.*

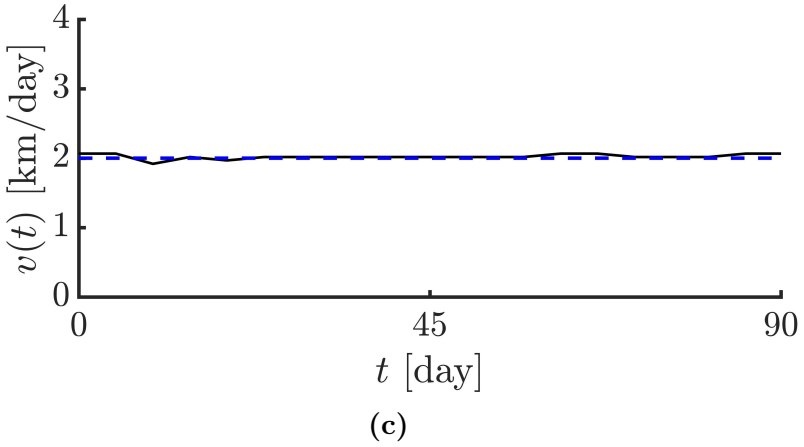

(c)

Fig. 4.2: (**a**,**b**) Wave solutions of the infected birds and mosquitoes travelling to the left and right sides at different times obtained by solving Eqs. (4.11) and (4.12), considering the biting rate $b = 0.3\,\text{day}^{-1}$. The arrows show the direction of the waves propagation. (**c**) Time evolution of the epidemic speed. The dashed line is related to the constant speed equals $\bar{v} = 2\,\text{km/day}$.

As we see both the left and right-sided waves travel at the same constant speed $v(t) \approx \bar{v} = 2\,\text{km/day}$, which is lower than the recorded epidemic speed ranging between 3–3.5 km/day (see Fig. 4.2(c)). The second-order diffusion model (4.11)–(4.12) thus underestimates the epidemic wave speed.
In order to obtain an estimation of the speed that falls within that range, we consider the nonlocal diffusion model (4.13)–(4.14) by assuming that birds follow a truncated Lévy flight with the truncation parameter $\lambda = 0.11\,\text{km}^{-1}$. Here, the value of L_{trunc} is set to 9 km. In that case, the epidemic waves initially move at an increasing speed (see Fig. 4.3(c), phase(I)), and then they travel at a constant speed showing the maximum speed $v_{max} \approx 3.2\,\text{km/day}$ (see Fig. 4.3(c), phase(II)). Here, the speed falls within the range of the observed value for the epidemic speed. In this case, the spatial

propagation of the infected mosquitoes and birds are shown in Fig. 4.3(a) and 4.3(b).

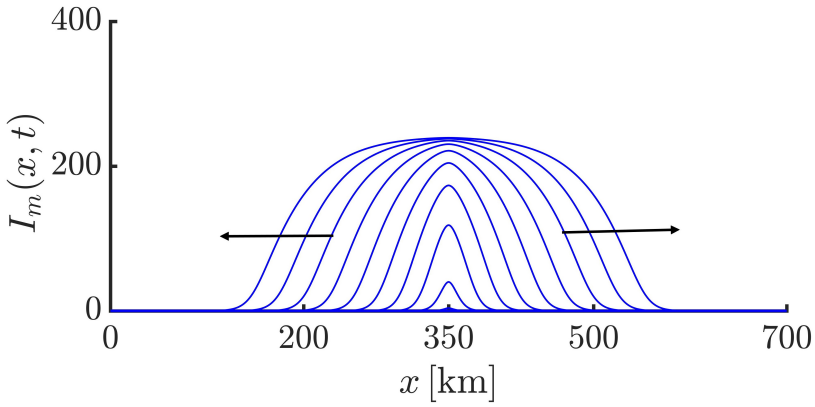

(a)

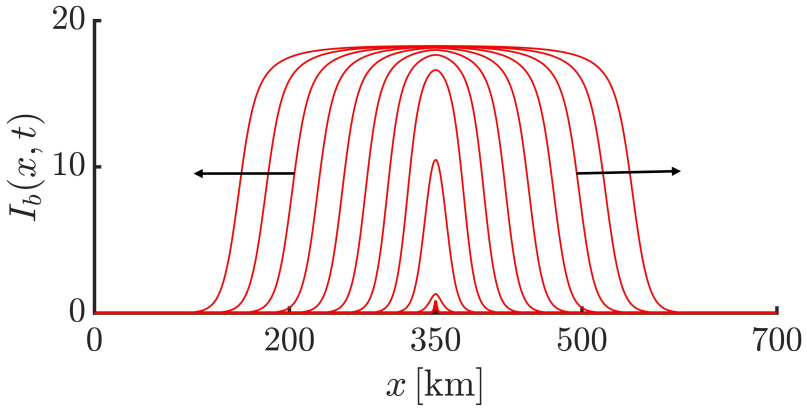

(b)

Fig. 4.3: *Cont.*

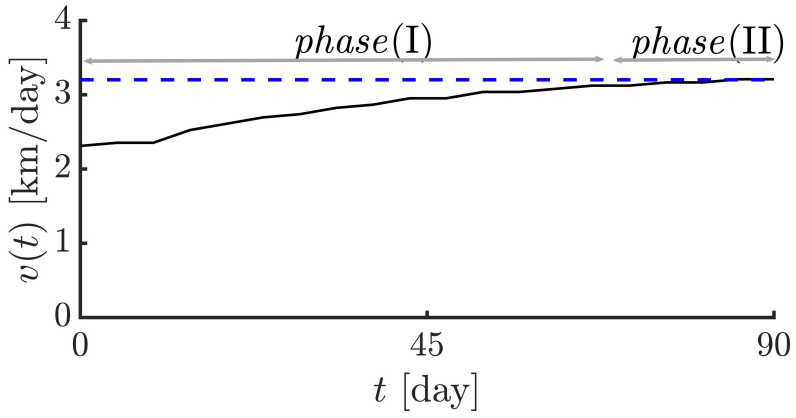

(c)

Fig. 4.3: (**a**,**b**) Wave solutions of the infected birds and mosquitoes travelling to the left and right sides at different times obtained by solving Eqs. (4.13) and (4.14), considering $\alpha = 1.5$, $\lambda = 0.11\,\mathrm{km}^{-1}$, and the biting rate $b = 0.3\,\mathrm{day}^{-1}$. The arrows show the direction of the waves propagation. (**c**) Time evolution of the epidemic speed. The dashed line is related to the maximum value of the epidemic speed equals $v_{max} \approx 3.2\,\mathrm{km/day}$. The phases (I) and (II) correspond to the accelerating and constant speed stages of the front propagation.

By increasing the value of biting rate, the density of infected birds will increase so that the epidemic front accelerates. With the assumption that birds do random movements based on a Brownian motion, for $b = 0.5\,\mathrm{day}^{-1}$, we obtain the estimated constant epidemic speed $v(t) \approx \bar{v} = 3\,\mathrm{km/day}$, which shows the lowest observed speed (see Fig. 4.4(c)). In that case, the profiles of infected mosquitoes and birds at different times are shown in Fig. 4.4(a) and 4.4(b).
For estimating the epidemic speed greater than $3\,\mathrm{km/day}$, we consider the truncated-space fractional order model (4.13)–(4.14) with the truncation parameter $\lambda = 0.2\,\mathrm{km}^{-1}$ ($L_{trunc} = 5\,\mathrm{km}$), which yields the epidemic waves that first propagate increasingly (see Fig. 4.5(c), phase(I)) and then the waves propagate at a constant speed

equals $v_{max} \approx 3.7\,\text{km/day}$ (see Fig. 4.5(c), phase(II)). The both infected waves of mosquitoes and birds at different instant times are shown in Fig. 4.5(a) and 4.5(b), respectively.

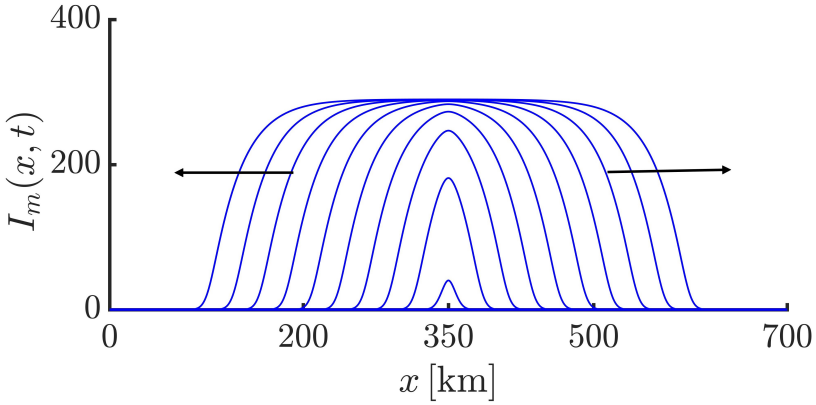

(a)

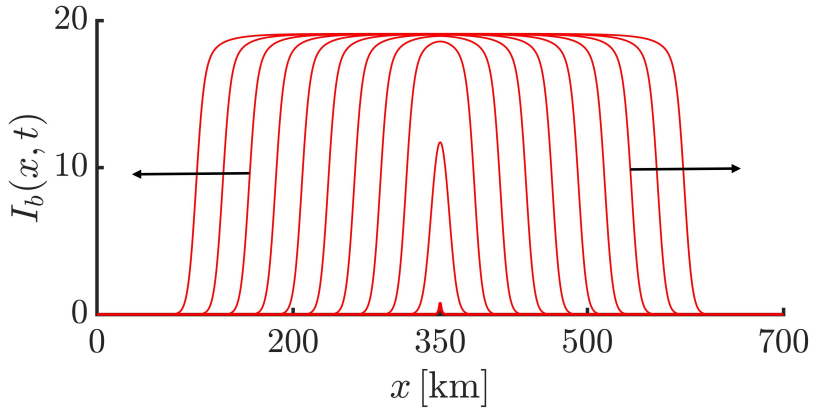

(b)

Fig. 4.4: *Cont.*

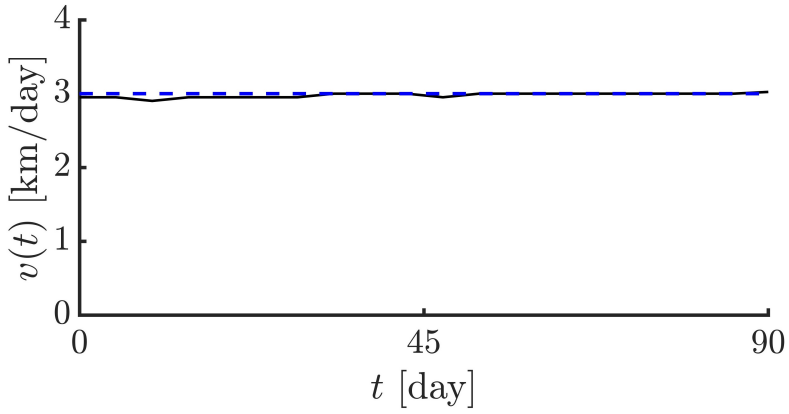

(c)

Fig. 4.4: (**a**,**b**) Wave solutions of the infected birds and mosquitoes travelling to the left and right sides at different times obtained by solving Eqs. (4.11) and (4.12), considering the biting rate $b = 0.5\,\text{day}^{-1}$. The arrows show the direction of the waves propagation. (**c**) Time evolution of the epidemic speed. The dashed line is related to the constant speed equals $\bar{v} = 3\,\text{km/day}$.

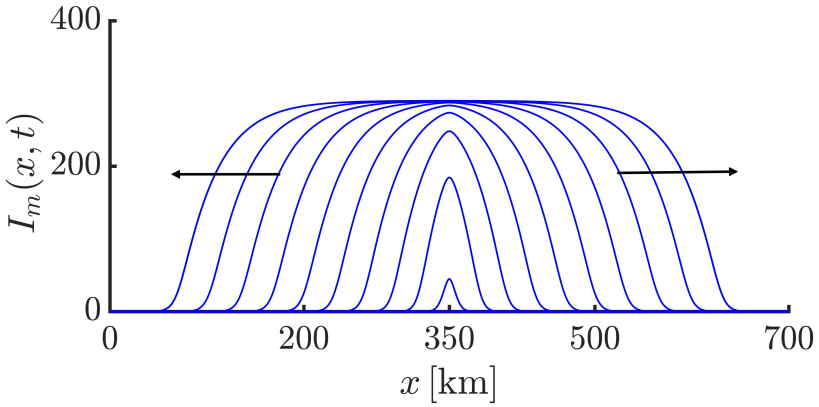

(a)

Fig. 4.5: *Cont.*

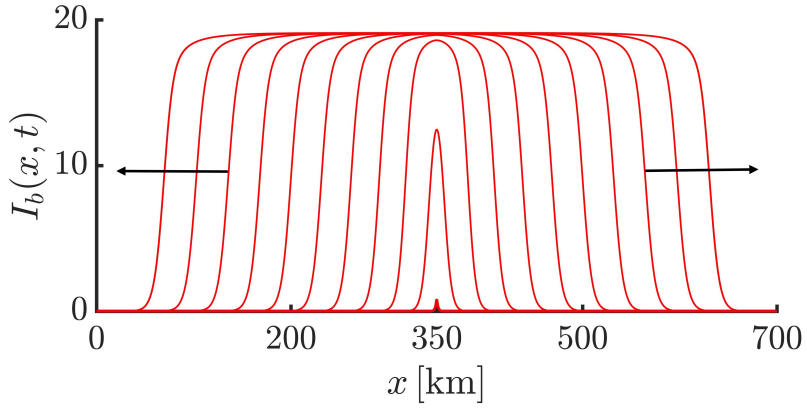

(b)

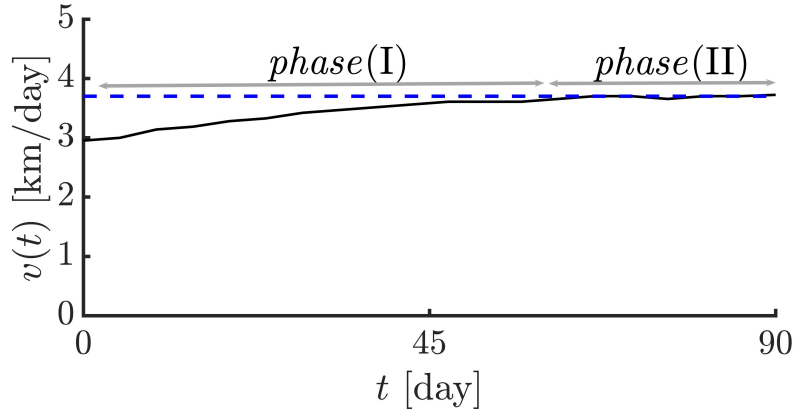

(c)

Fig. 4.5: (**a**,**b**) Wave solutions of the infected birds and mosquitoes travelling to the left and right sides at different times obtained by solving Eqs. (4.13) and (4.14), considering $\alpha = 1.5$, $\lambda = 0.2\,\mathrm{km}^{-1}$, and the biting rate $b = 0.5\,\mathrm{day}^{-1}$. The arrows show the direction of the waves propagation. (**c**) Time evolution of the epidemic speed. The dashed line is related to the maximum value of the epidemic speed equals $v_{max} \approx 3.7\,\mathrm{km/day}$. The phases (I) and (II) correspond to the accelerating and constant speed stages of the front propagation.

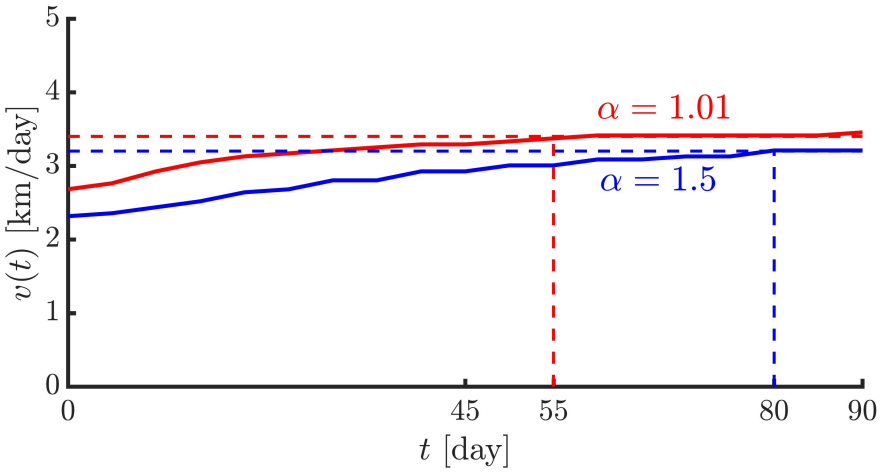

Fig. 4.6: Comparison between the time evolution of the epidemic speed obtained by two different values of the fractional-order α, i.e., $\alpha = 1.5$ and $\alpha = 1.01$. The biting rate and the truncation parameter are set to $b = 0.3\,\text{day}^{-1}$ and $\lambda = 0.11\,\text{km}^{-1}$, respectively. For $\alpha = 1.01$, the epidemic waves reach the constant speed $v_{max} \approx 3.4\,\text{km/day}$ at time 55 days. However, for $\alpha = 1.5$, the constant speed $v_{max} \approx 3.2\,\text{km/day}$ at time 80 days is obtained. Highlighting the importance of the fractional-order α in the time evolution of the epidemic speed.

Fig. 4.6 shows the difference between the time evolution of the epidemic speed in the cases of $\alpha = 1.01$ and $\alpha = 1.5$. Here, we set the same values of $\lambda = 0.11\,\text{km}^{-1}$ and $b = 0.3\,\text{day}^{-1}$. As we see, when the fractional-order α is closer to 1, the epidemic waves propagate more quickly so that they reach the maximum speed within a shorter time compared to values of α closer to 2.

It is worth noting that based on our simulation results, for different biting rates, the value of truncation parameter should vary so that an appropriate estimation of the epidemic speed could be achieved. For each biting rate, different values of truncation parameter can also be considered. In that case, values of λ can lead to either underestimating or overestimating the epidemic speed. But, we can estimate a domain of λ values such that the obtained

epidemic speed can fall within the range of observed speed. For instance, for $b = 0.3\,\text{day}^{-1}$ and $\lambda = 0.11\,\text{km}^{-1}$, we get $v_{max} \approx 3.2\,\text{km/day}$. Now, if we set $L_{trunc} = 11\,\text{km}$ ($\lambda = 0.09\,\text{km}^{-1}$) then the maximum epidemic will increase, i.e., $v_{max} \approx 3.7\,\text{km/day}$. However, if L_{trunc} is set to $7\,\text{km}$ ($\lambda = 0.14\,\text{km}^{-1}$) then the epidemic speed is underestimated as $v_{max} \approx 2.6\,\text{km/day}$. Therefore, for $b = 0.3\,\text{day}^{-1}$, we can approximately estimate the values between $8\,\text{km}$ and $10\,\text{km}$ for L_{trunc} such that the obtained epidemic speed varies in the range of (3–3.5 km/day).

The final example illustrates the impact of the migration velocity on the epidemic propagation. In this case, for migrating birds, a preferential direction to the left is considered. Here, we assume that $c = -1\,\text{km/day}$ as considered by Maidana and Yang (2009) in their numerical examples, $\alpha = 1.5$, $b = 0.3\,\text{day}^{-1}$, and $\lambda = 0.11\,\text{km}^{-1}$.

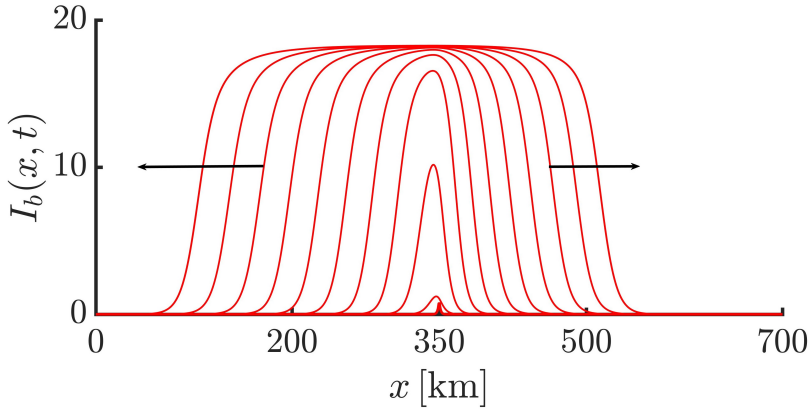

(a)

Fig. 4.7: *Cont.*

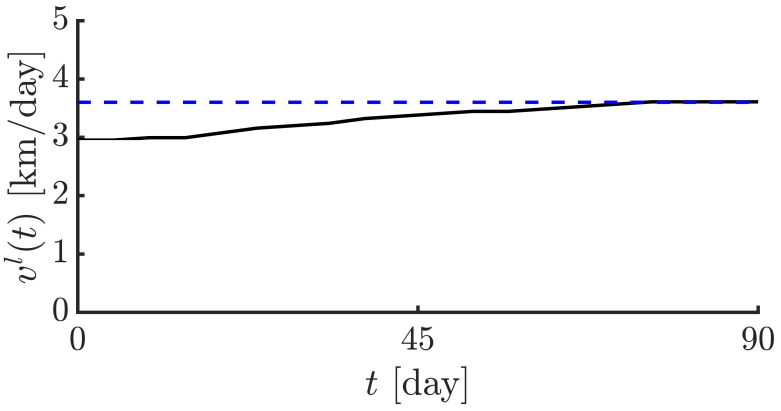

(b)

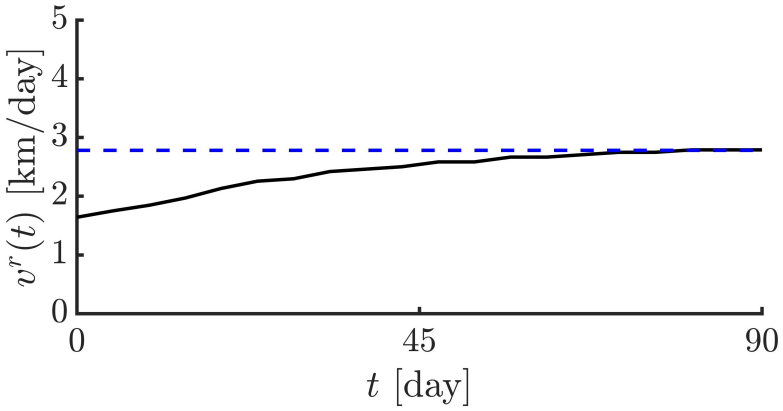

(c)

Fig. 4.7: (**a**) Asymmetrical wave solutions of the infected birds to the left and right sides at different times obtained by solving the model (4.13)–(4.14), considering $\alpha = 1.5$, $\lambda = 0.11\,\mathrm{km}^{-1}$, $b = 0.3\,\mathrm{day}^{-1}$, and $c = -1\,\mathrm{km/day}$. The arrows show the direction of the waves propagation. (**b**,**c**) Time evolution of the epidemic speed for the left- and right-moving waves. The dashed line is related to the constant speeds equal $\bar{v}^l_{max} \approx 3.6\,\mathrm{km/day}$ and $\bar{v}^r_{max} \approx 2.78\,\mathrm{km/day}$, for the left- and right-moving waves, respectively.

Fig. 4.7(a) shows that the left- and right-moving waves are not symmetric so that epidemic waves travel to the left more quickly than those moving to the right. Therefore, the left-propagating waves initially accelerate and then moving at a constant speed $\bar{v}^l_{max} \approx 3.6\,\text{km/day}$ (see Fig. 4.7(b)). However, the right-propagating waves are greatly decelerated so that they propagate at a maximum constant speed $\bar{v}^r_{max} \approx 2.78\,\text{km/day}$ (see Fig. 4.7(c)).

4.5 Conclusion

In this paper, we have proposed a tempered space fractional-order diffusion model based on the spatial model formulated by Lewis et al. (2006a) for the West Nile virus epidemic. Our model incorporates the anomalous diffusion process that occurs as a result of the Lévy movements assumption of the infected wild birds when doing random searches, especially for scarce resources in their home range. By numerically solving the model equations, we have performed a comparison of the epidemic speed estimated by the classical and fractional-order models. Maidana and Yang (2009) showed that if we consider an average value of parameters corresponding to birds species, such as common grackle, and blue jay, then the estimated speed by the model proposed by Lewis et al. (2006a) does not match that observed in the field data. Indeed, the classical model based on the Brownian motion assumption generates the epidemic waves moving at a constant speed, which might be less than the range of observed epidemic speed. However, we showed that the estimated wave speed by our model could fall within that range. That is, the truncated fractional-order diffusion model initially leads to the waves accelerating so that the epidemic could reach a maximum speed, which is consistent with the range of observed speed. It should be noted that tuning the value of the model parameters can modify the speed and hence by considering a classical model, we can also get the correct epidemic speed. But what generally differentiates classical and truncated-fractional-order models is the

fact that our model relying on a truncated Lévy flight assumption generates non-constant travelling waves (accelerating waves of the epidemic), which are shown in Mundt et al. (2009).

Furthermore, we have shown that the values of the fractional-order, truncation parameter, and migration velocity are important factors that can affect the epidemic speed and the pattern of the waves propagation. Different values of the truncation parameter are required for different biting rates to explain the real speed reported in the field data. The fractional-order affects the time to reach the maximum speed. For values closer to 1, the epidemic waves travel more quickly than the values closer to 2. The preferential movement of birds to the left leads to generating waves that travel to the left at a speed higher than those moving to the right side.

In the case of directly transmitted infectious diseases, Farhadi and Hanert (2022b) also derived analytical results for a truncated fractional-order epidemic model. For indirectly transmitted epidemics, like West Nile virus, as more complex models our results were obtained by numerical methods. Our numerical simulations propose that the same results of the work by Farhadi and Hanert (2022b), are still valid. That is, truncation parameter is an important factor that influences the epidemic speed and can lead to different propagation patterns of epidemic.

CHAPTER 5

Conclusions and perspectives

This chapter will conclude the study by reviewing the major research findings in relation to the research goals and questions, as well as discussing their value and contribution. It will also make suggestions for further research.

Summary of key findings

Today, after more than three centuries, Leibniz's prediction of the benefits of fractional derivatives has come true so that fractional calculus has received increasing attention in recent years and its applications have covered a wide range of different issues in engineering and science. As a part of these developments, throughout this thesis, our main objective was to apply fractional-order diffusion models to life-science problems in the fields of immunology and epidemiology. Our proposed model equations were driven by the observation that living species do not always perform random displacements that can be approximated by a Brownian motion.

Instead, Lévy flight displacement patterns often provide a more realistic picture of their displacements. In this thesis, we showed how the type of random movements of living species influences the elimination of infection in the body by the immune system and the speed of epidemics propagation in an area.

At first, we discussed the elimination speed of infected brain cells during T. gondii infection by considering different patterns of $CD8^+$ T cell random movements. In Chapter 2, our simulations demonstrated that the effectiveness of the immune system is enhanced when $CD8^+$ T cells move super-diffusively in the brain. Indeed, while doing their protective mechanisms, in comparison to Brownian motion, with a Lévy flight searching, T cells make long jumps between many short movements so that the whole brain tissue can be scanned during infection, and they spread more quickly throughout the brain tissue, leading to a rapid decrease of tissue cysts distributed throughout the brain. In the case of a Lévy flight, the infected cells distributed over the whole brain even those located far away from the source of T cells could be killed while in the case of a Brownian motion, the elimination speed of infected cells is much slower so that it takes a long time to kill the infected cells distributed throughout the brain tissue. Therefore, during infection, the spatial dynamic and elimination speed of infected cells are dependent on the type of random movement of T cells.

Nowadays, mathematical models about the immune system are focused on time-fractional-order and/or second-order diffusion models. However, our new results can illuminate our understanding of how the immune system can get benefit from the LF foraging pattern of T cells in response to infection. This work paves the way to further scientific investigations around the advantages of the LF searching mechanism for the immune system in other tissues, like lymph nodes. Fricke et al. (2016) showed that the movement of inactive (naïve) T cells within lymph nodes are super-diffusive. Thus, this will allow us to study the efficiency of T cells at finding antigen-presenting cells (APCs) in lymph nodes by deriving space-fractional-order models and using the same strategy by comparing

the obtained results to a classical model relying on the second-order diffusion models.

In the context of epidemiology, the propagation speed of epidemics has been widely studied based on the assumption that infected hosts move in a diffusive fashion (Brownian motion). In a few studies, by assuming that the random movement of infected hosts is described by a pure Lévy flight, the epidemic speed was also studied. However, in this study, a space-fractional-order diffusion epidemic model is developed by assuming that the random movement of infected hosts is described by a truncated Lévy flight. Therefore, in Chapter 3, we considered a simple epidemic caused by direct transmission of infection. Our numerical and analytical results well confirmed that different values of the truncation parameter could lead to various types of epidemics spread. For small values of truncation parameter $\gtrsim 0$, the propagation speed of an epidemic is exponential and the solution tails have a power-law asymptotic behaviour. Increasing the value of the truncation parameter causes the epidemic propagation gets smoother so that it leads to either a gradual increase of the epidemic speed, which finally becomes constant or a constant speed like classical models. Then, we suggested that the truncated space-fractional-order diffusion models can be applied to modelling animal epidemics as they can be propagated more smoothly than human epidemics. Chapter 4 was thus concerned with a real problem. In that case, we considered the West Nile virus epidemic propagated at a non-constant speed across the USA in 1999. In this study, we extended a classical model by assuming that the random movement of infected birds in their home range can be described by a truncated Lévy flight. We showed that our proposed model could estimate the epidemic speed, which falls within the observed speed range while a space-fractional-order diffusion model with zero value of the truncation parameter and a second-order diffusion model overestimate and underestimate the epidemic speed, respectively.

In this study, an application of the exponentially truncated space-fractional-order diffusion operator was investigated for epi-

demiological problems. More broadly, we expect that one can apply such an operator to other biological reaction-diffusion systems since the truncated Lévy flight pattern of random movements is a more relevant model for describing limited/bounded biological systems. For instance, as mentioned above, for modelling the random movement of naïve T cells in lymph nodes, we can thus consider truncated space-fractional-order diffusion operators, which could provide a better estimation of T cells efficiency at finding APCs compared to pure Lévy flight and Brownian motion. As another example, we can refer to the work by Huda et al. (2018) who analysed the movement patterns of non-metastatic versus metastatic cancer cells. They showed that the probability distribution function for metastatic cell displacements well exhibits a truncated power-law with an exponent between $2.22 - 2.99$ for different types of metastatic cancer cells. Nowadays, mathematical modelling in the field of cancer has made significant progress. By considering such classical models, we can extend them to a fractional-order model by assuming that tumour cells move by a truncated Lévy flight. Indeed, the second-order diffusion term can be replaced by a symmetric truncated fractional-order diffusion operator. In that case, we can compare our numerical results with the classical model. Therefore, by considering such studies, the effect of the Lévy flight pattern on the spread of cancer cells to adjacent tissues can be compared with the Brownian motion assumption.

Overall, in this study, our strategy to quantify the improvements our proposed fractional-order models brought was to compare our results to classical Brownian models by numerically solving those equations. We concluded that space-fractional-order diffusion equations are powerful tools that can be used to well understand the effect of Lévy movements on the temporal evolution of quantities in complex systems, such as the number of infected cells in the brain and the speed of an epidemic, which were examined in this work because second-order models ignore the effect of the main feature of Lévy movements, i.e., long jumps between many short displacements. Thus, making a comparison between the results

of the second-order and fractional-order diffusion models can be a useful strategy for studying other problems in population dynamics that are characterized by a power-law asymptotic behaviour.

Perspectives

All the fractional-order diffusion models used in biology and other fields such as ecology and finance have been proposed over the last 15 years and have not been studied extensively. While classical diffusion models have been used in those fields for more than 40 years, the fractional-order versions are much more recent. This means that many aspects of these models still need to be developed or further studied. In particular, all the models throughout this thesis were derived and used only in one spatial dimension. Higher dimensions have not been considered mostly because of the complexity of multi-dimensional formulations and the computational cost to compute a numerical approximation. This is a serious knowledge gap as most realistic problems in biology, are inherently multi-dimensional. For instance, one might be interested to study the dispersal of $CD8^+$ T cells during T. gondii infection over a realistic domain of the brain tissue and not only in one dimension as we did in Chapter 2. Therefore, the next future goal would be to address this knowledge gap by deriving a 2D and 3D space-fractional-order diffusion model.

We suggest that at first, one can review all multi-dimensional models that have been proposed, compare the mathematical properties of their solutions (existence, uniqueness, regularity) and evaluate their adequacy for the applications would be considered, then the numerical methods that have been designed for the 1D fractional diffusion equation (see for instance (Hanert, 2011; Hanert and Piret, 2014)) should be extended to the 2D equation. Here, the main challenge will be to derive a numerical scheme whose computational cost remains reasonable. Once the mathematical and numerical aspects will have been solved, the next objective will be to apply the 2D and 3D fractional diffusion models to realistic

problems, like fractional modelling of T cells in the brain.

APPENDIX A

Appendices

A.1 Fractional Neumann boundary conditions

One of the delicate issues in the field of modelling using fractional diffusion equations is to apply appropriate boundary conditions to the models on bounded domains. One of the boundary conditions is Neumann (no-flux), which contains the first-order derivatives with respect to space on the boundaries of the domain. They are also known as classical Neumann boundary conditions. In Chapter 2, since our goal is to perform a comparison between the results of Lévy and Brownian RWs, the total number of $CD8^+$ T cells entering the domain at time t should be the same in both cases. In other words, the issue of mass conservation should be guaranteed. In the case of Brownian RW, it can be done by using classical Neumann boundary conditions. However, they do not guarantee mass conservation for diffusion equations related to a Lévy RW, i.e., space-fractional-order diffusion equations. Thus, we have used the following fractional Neumann boundary conditions proposed by

Kelly et al. (2019):

$$\frac{1-\beta}{2}\,{}_0^C D_x^{\alpha-1} E(x,t) = \frac{1+\beta}{2}\,{}_x^C D_L^{\alpha-1} E(x,t),$$

for all $t \geq 0$ at positions $x = 0$ and $x = L$ and the fractional derivatives of order $\alpha - 1$ are in the Caputo sense defined in Eqs. (2.7) and (2.8). In the numerical examples, the following boundary conditions in the symmetric case, i.e., when $\beta = 0$ have been considered:

$${}_0^C D_x^{\alpha-1} E(x,t) = {}_x^C D_L^{\alpha-1} E(x,t),$$

for all $t \geq 0$ at positions $x = 0$ and $x = L$.

A.2 Numerical discretization of T. gondii model

In this section, we shall illustrate the discretization of the T. gondii model equations by the finite-element scheme. To do this, we approximate the exact solutions of the model equations by the following expansions in terms of basis functions $\phi_j(x)$:

$$S(x,t) \approx \tilde{S}(x,t) = \sum_{j=1}^{N} s_j(t)\phi_j(x), \quad I_1(x,t) \approx \tilde{I}_1(x,t) = \sum_{j=1}^{N} a_j(t)\phi_j(x),$$

$$I_2(x,t) \approx \tilde{I}_2(x,t) = \sum_{j=1}^{N} c_j(t)\phi_j(x), \quad E(x,t) \approx \tilde{E}(x,t) = \sum_{j=1}^{N} e_j(t)\phi_j(x),$$

where s_j, a_j, c_j and e_j are unknown nodal values. With the same method in Section 2.4, the resulting discrete Eqs. (2.9)–(2.11) then read:

$$\begin{aligned}
M_{ij}s_j'(t) &= -\theta R_{ijk} s_j(t) a_k(t), \\
M_{ij}a_j'(t) &= \theta R_{ijk} h_j(t) a_k(t) - (\beta + d_1) M_{ij} a_j(t), \\
M_{ij}c_j'(t) &= \beta M_{ij} a_j(t) - p R_{ijk} c_j(t) e_k(t) - d_2 M_{ij} c_j(t),
\end{aligned}$$

where

$$M_{ij} = \int_0^L \phi_i \phi_j dx, \qquad R_{ijk} = \int_0^L \phi_i \phi_j \phi_k dx,$$

for $i, j, k = 1, ..., N$. Here, our aim is to find possible values of the coefficients R_{ijk}. First, We consider a fixed index $i \in \{2, ..., N-1\}$. So, there are only the three possible values of $j : i-1, i$ and $i+1$. Because for $j = i-1, i, i+1$, there are intervals $J_{i-1} = (x_{i-1}, x_i), J_i = (x_{i-1}, x_{i+1})$ and $J_{i+1} = (x_i, x_{i+1})$ such that for any $x \in J_j$, we have $\phi_i(x)\phi_j(x) \neq 0$. Now, for these values of j, we determine the possible values of index k such that $\phi_i(x)\phi_j(x)\phi_k(x) \neq 0$ for any $x \in J_j$. Here, we have three cases. (1) for $j = i-1$, by considering the two possible values of index $k = i-1, i$, we have $\phi_i(x)\phi_j(x)\phi_k(x) \neq 0$ for any $x \in J_{i-1}$. (2) for $j = i$, by considering the three possible values of index $k = i-1, i, i+1$, we have $\phi_i(x)\phi_j(x)\phi_k(x) \neq 0$ for any $x \in J_i$, and (3) for $j = i+1$, the only possible values of index k are i and $i+1$ such that for any $x \in J_{i+1}$, we get $\phi_i(x)\phi_j(x)\phi_k(x) \neq 0$. Therefore, we get the following nonzero values of the coefficients R_{ijk}:

$$R_{i,i-1,i-1}, \quad R_{i,i-1,i}, \quad R_{i,i,i-1}, \quad R_{i,i,i}, \quad R_{i,i,i+1}, \quad R_{i,i+1,i}, \quad R_{i,i+1,i+1}.$$

For $i = 1$, the coefficients $R_{1,1,1}, R_{1,1,2}, R_{1,2,1}$ and $R_{1,2,2}$, and finally for $i = N$, the coefficients $R_{N,N-1,N-1}, R_{N,N-1,N}, R_{N,N,N-1}$ and $R_{N,N,N}$ have nonzero values. After some calculation, we can express the nonzero values R_{ijk} in terms of M_{ij} as follows:

$$R_{1,1,1} = \frac{3}{4} M_{1,1}, \quad R_{1,1,2} = R_{1,2,1} = R_{1,2,2} = \frac{1}{2} M_{1,2},$$

for $i = 2, ..., N-1$,

$$\begin{aligned} R_{i,i,i} &= \frac{3}{4} M_{i,i}, \quad R_{i,i-1,i-1} = R_{i,i-1,i} = R_{i,i,i-1} = \frac{1}{2} M_{i,i-1}, \\ R_{i,i,i+1} &= R_{i,i+1,i} = R_{i,i+1,i+1} = \frac{1}{2} M_{i,i+1}, \end{aligned}$$

and finally,

$$R_{N,N,N} = \frac{3}{4} M_{N,N}, \quad R_{N,N-1,N-1} = R_{N,N-1,N} = R_{N,N,N-1} = \frac{1}{2} M_{N,N-1}.$$

A.3 Numerical discretization of the West Nile virus model

In order to numerically solve Eqs. (4.13) and (4.14), based on a Galerkin formulation, we use a finite-element method that used by Vallaeys et al. (2017). To explain that scheme with more details, we consider the following reaction-advection-diffusion equation:

$$\frac{\partial I_b}{\partial t} = D_{b,\alpha}\mathcal{D}_x^{\alpha,\lambda} I_b(x,t) - c\frac{\partial I_b}{\partial x} - \gamma I_b(x,t), \tag{A.1}$$

where the parameters $D_{b,\alpha}$, c, and γ and the operator $\mathcal{D}_x^{\alpha,\lambda}$ are defined in Section 4.3. First, we express the unknown solution $I_b(x,t)$ as a sum of basis functions $\phi_j(x)$ and the unknown coefficients $b_j(t)$:

$$I_b(x,t) \approx \tilde{I}_b(x,t) = \sum_{j=1}^{N} b_j(t)\phi_j(x). \tag{A.2}$$

Then we divide the interval $[0, L]$ into $N-1$ subintervals $[x_j, x_{j+1}]$ whose lengths are equal to h, i.e., $x_1 = 0, x_N = L$, and $x_{j+1} - x_j = h$ for $j = 1, \ldots, N-1$ so that the piecewise linear basis functions $\phi_j(x)$ for $j = 1, 2, \ldots, N$ are defined as follows:

$$\phi_1(x) = \begin{cases} \dfrac{x_2 - x}{x_2 - x_1} & : x_1 \le x \le x_2, \\ 0 & : x \notin [x_1, x_2]. \end{cases}$$

for $j = 2, \ldots, N-1$,

$$\phi_j(x) = \begin{cases} \dfrac{x - x_{j-1}}{x_j - x_{j-1}} & : x_{j-1} \le x \le x_j, \\ \dfrac{x_{j+1} - x}{x_{j+1} - x_j} & : x_j \le x \le x_{j+1}, \\ 0 & : x \notin [x_{j-1}, x_{j+1}]. \end{cases}$$

and for $j = N$,

$$\phi_N(x) = \begin{cases} \dfrac{x - x_{N-1}}{x_N - x_{N-1}} & : x_{N-1} \le x \le x_N, \\ 0 & : x \notin [x_{N-1}, x_N]. \end{cases}$$

The left and right exponentially tempered unknown solutions, i.e., $e^{\lambda x} I_b(x,t)$ and $e^{-\lambda x} I_b(x,t)$ are also discretized, respectively as follows:

$$e^{\lambda x} I_b(x,t) \approx \tilde{I}_b^l(x,t) = \sum_{j=1}^{N} b_j^l(t)\phi_j(x). \tag{A.3}$$

and

$$e^{-\lambda x} I_b(x,t) \approx \tilde{I}_b^r(x,t) = \sum_{j=1}^{N} b_j^r(t)\phi_j(x). \tag{A.4}$$

where $b_j^l(t)$ and $b_j^r(t)$ are the unknown coefficients corresponding to the left and right tempered solutions, respectively.

By replacing $\tilde{I}_b(x,t)$, $\tilde{I}_b{}^l(x,t)$, and $\tilde{I}_b{}^r(x,t)$ in Eq. (A.1), using a Galerkin formulation, and then orthogonalizing the discrete equation with respect to all ϕ_j, we get the following equation:

$$\begin{aligned}\left(\int_0^L \phi_i\phi_j dx\right)\frac{db_j}{dt}(t) = \frac{-D_{b,\alpha}}{2\cos(\alpha\pi/2)}\Bigg(&\left(\int_0^L \phi_i e^{-\lambda x}\,{}_0D_x^\alpha\phi_j dx\right) b_j^l(t)\\ &+\left(\int_0^L \phi_i e^{\lambda x}\,{}_xD_L^\alpha\phi_j dx\right) b_j^r(t)\Bigg)\\ &- c\left(\int_0^L \phi_i\frac{d\phi_j}{dx}dx\right) b_j(t)\\ &+\frac{\lambda^\alpha D_{b,\alpha}}{\cos(\alpha\pi/2)}\left(\int_0^L \phi_i\phi_j dx\right) b_j(t)\\ &-\gamma\left(\int_0^L \phi_i\phi_j dx\right) b_j(t),\end{aligned}$$

for $i,j = 1,\ldots,N$.

Now by defining the following matrices

$$\mathbf{M} := \int_0^L \phi_i\phi_j dx, \quad \mathbf{D} := \int_0^L \phi_i(d\phi_j/dx)dx,$$

$$\mathbf{D^l} := \int_0^L \phi_i e^{-\lambda x}\,{}_0D_x^\alpha\phi_j dx, \quad \mathbf{D^r} := \int_0^L \phi_i e^{\lambda x}\,{}_xD_L^\alpha\phi_j dx,$$

the following semi-discrete equation in a matrix form is obtained:

$$\begin{aligned}\mathbf{M}\frac{d\mathbf{b}}{dt}(t) &= \frac{-D_{b,\alpha}}{2\cos(\alpha\pi/2)}\Big(\mathbf{D^l}\mathbf{b}^l(t)+\mathbf{D^r}\mathbf{b}^r(t)\Big)\\ &+ \left(\left(\frac{\lambda^\alpha D_{b,\alpha}}{\cos(\alpha\pi/2)}-\gamma\right)\mathbf{M}-c\mathbf{D}\right)\mathbf{b}(t), \qquad \text{(A.5)}\end{aligned}$$

where the vectors $\mathbf{b}(t)=[b_1(t)\ \dots\ b_N(t)]^T$, $\mathbf{b}^l(t)=\left[b_1^l(t)\ \dots\ b_N^l(t)\right]^T$, and $\mathbf{b}^r(t)=[b_1^r(t)\ \dots\ b_N^r(t)]^T$ consist of the unknown coefficients at time t. For solving Eq. (A.5), we need to compute the vectors $\mathbf{b}^l(t)$ and $\mathbf{b}^r(t)$ in terms of the vector $\mathbf{b}(t)$. To do this, we applying a Galerkin formulation to Eqs. (A.2) – (A.4) as follows:

$$\begin{aligned}\int_0^L \phi_i e^{\lambda x}\tilde{I}_b dx=\int_0^L \phi_i \tilde{I}_b{}^l dx &\longrightarrow \left(\int_0^L \phi_i e^{\lambda x}\phi_j dx\right)b_j(t)\\ &=\left(\int_0^L \phi_i\phi_j dx\right)b_j^l(t).\end{aligned}$$

and

$$\begin{aligned}\int_0^L \phi_i e^{-\lambda x}\tilde{I}_b dx=\int_0^L \phi_i \tilde{I}_b{}^r dx &\longrightarrow \left(\int_0^L \phi_i e^{-\lambda x}\phi_j dx\right)b_j(t)\\ &=\left(\int_0^L \phi_i\phi_j dx\right)b_j^r(t).\end{aligned}$$

By introducing the matrices

$$\mathbf{W^l}:=\int_0^L \phi_i e^{\lambda x}\phi_j dx, \qquad \mathbf{W^r}:=\int_0^L \phi_i e^{-\lambda x}\phi_j dx,$$

we get $\mathbf{b}^l(t)=\mathbf{M}^{-1}\mathbf{W^l}\mathbf{b}(t)$, and $\mathbf{b}^r(t)=\mathbf{M}^{-1}\mathbf{W^r}\mathbf{b}(t)$. Eq. (A.5) can thus be expressed in the following form

$$\begin{aligned}\mathbf{M}\frac{d\mathbf{b}}{dt}(t) =&\left(\frac{-D_{b,\alpha}}{2\cos(\alpha\pi/2)}\Big(\mathbf{D^l}\mathbf{M}^{-1}\mathbf{W^l}+\mathbf{D^r}\mathbf{M}^{-1}\mathbf{W^r}\Big)\right.\\ &\left.+\left(\frac{\lambda^\alpha D_{b,\alpha}}{\cos(\alpha\pi/2)}-\gamma\right)\mathbf{M}-c\mathbf{D}\right)\mathbf{b}(t), \qquad \text{(A.6)}\end{aligned}$$

Finally, by using a third-order Adams–Bashforth method, we can discretize Eq. A.6 in order to obtain the coefficients b_j defining the model solution at the current time.

Bibliography

Ali, K.K., Osman, M.S., Baskonus, H.M., Elazabb, N.S., İlhan, E., 2020. Analytical and numerical study of the HIV-1 infection of $CD4^+$ T-cells conformable fractional mathematical model that causes acquired immunodeficiency syndrome with the effect of antiviral drug therapy. Mathematical Methods in the Applied Sciences .

Anderson, A.R., Chaplain, M.A., Newman, E.L., Steele, R.J., Thompson, A.M., 2000. Mathematical modelling of tumour invasion and metastasis. Computational and mathematical methods in medicine 2, 129–154.

Ariotti, S., Beltman, J.B., Borsje, R., Hoekstra, M.E., Halford, W.P., Haanen, J.B., de Boer, R.J., Schumacher, T.N., 2015. Subtle CXCR3-dependent chemotaxis of CTLs within infected tissue allows efficient target localization. The Journal of Immunology 195, 5285–5295.

Atkinson, R., Rhodes, C., Macdonald, D., Anderson, R., 2002. Scale-free dynamics in the movement patterns of jackals. Oikos 98, 134–140.

Baeumer, B., Meerschaert, M.M., 2010. Tempered stable lévy motion and transient super-diffusion. Journal of Computational and Applied Mathematics 233, 2438–2448.

Baleanu, D., Ghanbari, B., Asad, J.H., Jajarmi, A., Pirouz, H.M., 2020a. Planar system-masses in an equilateral triangle: numerical study within fractional calculus .

Baleanu, D., Jajarmi, A., Sajjadi, S.S., Asad, J.H., 2020b. The fractional features of a harmonic oscillator with position-dependent mass. Communications in Theoretical Physics 72, 055002.

Baleanu, D., Mohammadi, H., Rezapour, S., 2020c. Analysis of the model of HIV-1 infection of $CD4^+$ T-cell with a new approach of fractional derivative. Advances in Difference Equations 2020, 1–17.

Berenreiterová, M., Flegr, J., Kuběna, A.A., Němec, P., 2011. The distribution of Toxoplasma gondii cysts in the brain of a mouse with latent toxoplasmosis: implications for the behavioral manipulation hypothesis. PloS One 6, e28925.

Bocharov, G., Meyerhans, A., Bessonov, N., Trofimchuk, S., Volpert, V., 2016. Spatiotemporal dynamics of virus infection spreading in tissues. PloS One 11, e0168576.

Bowman, C., Gumel, A., Van den Driessche, P., Wu, J., Zhu, H., 2005. A mathematical model for assessing control strategies against west nile virus. Bulletin of mathematical biology 67, 1107–1133.

Boyer, D., Ramos-Fernández, G., Miramontes, O., Mateos, J.L., Cocho, G., Larralde, H., Ramos, H., Rojas, F., 2006. Scale-free foraging by primates emerges from their interaction with a complex environment. Proceedings of the Royal Society B: Biological Sciences 273, 1743–1750.

Brauer, F., 2008. Modeling influenza: pandemics and seasonal epidemics, in: Mathematical Epidemiology. Springer, pp. 321–347.

Brockmann, D., Hufnagel, L., Geisel, T., 2006. The scaling laws of human travel. Nature 439, 462–465.

Cannon, J., Asperti-Boursin, F., Fricke, M., Letendre, K., Moses, M., 2014. T cell motility within lymph nodes fits a levy signature (cam1p. 225).

Cartea, Á., del Castillo-Negrete, D., 2007a. Fluid limit of the continuous-time random walk with general lévy jump distribution functions. Physical Review E 76, 041105.

Cartea, A., del Castillo-Negrete, D., 2007b. Fractional diffusion models of option prices in markets with jumps. Physica A: Statistical Mechanics and its Applications 374, 749–763.

del Castillo-Negrete, D., 2009. Truncation effects in superdiffusive front propagation with lévy flights. Physical Review E 79, 031120.

del Castillo-Negrete, D., Carreras, B., Lynch, V., 2004. Fractional diffusion in plasma turbulence. Physics of Plasmas 11, 3854–3864.

del Castillo-Negrete, D., Carreras, B., Lynch, V., 2005. Nondiffusive transport in plasma turbulence: a fractional diffusion approach. Physical Review Letters 94, 065003.

Chambers, J.M., Mallows, C.L., Stuck, B., 1976. A method for simulating stable random variables. Journal of the american statistical association 71, 340–344.

Chaplain, M., Matzavinos, A., 2006. Mathematical modelling of spatio-temporal phenomena in tumour immunology, in: Tutorials in Mathematical Biosciences III. Springer, pp. 131–183.

Chaves, A., 1998. A fractional diffusion equation to describe Lévy flights. Physics Letters A 239, 13–16.

Chen, J., Huang, J., Beier, J.C., Cantrell, R.S., Cosner, C., Fuller, D.O., Zhang, G., Ruan, S., 2016. Modeling and control of local outbreaks of west nile virus in the united states. Discrete & Continuous Dynamical Systems-B 21, 2423.

Chen, Y.C., Lu, P.E., Chang, C.S., Liu, T.H., 2020. A time-dependent sir model for covid-19 with undetectable infected persons. IEEE Transactions on Network Science and Engineering 7, 3279–3294.

Cheng, C., Zheng, Z., 2021. Dynamics and spreading speed of a reaction-diffusion system with advection modeling West Nile virus. Journal of Mathematical Analysis and Applications 493, 124507.

Ciotti, M., Ciccozzi, M., Terrinoni, A., Jiang, W.C., Wang, C.B., Bernardini, S., 2020. The covid-19 pandemic. Critical reviews in clinical laboratory sciences 57, 365–388.

Cleaveland, S., Laurenson, M.K., Taylor, L.H., 2001. Diseases of humans and their domestic mammals: pathogen characteristics, host range and the risk of emergence. Philosophical Transactions of the Royal Society of London. Series B: Biological Sciences 356, 991–999.

Cole, B.J., 1995. Fractal time in animal behaviour: the movement activity of drosophila. Animal Behaviour 50, 1317–1324.

Cruz-Pacheco, G., Esteva, L., Montaño-Hirose, J.A., Vargas, C., 2005. Modelling the dynamics of west nile virus. Bulletin of mathematical biology 67, 1157–1172.

Darsie Jr, R.F., Ward, R.A., 1981. Identification and geographical distribution of the mosquitoes of North America, north of Mexico. Technical Report. Walter Reed Army Inst of Research Washington DC.

Denkers, E.Y., 1999. T lymphocyte-dependent effector mechanisms of immunity to Toxoplasma gondii. Microbes and Infection 1, 699–708.

Denkers, E.Y., Gazzinelli, R.T., 1998. Regulation and function of T-cell-mediated immunity during Toxoplasma gondii infection. Clinical Microbiology Reviews 11, 569–588.

Ding, Y., Ye, H., 2009. A fractional-order differential equation model of HIV infection of $CD4^+$ T-cells. Mathematical and Computer Modelling 50, 386–392.

Djilali, S., Ghanbari, B., Bentout, S., Mezouaghi, A., 2020. Turing-hopf bifurcation in a diffusive mussel-algae model with time-fractional-order derivative. Chaos, Solitons & Fractals 138, 109954.

Dokoumetzidis, A., Macheras, P., 2009. Fractional kinetics in drug absorption and disposition processes. Journal of pharmacokinetics and pharmacodynamics 36, 165–178.

Van den Driessche, P., Watmough, J., 2008. Further notes on the basic reproduction number, in: Mathematical epidemiology. Springer, pp. 159–178.

Dubey, J.P., 2016. Toxoplasmosis of animals and humans. CRC Press.

E Paul, W., 2003. Fundamental immunology. New York.

Esteva, L., Vargas, C., 1998. Analysis of a dengue disease transmission model. Mathematical biosciences 150, 131–151.

Farhadi, A., Hanert, E., 2022a. A fractional diffusion model of $CD8^+$ T cells response to parasitic infection in the brain. Mathematical Modelling of Natural Phenomena 17, 3.

Farhadi, A., Hanert, E., 2022b. Front propagation of exponentially truncated fractional-order epidemics. Fractal and Fractional 6, 53.

Ferguson, D., Hutchison, W., Pettersen, E., 1989. Tissue cyst rupture in mice chronically infected with Toxoplasma gondii. Parasitology Research 75, 599–603.

Franssen, L.C., Lorenzi, T., Burgess, A.E., Chaplain, M.A., 2019. A mathematical framework for modelling the metastatic spread of cancer. Bulletin of mathematical biology 81, 1965–2010.

Freund, J.E., Miller, I., Miller, M., 2004. John E. Freund's Mathematical Statistics: With Applications. Pearson Education India.

Fricke, G.M., Letendre, K.A., Moses, M.E., Cannon, J.L., 2016. Persistence and adaptation in immunity: T cells balance the extent and thoroughness of search. PLoS computational biology 12, e1004818.

Gazzinelli, R.T., Wysocka, M., Hayashi, S., Denkers, E.Y., Hieny, S., Caspar, P., Trinchieri, G., Sher, A., 1994. Parasite-induced IL-12 stimulates early IFN-gamma synthesis and resistance during acute infection with Toxoplasma gondii. The Journal of Immunology 153, 2533–2543.

Giordano, B.V., Kaur, S., Hunter, F.F., 2017. West Nile virus in Ontario, Canada: A twelve-year analysis of human case prevalence, mosquito surveillance, and climate data. PloS one 12, e0183568. URL: https://doi.org/10.1371/journal.pone.0183568.

Goddard, L.B., Roth, A.E., Reisen, W.K., Scott, T.W., 2003. Vertical transmission of West Nile virus by three california culex (diptera: Culicidae) species. Journal of medical entomology 40, 743–746.

Gorenflo, R., Mainardi, F., 2008a. Continuous time random walk, mittag-leffler waiting time and fractional diffusion: mathematical aspects. Anomalous Transport , 93–127.

Gorenflo, R., Mainardi, F., 2008b. Fractional calculus: integral and differential equations of fractional order. arXiv preprint arXiv:0805.3823 .

Halonen, S., Lyman, W., Chiu, F., 1996. Growth and development of Toxoplasma gondii in human neurons and astrocytes. Journal of Neuropathology and Experimental Neurology 55, 1150–1156.

Hampton, M.M., 2015. Congenital toxoplasmosis: a review. Neonatal Network 34, 274–278.

Hanert, E., 2010. A comparison of three Eulerian numerical methods for fractional-order transport models. Environmental Fluid Mechanics 10, 7–20.

Hanert, E., 2011. On the numerical solution of space-time fractional diffusion models. Computers & Fluids 46, 33–39.

Hanert, E., 2012. Front dynamics in a two-species competition model driven by Lévy flights. Journal of Theoretical Biology 300, 134–142.

Hanert, E., Piret, C., 2014. A chebyshev pseudospectral method to solve the space-time tempered fractional diffusion equation. SIAM Journal on Scientific Computing 36, A1797–A1812.

Hanert, E., Schumacher, E., Deleersnijder, E., 2011. Front dynamics in fractional-order epidemic models. Journal of Theoretical Biology 279, 9–16.

Harris, T.H., Banigan, E.J., Christian, D.A., Konradt, C., Wojno, E.D.T., Norose, K., Wilson, E.H., John, B., Weninger, W., Luster, A.D., et al., 2012. Generalized Lévy walks and the role of chemokines in migration of effector $CD8^+$ T cells. Nature 486, 545–548.

Hawkins, B.T., Davis, T.P., 2005. The blood-brain barrier/neurovascular unit in health and disease. Pharmacological Reviews 57, 173–185.

Huang, C., Liu, H., Chen, X., Zhang, M., Ding, L., Cao, J., Alsaedi, A., 2020. Dynamic optimal control of enhancing feedback treatment for a delayed fractional order predator–prey model. Physica A: Statistical Mechanics and Its Applications 554, 124136.

Huang, C., Nie, X., Zhao, X., Song, Q., Tu, Z., Xiao, M., Cao, J., 2019. Novel bifurcation results for a delayed fractional-order quaternion-valued neural network. Neural Networks 117, 67–93.

Hubálek, Z., Halouzka, J., 1999. West Nile fever–a reemerging mosquito-borne viral disease in Europe. Emerging infectious diseases 5, 643. URL: http://dx.doi.org/10.3201/eid0505.990505.

Huda, S., Weigelin, B., Wolf, K., Tretiakov, K.V., Polev, K., Wilk, G., Iwasa, M., Emami, F.S., Narojczyk, J.W., Banaszak, M., et al., 2018. Lévy-like movement patterns of metastatic cancer cells revealed in microfabricated systems and implicated in vivo. Nature communications 9, 1–11.

Humphries, N.E., Queiroz, N., Dyer, J.R., Pade, N.G., Musyl, M.K., Schaefer, K.M., Fuller, D.W., Brunnschweiler, J.M., Doyle, T.K., Houghton, J.D., et al., 2010. Environmental context explains Lévy and Brownian movement patterns of marine predators. Nature 465, 1066–1069.

Humphries, N.E., Weimerskirch, H., Sims, D.W., 2013. A new approach for objective identification of turns and steps in organism movement data relevant to random walk modelling. Methods in Ecology and Evolution 4, 930–938.

Ibe, O.C., 2013. Elements of random walk and diffusion processes. John Wiley & Sons.

Jajarmi, A., Baleanu, D., 2018. A new fractional analysis on the interaction of HIV with $CD4^+$ T-cells. Chaos, Solitons & Fractals 113, 221–229.

Jajarmi, A., Baleanu, D., 2020. A new iterative method for the numerical solution of high-order non-linear fractional boundary value problems. Frontiers in Physics 8, 220.

Jajarmi, A., Baleanu, D., 2021. On the fractional optimal control problems with a general derivative operator. Asian Journal of Control 23, 1062–1071.

John, B., Harris, T.H., Tait, E.D., Wilson, E.H., Gregg, B., Ng, L.G., Mrass, P., Roos, D.S., Dzierszinski, F., Weninger, W., et al., 2009. Dynamic imaging of $CD8^+$ T cells and dendritic cells during infection with Toxoplasma gondii. PLoS Pathog 5, e1000505.

Källén, A., Arcuri, P., Murray, J., 1985. A simple model for the spatial spread and control of rabies. Journal of theoretical biology 116, 377–393.

Kalmykov, Y.P., Coffey, W.T., Rice, S.A., 2006. Fractals, Diffusion, and Relaxation in Disordered Complex Systems, Volume 133, Part A. John Wiley & Sons.

Keeling, M.J., Rohani, P., 2011. Modeling infectious diseases in humans and animals. Princeton university press.

Kelly, J.F., Sankaranarayanan, H., Meerschaert, M.M., 2019. Boundary conditions for two-sided fractional diffusion. Journal of Computational Physics 376, 1089–1107.

Kenkre, V., Parmenter, R.R., Peixoto, I., Sadasiv, L., 2005. A theoretical framework for the analysis of the West Nile virus epidemic. Mathematical and computer modelling 42, 313–324.

Kilbas, A.A., Marichev, O., Samko, S., 1993. Fractional integrals and derivatives (theory and applications).

Kilpatrick, A.M., LaDeau, S.L., Marra, P.P., 2007. Ecology of West Nile virus transmission and its impact on birds in the western hemisphere. The Auk 124, 1121–1136.

Klafter, J., Sokolov, I.M., 2011. First steps in random walks: from tools to applications. Oxford University Press.

Komar, N., Langevin, S., Hinten, S., Nemeth, N., Edwards, E., Hettler, D., Davis, B., Bowen, R., Bunning, M., 2003. Experimental infection of north american birds with the New york 1999 strain of West Nile virus. Emerging infectious diseases 9, 311.

Konradt, C., Ueno, N., Christian, D.A., Delong, J.H., Pritchard, G.H., Herz, J., Bzik, D.J., Koshy, A.A., McGavern, D.B., Lodoen, M.B., et al., 2016. Endothelial cells are a replicative niche for entry of Toxoplasma gondii to the central nervous system. Nature Microbiology 1, 1–8.

Koponen, I., 1995. Analytic approach to the problem of convergence of truncated lévy flights towards the gaussian stochastic process. Physical Review E 52, 1197.

Krummel, M.F., Bartumeus, F., Gérard, A., 2016. T cell migration, search strategies and mechanisms. Nature Reviews Immunology 16, 193.

Kuznetsov, V.A., Makalkin, I.A., Taylor, M.A., Perelson, A.S., 1994. Nonlinear dynamics of immunogenic tumors: parameter estimation and global bifurcation analysis. Bulletin of Mathematical Biology 56, 295–321.

Landrith, T.A., Harris, T.H., Wilson, E.H., 2015. Characteristics and critical function of $CD8^+$ T cells in the Toxoplasma-infected brain, in: Seminars in immunopathology, Springer. pp. 261–270.

Lévy, P., 1937. Théorie de l'addition des variables aléatoires, volume 1 of monographies des probabilités, publiés sous la direction de e. Borel. Gauthier–Villars, Paris .

Lewis, M., Rencławowicz, J., den Driessche, P.v., 2006a. Traveling waves and spread rates for a West Nile virus model. Bulletin of mathematical biology 68, 3–23.

Lewis, M.A., Rencławowicz, J., Driessche, P.v.d., Wonham, M., 2006b. A comparison of continuous and discrete-time West Nile virus models. Bulletin of Mathematical Biology 68, 491–509.

Li, H., Qi, S., Jin, H., Qi, Z., Zhang, Z., Fu, L., Luo, Q., 2015. Zigzag generalized levy walk: the in vivo search strategy of immunocytes. Theranostics 5, 1275.

Lihoreau, M., Ings, T.C., Chittka, L., Reynolds, A.M., 2016. Signatures of a globally optimal searching strategy in the three-dimensional foraging flights of bumblebees. Scientific Reports 6, 1–13.

Lüder, C.G., Giraldo-Velásquez, M., Sendtner, M., Gross, U., 1999. Toxoplasma gondii in primary rat CNS cells: differential contribution of neurons, astrocytes, and microglial cells for the intracerebral development and stage differentiation. Experimental Parasitology 93, 23–32.

Luft, B.J., Remington, J.S., 1988. Toxoplasmic encephalitis. Journal of Infectious Diseases 157, 1–6.

MAIDANA, N.A., YANG, H.M., 2008. Assessing the spatial propagation of West Nile virus. Biophysical Reviews and Letters 3, 227–239.

Maidana, N.A., Yang, H.M., 2008. Describing the geographic spread of dengue disease by traveling waves. Mathematical biosciences 215, 64–77.

Maidana, N.A., Yang, H.M., 2009. Spatial spreading of west nile virus described by traveling waves. Journal of theoretical biology 258, 403–417.

Mainardi, F., Luchko, Y., Pagnini, G., 2007. The fundamental solution of the space-time fractional diffusion equation. arXiv preprint cond-mat/0702419 .

Mantegna, R.N., Stanley, H.E., 1994. Stochastic process with ultra-slow convergence to a gaussian: the truncated lévy flight. Physical Review Letters 73, 2946.

Marra, P.P., Griffing, S., Caffrey, C., Kilpatrick, M.A., McLean, R., Brand, C., Saito, E., Dupuis, A.P., Kramer, L., Novak, R., 2004. West Nile virus and wildlife. Bioscience 54, 393–402.

McCabe, R., Remington, J., et al., 1990. Toxoplasma gondii. Principles and Practice of Infectious Diseases , 2090–2103.

Méndez, V., Campos, D., Bartumeus, F., 2016. Stochastic foundations in movement ecology. Springer.

Metzler, R., Klafter, J., 2000. The random walk's guide to anomalous diffusion: a fractional dynamics approach. Physics Reports 339, 1–77.

Miller, M.J., Wei, S.H., Parker, I., Cahalan, M.D., 2002. Two-photon imaging of lymphocyte motility and antigen response in intact lymph node. Science 296, 1869–1873.

Miramontes, O., DeSouza, O., Paiva, L.R., Marins, A., Orozco, S., 2014. Lévy flights and self-similar exploratory behaviour of termite workers: beyond model fitting. PloS one 9, e111183.

Mohammadi, F., Moradi, L., Baleanu, D., Jajarmi, A., 2018. A hybrid functions numerical scheme for fractional optimal control problems: application to nonanalytic dynamic systems. Journal of Vibration and Control 24, 5030–5043.

Molaei, G., Andreadis, T.G., Armstrong, P.M., Anderson, J.F., Vossbrinck, C.R., 2006. Host feeding patterns of culex mosquitoes and West Nile virus transmission, northeastern United States. Emerging infectious diseases 12, 468.

Montroll, E.W., Weiss, G.H., 1965. Random walks on lattices. ii. Journal of Mathematical Physics 6, 167–181.

Moses, M.E., Cannon, J.L., Gordon, D.M., Forrest, S., 2019. Distributed adaptive search in T cells: Lessons from ants. Frontiers in Immunology 10, 1357.

Mrass, P., Oruganti, S.R., Fricke, G.M., Tafoya, J., Byrum, J.R., Yang, L., Hamilton, S.L., Miller, M.J., Moses, M.E., Cannon, J.L., 2017. ROCK regulates the intermittent mode of interstitial

T cell migration in inflamed lungs. Nature Communications 8, 1–14.

Mundt, C.C., Sackett, K.E., Wallace, L.D., Cowger, C., Dudley, J.P., 2009. Long-distance dispersal and accelerating waves of disease: empirical relationships. The American Naturalist 173, 456–466.

Murgue, B., Murri, S., Triki, H., Deubel, V., Zeller, H., 2001. West Nile in the mediterranean basin: 1950-2000. Annals of the New York Academy of Sciences 951, 117–126. URL: https://doi.org/10.1111/j.1749-6632.2001.tb02690.x.

Murray, J.D., 2001. Mathematical biology II: spatial models and biomedical applications. volume 3. Springer New York.

Nash, D., Mostashari, F., Fine, A., Miller, J., O'leary, D., Murray, K., Huang, A., Rosenberg, A., Greenberg, A., Sherman, M., et al., 2001. The outbreak of West Nile virus infection in the New York city area in 1999. New England Journal of Medicine 344, 1807–1814. URL: http://dx.doi.org/10.1056/NEJM200106143442401.

Nelson, K.E., Williams, C.M., 2014. Infectious disease epidemiology: theory and practice. Jones & Bartlett Publishers.

Nguyen Edalgo, Y.T., Ford Versypt, A.N., 2018. Mathematical modeling of metastatic cancer migration through a remodeling extracellular matrix. Processes 6, 58.

Okada, T., Miller, M.J., Parker, I., Krummel, M.F., Neighbors, M., Hartley, S.B., O'Garra, A., Cahalan, M.D., Cyster, J.G., 2005. Antigen-engaged B cells undergo chemotaxis toward the T zone and form motile conjugates with helper T cells. PLoS Biol 3, e150.

Okubo, A., Levin, S.A., 2001. Diffusion and ecological problems: modern perspectives. volume 14. Springer.

Okubo, A., Levin, S.A., 2013. Diffusion and ecological problems: modern perspectives. volume 14. Springer Science & Business Media.

Oldham, K., Spanier, J., 1974. The fractional calculus theory and applications of differentiation and integration to arbitrary order. Elsevier.

Peterson, A.T., Vieglais, D.A., Andreasen, J.K., 2003. Migratory birds modeled as critical transport agents for West Nile virus in North America. Vector-Borne and Zoonotic Diseases 3, 27–37.

Piret, C., Hanert, E., 2013. A radial basis functions method for fractional diffusion equations. Journal of Computational Physics 238, 71–81.

Podlubny, I., 1998. Fractional differential equations: an introduction to fractional derivatives, fractional differential equations, to methods of their solution and some of their applications. Elsevier.

Podlubny, I., 1999. Fractional differential equations. volume 198, Mathematics in Science and Engineering. Academic Press, San Diego, Calif, USA.

Preston, S., Waters, S., Jensen, O., Heaton, P., Pritchard, D., 2006. T-cell motility in the early stages of the immune response modeled as a random walk amongst targets. Physical Review E 74, 011910.

Pu, L., Lin, Z., Lou, Y., 2021. A West Nile virus nonlocal model with free boundaries and seasonal succession. arXiv preprint arXiv:2110.08055 .

Radke, J.R., Striepen, B., Guerini, M.N., Jerome, M.E., Roos, D.S., White, M.W., 2001. Defining the cell cycle for the tachyzoite stage of Toxoplasma gondii. Molecular and Biochemical Parasitology 115, 165–175.

Raghib, M., Levin, S.A., Kevrekidis, I.G., 2010. Multiscale analysis of collective motion and decision-making in swarms: an advection–diffusion equation with memory approach. Journal of Theoretical Biology 264, 893–913.

Ramos-Fernández, G., Mateos, J.L., Miramontes, O., Cocho, G., Larralde, H., Ayala-Orozco, B., 2004. Lévy walk patterns in the foraging movements of spider monkeys (ateles geoffroyi). Behavioral ecology and Sociobiology 55, 223–230.

Reynolds, A.M., 2009. Lévy flight patterns are predicted to be an emergent property of a bumblebees' foraging strategy. Behavioral Ecology and Sociobiology 64, 19–23.

Reynolds, A.M., Frye, M.A., 2007. Free-flight odor tracking in drosophila is consistent with an optimal intermittent scale-free search. PloS One 2, e354.

Reynolds, A.M., Schultheiss, P., Cheng, K., 2014. Does the australian desert ant melophorus bagoti approximate a lévy search by an intrinsic bi-modal walk? Journal of theoretical biology 340, 17–22.

Reynolds, A.M., Smith, A.D., Menzel, R., Greggers, U., Reynolds, D.R., Riley, J.R., 2007a. Displaced honey bees perform optimal scale-free search flights. Ecology 88, 1955–1961.

Reynolds, A.M., Smith, A.D., Reynolds, D.R., Carreck, N.L., Osborne, J.L., 2007b. Honeybees perform optimal scale-free searching flights when attempting to locate a food source. Journal of Experimental Biology 210, 3763–3770.

Riggs, T., Walts, A., Perry, N., Bickle, L., Lynch, J.N., Myers, A., Flynn, J., Linderman, J.J., Miller, M.J., Kirschner, D.E., 2008. A comparison of random vs. chemotaxis-driven contacts of T cells with dendritic cells during repertoire scanning. Journal of Theoretical Biology 250, 732–751.

Rosiński, J., 2007. Tempering stable processes. Stochastic processes and their applications 117, 677–707.

Sajjadi, S.S., Baleanu, D., Jajarmi, A., Pirouz, H.M., 2020. A new adaptive synchronization and hyperchaos control of a biological snap oscillator. Chaos, Solitons & Fractals 138, 109919.

Scalas, E., Gorenflo, R., Mainardi, F., 2000. Fractional calculus and continuous-time finance. Physica A: Statistical Mechanics and its Applications 284, 376–384.

Schlüter, D., Deckert, M., Hof, H., Frei, K., 2001. Toxoplasma gondii infection of neurons induces neuronal cytokine and chemokine production, but gamma interferon-and tumor necrosis factor-stimulated neurons fail to inhibit the invasion and growth of T. gondii. Infection and Immunity 69, 7889–7893.

Shigesada, N., Kawasaki, K., 1997. Biological invasions: theory and practice. Oxford University Press, UK.

Shlesinger, M.F., Klafter, J., 1986. Lévy walks versus lévy flights, in: On growth and form. Springer, pp. 279–283.

Sims, D.W., Southall, E.J., Humphries, N.E., Hays, G.C., Bradshaw, C.J., Pitchford, J.W., James, A., Ahmed, M.Z., Brierley, A.S., Hindell, M.A., et al., 2008. Scaling laws of marine predator search behaviour. Nature 451, 1098–1102.

Skariah, S., McIntyre, M.K., Mordue, D.G., 2010. Toxoplasma gondii: determinants of tachyzoite to bradyzoite conversion. Parasitology Research 107, 253–260.

Small, M., Walker, D.M., Tse, C.K., 2007. Scale-free distribution of avian influenza outbreaks. Physical review letters 99, 188702.

Smithburn, K., Hughes, T., Burke, A., Paul, J., et al., 1940. A neurotropic virus isolated from the blood of a native of Uganda. American journal of tropical medicine 20, 471–2.

Sullivan, A., Agusto, F., Bewick, S., Su, C., Lenhart, S., Zhao, X., 2012. A mathematical model for within-host Toxoplasma gondii invasion dynamics. Mathematical Biosciences Engineering 9, 647.

Sullivan, A.M., Zhao, X., Suzuki, Y., Ochiai, E., Crutcher, S., Gilchrist, M.A., 2013. Evidence for finely-regulated asynchronous growth of Toxoplasma gondii cysts based on data-driven model selection. PLoS Comput Biol 9, e1003283.

Suzuki, Y., Wang, X., Jortner, B.S., Payne, L., Ni, Y., Michie, S.A., Xu, B., Kudo, T., Perkins, S., 2010. Removal of Toxoplasma gondii cysts from the brain by perforin-mediated activity of $CD8^+$ T cells. The American Journal of Pathology 176, 1607–1613.

Sweilam, N., Saad, O., Mohamed, D., 2019. Fractional optimal control in transmission dynamics of West Nile virus model with state and control time delay: a numerical approach. Advances in Difference Equations 2019, 1–25.

Tiwari, A., Hannah, R., Lutshumba, J., Ochiai, E., Weiss, L.M., Suzuki, Y., 2019. Penetration of $CD8^+$ cytotoxic T cells into large target, tissue cysts of Toxoplasma gondii, leads to its elimination. The American Journal of Pathology 189, 1594–1607.

Torrey, E.F., Yolken, R.H., 2003. Toxoplasma gondii and schizophrenia. Emerging infectious diseases 9, 1375.

Vallaeys, V., Tyson, R.C., Lane, W.D., Deleersnijder, E., Hanert, E., 2017. A Lévy-flight diffusion model to predict transgenic pollen dispersal. Journal of the Royal Society Interface 14, 20160889.

Veit, R.R., Lewis, M.A., 1996. Dispersal, population growth, and the allee effect: dynamics of the house finch invasion of eastern north america. The American Naturalist 148, 255–274.

Viswanathan, G.M., Da Luz, M.G., Raposo, E.P., Stanley, H.E., 2011. The physics of foraging: an introduction to random searches and biological encounters. Cambridge University Press.

Viswanathan, G.M., Raposo, E., Da Luz, M., 2008. Lévy flights and superdiffusion in the context of biological encounters and random searches. Physics of Life Reviews 5, 133–150.

Viswanthan, G., 1996. Levy flight search patterns of wandering albatrosses. Nature 381, 413415.

Von Economo, C., 2009. Cellular structure of the human cerebral cortex. Karger Medical and Scientific Publishers.

Wang, X., Michie, S.A., Xu, B., Suzuki, Y., 2007. Importance of ifn-γ-mediated expression of endothelial vcam-1 on recruitment of $CD8^+$ T cells into the brain during chronic infection with toxoplasma gondii. Journal of Interferon & Cytokine Research 27, 329–338.

Wei, S.H., Parker, I., Miller, M.J., Cahalan, M.D., 2003. A stochastic view of lymphocyte motility and trafficking within the lymph node. Immunological Reviews 195, 136–159.

Weiss, L.M., Kim, K., 2011. Toxoplasma gondii: the model apicomplexan. Perspectives and methods. Elsevier.

Weron, A., Weron, R., 1995. Computer simulation of lévy α-stable variables and processes, in: Chaos—The interplay between stochastic and deterministic behaviour. Springer, pp. 379–392.

Wilson, E.H., Weninger, W., Hunter, C.A., et al., 2010. Trafficking of immune cells in the central nervous system. The Journal of Clinical Investigation 120, 1368–1379.

Witt, C.M., Raychaudhuri, S., Schaefer, B., Chakraborty, A.K., Robey, E.A., 2005. Directed migration of positively selected thymocytes visualized in real time. PLoS Biol 3, e160.

Wodarz, D., Christensen, J.P., Thomsen, A.R., 2002. The importance of lytic and nonlytic immune responses in viral infections. TRENDS in Immunology 23, 194–200.

Wohlfert, E.A., Blader, I.J., Wilson, E.H., 2017. Brains and brawn: Toxoplasma infections of the central nervous system and skeletal muscle. Trends in Parasitology 33, 519–531.

Wonham, M.J., de Camino-Beck, T., Lewis, M.A., 2004. An epidemiological model for West Nile virus: invasion analysis and control applications. Proceedings of the Royal Society of London. Series B: Biological Sciences 271, 501–507.

Work, T.H., Hurlbut, H.S., Taylor, R., et al., 1955. Indigenous wild birds of the Nile Delta as potential West Nile virus circulating reservoirs. American Journal of Tropical Medicine and Hygiene 4, 872–88.

Wu, J., 2008. Spatial structure: partial differential equations models, in: Mathematical epidemiology. Springer, pp. 191–203.

Xu, C., Liao, M., Li, P., Guo, Y., Liu, Z., 2021a. Bifurcation properties for fractional order delayed bam neural networks. Cognitive Computation 13, 322–356.

Xu, C., Zhang, W., Aouiti, C., Liu, Z., Liao, M., Li, P., 2021b. Further investigation on bifurcation and their control of fractional-order bidirectional associative memory neural networks involving four neurons and multiple delays. Mathematical Methods in the Applied Sciences .

Yuan, J., Zhao, L., Huang, C., Xiao, M., 2021. Stability and bifurcation analysis of a fractional predator–prey model involving two nonidentical delays. Mathematics and Computers in Simulation 181, 562–580.

Zhang, X., Lv, M., Crawford, J.W., Young, I.M., 2007. The impact of boundary on the fractional advection–dispersion equation for

solute transport in soil: Defining the fractional dispersive flux with the caputo derivatives. Advances in Water Resources 30, 1205–1217.

Ziegler, U., Lühken, R., Keller, M., Cadar, D., Van Der Grinten, E., Michel, F., Albrecht, K., Eiden, M., Rinder, M., Lachmann, L., et al., 2019. West Nile virus epizootic in Germany, 2018. Antiviral research 162, 39–43.